Ultrafast Spectroscopy of Charge Separation, Transport and Recombination Processes in Functional Materials for Thin-Film Photovoltaics

Christian Wehrenfennig

University College

University of Oxford

A thesis submitted for the degree of

Doctor of Philosophy

Trinity 2014

Abstract:

Ultrafast Spectroscopy of Charge Separation, Transport and Recombination Processes in Functional Materials for Thin-Film Photovoltaics

Christian Wehrenfennig, University College
Submitted for the degree of Doctor of Philosophy in Trinity 2014.

Dye-sensitized solar cells (DSSCs) and perovskite solar cells are emerging as promising potential low-cost alternatives to established crystalline silicon photovoltaics. Of the employed functional materials, however, many fundamental optoelectronic properties governing photovoltaic device operation are not sufficiently well understood. This thesis reports on a series of studies using ultrafast THz and photoluminescence spectroscopy on two classes of such materials, providing insight into the dynamics of charge-transport and recombination processes following photoexcitation.

For TiO_2-nanotubes, which have been proposed as easy-to-fabricate electron transporters for DSSCs, fast, shallow electron trapping is identified as a limiting factor for efficient charge collection. Trapping lifetimes are found to be about an order of magnitude shorter than in the prevalently employed sintered nanoparticles under similar excitation conditions and trap saturation effects are not observed, even at very high excitation densities.

In organo-lead halide perovskites - specifically $CH_3NH_3PbI_3$ and $CH_3NH_3PbI_{3-x}Cl_x$, which have only recently emerged as highly efficient absorbers and charge transporters for thin-film solar cells, carrier mobilities and fundamental recombination dynamics are revealed. Extremely low bi-molecular recombination rates at least four orders of magnitude below the prediction of Langevin's model are found as well as relatively high charge-carrier mobilities in comparison to other solution-processable materials. Furthermore a very low influence of trap-mediated recombination channels was observed. Due to a combination of these factors, diffusion lengths reach hundreds of nanometres for $CH_3NH_3PbI_3$ and several microns for $CH_3NH_3PbI_{3-x}Cl_x$. These results are shown to hold for both, solution processed and vapour-deposited $CH_3NH_3PbI_{3-x}Cl_x$ and underline the superb suitability of the materials as absorbers in solar cells, even in planar heterojunction architectures.

The THz-frequency spectrum of the conductivity of the investigated perovskites is consistent with Drude-like charge transport additionally exhibiting weak signatures of phonon coupling. These coupling effects are also reflected in the luminescence of $CH_3NH_3PbI_{3-x}Cl_x$, where they are believed to be the cause of the observed homogeneous spectral broadening. Further photoluminescence measurements were performed at temperatures between 4 K and room temperature to study the nature of recombination pathways in the material.

Publications

1. Wehrenfennig, C., Eperon, G. E., Johnston, M. B., Snaith, H. J. & Herz, L. M.: High charge-carrier mobilities and lifetimes in organolead trihalide perovskites. *Adv. Mater.* **26**, 1584–1589 (2014).

2. Wehrenfennig, C., Liu, M., Snaith, H. J., Johnston, M. B. & Herz, L. M.: Homogeneous emission line broadening in the organo lead halide perovskite $CH_3NH_3PbI_{3x}Cl_x$. *J. Phys. Chem. Lett.* **5**, 1300–1306 (2014).

3. Noel, N. K., Stranks, S. D., Abate, A., Wehrenfennig, C., Guarnera, S., Haghighirad, A. A., Sadhanala, A., Eperon, G. E., Pathak, S. K., Petrozza, A., Herz, L. M. & Snaith, H. J.: Lead-free organometal trihalide perovskites for photovoltaic applications. *Energy. Environ. Sci.* **7**, 3061–3068 (2014).

4. Raavi, S. S. K., Docampo, P., Wehrenfennig, C., Alcocer, M. J. P., Sadoughi, G., Herz, L. M., Snaith, H. J. & Petrozza, A.: The impact of molecular charge-transfer states on photocurrent generation in solid state DSSCs employing low band-gap dyes. *J. Phys. Chem. C.* **118**, 16825–16830 (2014).

5. Wehrenfennig, C., Liu, M., Snaith, H. J., Johnston, M. B. & Herz, L. M.: Charge-carrier dynamics in vapour-deposited films of the organo-lead halide perovskite $CH_3NH_3PbI_{3x}Cl_x$. *Energy. Environ. Sci.* **7**, 2269–2275 (2014).

6. Wehrenfennig, C., Liu, M., Snaith, H. J., Johnston, M. B. & Herz, L. M.: Charge-carrier recombination channels in the low-temperature phase of $CH_3NH_3PbI_{3x}Cl_x$ thin films. *APL Mat.* **2**, 081513 (2014).

7. Wehrenfennig, C., Palumbiny, C. M., Gunning, R., Schmidt-Mende, L., Snaith, H. J. & Herz, L. M.: Fast charge-carrier trapping in TiO_2 nanotubes. *J. Phys. Chem. C.* **119**, 9159-9168 (2015).

Acknowledgements

It is with great appreciation that I would like to acknowledge the support of many people who helped making the work for this thesis possible and enjoyable.

First and foremost, I am much indebted to my supervisor **Prof Laura Herz**, who dedicated a great deal of time and effort to discussing my results and providing me with valuable advice and feedback. There is certainly a lot I have learned during my time working with her. I would also like to thank **Dr Michael Johnston** for many fruitful discussions and particularly for his expert advice in experimental matters. Moreover, I have always been able to count on competent support from **my colleagues**. I would like to thank everyone in my research group, especially **Christian Weisspfennig** and **Christopher Menelaou** for introducing me to the laboratory equipment that I used for the greatest part of my experiments.

The work for this thesis was largely build upon a tight collaboration with **Prof Henry Snaith** whom I would like to thank for the opportunity to study first-hand state-of-the-art photovoltaic materials. I am much obliged to several members of his research group, in particular **Mingzhen Liu** and **Giles Eperon** for providing me with well-characterized, high-quality samples for my experiments.

During my time in Oxford I had the privilege to engage in a number of extracurricular activities which I see as an inseparable part of the pursuit of my degree. I am therefore grateful to all the people involved in running the countless clubs and societies inside and outside the University. Especially I would like to thank everyone from **Oxford University Badminton Club** for three fantastic seasons. An even more important part of my Oxford life were those people I had the pleasure to meet and become close friends with. A massive cheers for an unforgettable time to **Emanuel Ferm**, **Ryan Perkins**, **Anael Pussier**, **Anne Hillebrandt**, **Joanna Palermo**, **Petr Sulc**, **Rasmus Wissmann**, **Inbar Levy**, **Steven Wagner**, **Keru Cai**, **Pete Armstrong** and **many more**. Another big thanks goes to **my housemates** for three years of fun and trouble-free house-sharing.

I would like to express my deepest gratitude to my family, especially to **my parents** for supporting me in every situation and putting up with rather long periods of absence. Finally, it is thanks to **Katie Doig** that I already forgot how stressful the write-up of this thesis must have been, thinking of what a lovely time we spent and will be spending.

Prior to the publication of this thesis, parts of its contents were published in peer-reviewed journals. I gratefully acknowledge the permission of the respective publishers to reproduce the material in this thesis as follows:

Chapter 4 was reprinted (adapted) with permission from [C. Wehrenfennig et al., *J. Phys. Chem. C* **119**, 9159–9168 (2015)]. Copyright (2015) American Chemical Society.

Chapter 5 was reprinted (adapted) with permission from [C. Wehrenfennig et al., *Adv. Mater.* **26**, 1584–1589 (2014)]. Copyright (2013) WILEY-VCH Verlag GmbH & Co. KGaA, Weinheim.

Chapter 6 was reprinted (adapted) with permission from [C. Wehrenfennig et al., *Energy. Environ. Sci.* **7**, 2269–2275 (2014)]. Copyright (2014) The Royal Society of Chemistry.

Chapter 7 was reprinted (adapted) with permission from [C. Wehrenfennig et al., *J. Phys. Chem. Lett.* **5**, 1300–1306 (2014)]. Copyright (2014) American Chemical Society.

Chapter 8 was reprinted (adapted) with permission from [C. Wehrenfennig et al., *APL Mat.* **2**, 081513 (2014)]. Copyright (2014) AIP Publishing LLP.

"Zwischen Leber und Milz
passt immer noch 'n Pils."

Contents

1

Introduction

Photovoltaic (PV) energy conversion is not at all a new technology. In fact the first patent of a device producing an electric voltage upon irradiation with visible light dates back to 1941 [1, 2]. Even solar cells with relatively high efficiencies on the order of 20 % have been available for more then 30 years [3]. However, it was not until the past few years, that solar energy from photovoltaic cells contributed any notable amount to grid-electricity generation. After the strong political incentivization in the past decade, installed PV capacity has seen a rapid rise from 1.3 GW in 2000 to 136.7 GW in 2013 [4]. However, in spite of the dramatic decrease in module costs that has recently been achieved, photovoltaic energy conversion still faces a number of issues on its way to become competitive to the dominant conventional grid energy source coal [5]. These on one hand include infrastructural provisions to cope with the intermittent nature of solar power. On the other hand further cost reductions are required to alleviate the need for high up-front investment and government subsidies.

The commercially most successful technology at present is based on a p-n-junction in crystalline silicon and offers high efficiencies (up to 25 % [3]), very good longevity and reliability. Silicon solar-cell- and solar-cell-production technologies have advanced to a very mature and highly optimized state, such that costs for large scale production are now primarily dominated by material costs [6], which impose a fundamental limit on the potential future price development for photovoltaic energy conversion based

on silicon. In order to achieve significant further reductions, it therefore appears to be inevitable to explore alternative PV technologies that either require less material, cheaper materials or materials that can be processed in a cheaper way. Thin film solar cell technologies are a highly active field of research aiming to offer such low-cost alternatives to crystalline silicon based photovoltaics at similarly high power conversion efficiency, reliability and longevity [6, 7, 8, 9, 10]. Several approaches are currently being pursued based on a variety of device architectures and employing an even broader variety of functional materials. For many of these materials, fundamental optoelectronic properties governing photovoltaic device operation are not yet sufficiently well understood to create a complete and consistent picture of the underlying physics. Often however, such in-depth knowledge is the key to fully exploiting the potential of these materials in terms of device performance and reliability.

This thesis reports on a series of experimental studies conducted on the dynamics of photoexcited charge carriers in materials recently employed in two low-cost thin-film solar cell designs, the dye-sensitized solar cell (DSSC) and the perovskite solar cell. The DSSC was invented in the early 1990s [11] and has since seen continuous improvement through optimization of materials and processing methods [7]. Organic-inorganic hybrid perovskites were only discovered a few years ago to be highly suitable absorber materials for sensitized solar cells additionally exhibiting semiconducting properties [12, 13, 14]. This has lead to the emergence of a new class of devices branching off from the sensitized device architecture, currently attracting great research interest due to their extremely promising power conversion efficiencies [8, 9, 10] Both, dye-sensitized and perovskite solar cells are introduced in detail in Chapter 2.

The main experimental techniques employed in this work - optical-pump-THz-probe- and photoluminescence spectroscopy - are described in Chapter 3. These techniques allow to perform time-resolved investigations of charge transport and recombination processes with nanosecond to picosecond resolution.

TiO_2 nanotubes grown by anodization of Ti foil have been considered as promising alternatives to sintered TiO_2 nanoparticles as electron transport materials in dye-sensitized solar cells. However, in spite of more direct electron percolation paths from the point of injection to the outer electrode, no enhancement of charge collection has been found so far. The work reported in Chapter 4 reveals unusually fast electron trapping in TiO_2 nanotubes more than an order of magnitude faster than in nanoparticles, which can be linked to inhibited carrier diffusion within a multi-trapping transport model. Evidence is found that the corresponding trap states are not predominantly concentrated at the surface of the tubes and that a variation of the wall thickness via the anodization temperature has at most small influence on trapping lifetimes. Extracted THz carrier mobilities are similar in TiO_2-nanotubes and sintered TiO_2-nanoparticles.

The organo-lead halides $CH_3NH_3PbI_3$ and $CH_3NH_3PbI_{3-x}Cl_x$ are currently the most successfully employed active materials in perovskite solar cells [15, 16, 17]. In Chapters 5 and 6 it is shown that both compounds, prepared in the same mesoporous morphology as found in devices, exhibit exceptionally low mono-molecular and bi-molecular charge-carrier decay rates, undercutting the theoretical value from the Langevin model by at least 4 orders of magnitude. Lower bounds for the THz charge-carrier mobility of $11.6\,cm^2/(Vs)$ for $CH_3NH_3PbI_{3-x}Cl_x$ and $8\,cm^2/(Vs)$ for $CH_3NH_3PbI_3$ are established, which are remarkably high for solution-processed materials. Carrier diffusion lengths are deduced as a function of charge density and values exceeding a few microns for $CH_3NH_3PbI_{3-x}Cl_x$ are obtained under typical device operating conditions. In $CH_3NH_3PbI_3$, diffusion lengths are a factor $\sim$4 lower because of higher mono- and bi-molecular recombination rates. Together, these findings underline the suitability of organo-lead halides also for planar-heterojunction device structures, first reports of which were surfacing simultaneously to the conclusion of this work. Following this trend, a similar study is performed on solid, vapour-deposited films of the mixed halide perovskite $CH_3NH_3PbI_{3-x}Cl_x$, where charge-carrier mobil-

ities $\geq 33\,\mathrm{cm}^2/(\mathrm{Vs})$ and similarly low bi-molecular recombination rates as for the mesostructured material are determined. Diffusion lengths are shown to be only limited by slow mono-molecular decay processes, and approach three microns under realistic solar cell operating conditions. THz photoconductivity spectra are consistent with Drude-like charge transport and show no signs of localization effects.

A further investigation reported in Chapter 7 focusses on the unclear nature of the radiative decay channels in organo-lead halide perovskites, which show strong and broad photoluminescence (PL) around their bandgap energy of about 1.6 eV. In order to reveal the spectral broadening mechanisms in vapour-deposited films of $CH_3NH_3PbI_{3-x}Cl_x$ time- and excitation-energy dependent photoluminescence spectroscopy is used. It is shown that the PL spectrum is homogeneously broadened with a line width of 103 meV most likely as a consequence of phonon coupling effects. Further analysis reveals that defects or trap states play a minor role in radiative decay channels.

Photoluminescence and optical absorption studies are extended to low temperatures in Chapter 8 to supplement the proposed interpretation of spectral broadening through a polaronic mechanism. The transition of the $CH_3NH_3PbI_{3-x}Cl_x$-films to a low-temperature phase, which has been anticipated based on the well-known transition in $CH_3NH_3PbI_3$ at 160 K, is located and found to occur with large hysteresis. Recombination dynamics are investigated in this phase and an accelerated charge-carrier decay is observed. However, rather than suggesting intrinsically higher rate constants at low temperature, the data points towards the existence of scarce inclusions of domains of the high-temperature phase, in which a large fraction of photoexcited carriers agglomerates and subsequently recombines.

2

Background

2.1 Dye-Sensitized Solar Cells

One of the great challenges in designing cheap yet efficient solar cells is to find active materials fulfilling a broad variety of requirements simultaneously. These are economic requirements such as price and abundance, technical requirements including large scale, low energy processability, and physical requirements such as strong optical absorption, a suitable bandgap, good charge conductivity and long photoexcited carrier lifetimes. The concept of the dye-sensitized solar cell (DSSC), pioneered by *O'Regan* and *Grätzel* [11] in the early 1990s aims to tackle some of these tough constraints by employing separate materials for light harvesting (absorption) and transport of the separated charges to the contacts of the device.

In a typical DSSC, incident light is absorbed by a dye which is deposited as a single molecular layer on a porous semiconductor. This geometry allows for the generated free electrons to rapidly transfer to the conduction band of the semiconductor, which acts as the electron transport material (ETM) and enables electrons to travel to the anode contact while the absorber itself is usually an insulator. The resulting nanostructure is infiltrated with either a redox electrolyte or a solid state hole transport material (HTM) for conduction of the holes to the cathode contact. Figure 2.1 shows a simplified sketch and energy level diagram of a typical DSSC. Before proceeding

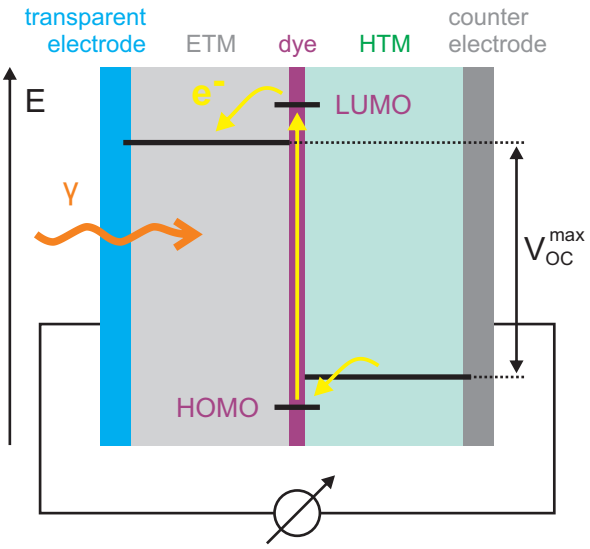

Figure 2.1: Simplified sketch and energy diagram of a dye sensitized solar cell. Note that ETM, dye and HTM layers are drawn flat for clarity, while the actual structure is mesoporous (see Figure 2.5(a)).

with a systematic description of its photovoltaic operation, the most important relative advantages and drawbacks of the DSSC with respect to conventional, crystalline silicon based devices shall be summarized.

Among the benefits of DSSCs is a high degree of tunability of the absorption spectrum through the choice of an appropriate dye, which also makes these devices suitable for application in semi-transparent glazing or as architectural design elements. Moreover, so called tandem cells can in principle defy the fundamental Schockley-Queisser-Limit for single junction cells [18], if the absorption edges of the individual light harvesters are well engineered [19, 20, 21]. Due to the very high extinction coefficients achievable in many dyes the overall thickness of the device can be reduced a few micrometers [22], which in turn tremendously brings down material costs for DSSCs.

On the downside, as a consequence of the separation of absorber and transporters, at least two injection steps are involved in the charge extraction process, which are both inevitably accompanied by a certain potential drop. Therefore, the open circuit voltage of the cell is significantly reduced with respect to the energy difference between

ground state and excited state of the absorber. Another performance-limiting factor arises from the nanostructured morphology of the electron extracting semiconductor. Due to their high surface-to-volume ratio, nanostructured materials naturally exhibit a higher concentration of interband states than their bulk counterparts as a direct consequence of the lattice discontinuity and often through increased adsorption or incorporation of impurities. These interband states act as traps for charge carriers limiting their mobility and often facilitating recombination. [23, 24, 25] Providing a clearer picture of transport limiting processes in nanostructured TiO_2, the most widely used electron extraction material in DSSCs and the possible benefits of using ordered, tubular structures instead of sintered nanoparticles is the objective of Chapter 4 of this thesis.

Aside from factors directly relating to power conversion efficiency, further challenges in the development dye-sensitized solar cells pertain chemical stability, especially of the employed dye in the presence of oxygen or moisture, which reduce the overall usable lifetime of the device. Fortunately, great progress has been made on this issue with certain compositions suffering only moderate performance degradation under accelerated ageing tests over several thousand hours [7, 26].

2.1.1 Photovoltaic Operation

The essential processes governing photovoltaic power conversion in dye-sensitized solar cells can be summarized as follows. (Note that despite this list being numbered the enumerated processes do not necessarily take place in strictly the listed order.)

1. Photoexcitation of the dye
2. Electron transfer (injection)
3. Hole transfer (dye regeneration)
4. Electron transport to the anode contact

5. Hole transport to the cathode contact

Efficient charge separation requires that, upon photoexcitation, electrons are rapidly injected into the conduction band of the electron transport material to avoid charge recombination on the dye. Successful material combinations often exhibit sub-ps injection dynamics which are facilitated by favourable energy level alignment and the fact that the electron wavefunction of the excited state of the absorber is concentrated close to the surface of the accepting semiconductor [27]. Although the charge injection process is often described in terms of electron transfer being followed by regeneration of the dye from the hole transporter, the reverse order process is also possible. Rapid hole extraction in systems with solid state HTMs has been shown to have a substantial effect on the efficiency of electron injection as it causes an energy shift of the lowest unoccupied molecular orbital (LUMO) of the dye and thereby alters its relative alignment to the conduction band of the ETM (reductive quenching). [28, 29].

Electron transport to the contacts is dominantly driven by diffusion rather than drift due to electric field screening by the HTM [30]. As mentioned above, nanostructured semiconductors often show inhibited charge transport due to the presence of interband trap states. A widely accepted model for conductivity in TiO_2 nanoparticle matrices assumes a distribution of shallow traps below the conduction band edge from which carriers can escape ('detrap') again thermally. [31, 32, 33] As a prediction of this model, the conductivity of the nanostructure becomes dependent on electron density due to trap-filling effects [34]. At the same time it has been observed that recombination rates R of electrons with holes either on the oxidized dye or the hole transport material show a similar dependence such that the diffusion length $L_D = \sqrt{D\tau}$ with the diffusion constant $D = \mu \cdot k_B T/e$ (μ: carrier mobility) and the recombination lifetime $\tau = 1/R$ becomes constant over a wide range of densities. [35] A possible interpretation of these observations leads to a model of kinetic ('transport-limited')

recombination, which essentially assumes that recombination occurs once an electron travels through the capture radius of a hole. As a consequence, an increase in electron mobility, for example through reduction of the trap density, would not lead to more efficient charge collection [34, 36].

An alternative interpretation could be termed 'trap-limited recombination' building upon the result of several studies showing that recombination of electrons with holes on the HTM is mediated by surface traps states on the nanostructured TiO_2 [23, 24, 25, 37]. Equally to the transport-limited model it results in simultaneously increasing conductivity and recombination with electron density rate. However, in the trap-limited model, a conductivity enhancement through the reduction of trap density is expected to lead to an increase in diffusion length.

2.1.2 Materials and Device Architectures

The original DSSC design employed a ruthenium-based charge-transfer dye supported by a 10 μm thick layer of sintered TiO_2 nanoparticles with an average diameter of about 15 nm [11]. An iodide-triiodide liquid electrolyte was used as a hole transporter. Concerns regarding the feasibility of appropriate sealing for cells containing liquid components have subsequently directed much of the attention towards all-solid-state dye-sensitized solar cells (sDSSCs) after their successful demonstration by *Bach et al.* [38]. This trend continues despite the fact that even to date these devices have only reached about half of the power conversion efficiency (6.1 % [39]) of those using liquid electrolytes (13 % [40]). Interestingly the by far most widely used solid state hole transporter 2,2',7,7'-tetrakis-(N,N-di-p-methoxyphenylamine)9,9'-spirobifluorene (spiro-OMeTAD) is still the same material as the one employed by the first sDSSC reported. The same applies to the electron transporting semiconductor TiO_2.

TiO_2 exists in three different crystallographic morphologies, anatase, rutile and

brookite, out of which the first plays the prevalent role in DSSC applications. Therefore, in this thesis, the formula TiO_2 is used in short for anatase TiO_2 unless explicitly stated otherwise. TiO_2 is an indirect, wide-gap semiconductor with a band gap energy of 3.2 eV [41] corresponding to an absorption onset in the ultraviolet at about 390 nm. Any possible charge-carrier generation in DSSCs through absorption in TiO_2 therefore plays at most a negligible role as only about 3 % of the solar intensity spectrum extends into the UV range beyond this wavelength. The electron mobility in single crystalline anatase at room temperature of $15\,cm^2/(Vs)$ as determined by means of hall effect measurements [42] is relatively low in comparison to other inorganic semiconductors commonly employed in solar cells such as silicon or gallium arsenide, which exhibit room temperature mobilities on the order of $1000\,cm^2/(Vs)$ and $8000\,cm^2/(Vs)$, respectively [43]. The polaronic nature of carriers in the material at moderate electron densities provides an explanation for the low conductivity observed [44]. For nanoparticulate TiO_2 even lower mobilities four to six orders of magnitude below the bulk single crystal value have been determined using time of flight [45] and transient photocurrent [46] measurements. This discrepancy has been subject of several studies and was by most authors attributed to the abovementioned multi-trapping phenomenon [36, 37, 47, 48, 49, 50, 51]. Studies using THz spectroscopy, which provide a figure for the 'local' and 'quasi-instantaneous' mobility (i.e. with carrier displacements much smaller than the particle size and at early times after charge-carrier generation and before significant trapping is likely to have occurred) have indeed revealed values closer to the single crystal mobility ($0.01 - 0.1\,cm^2/(Vs)$) [52, 53]. A calculation by *Hendry* and co-workers suggest that the remaining discrepancy can be accounted for by the strong electric field screening effects due to the permittivity of TiO_2 [52].

In DSSCs using liquid electrolyte hole transporters, charge recombination rates have been found to be exceptionally low such that despite the relatively low charge-carrier mobilities of TiO_2, diffusion lengths reach the order $40 - 70\,\mu m$ [35], which exceeds the

typical thickness of the DSSC active layer ($3 - 10\,\mu$m) [7, 40] enabling near complete electron collection. This ratio becomes less favourable in solid state DSSCs, where faster interfacial charge recombination and diffusion lengths of only about $6\,\mu$m have been determined under full sun operating conditions [54, 55]. Insufficient diffusion length might be partly accountable for the inferior power conversion efficiency of devices with solid state hole transporter. However, another factors, which is believed to play an at least equally important role is related to de-wetting of the pores following the infiltration of the nanostructure with the dissolved hole transporter leaving behind areas of un-contacted dye [56].

Although many attempts have been taken to create efficient DSSCs based on other wide-gap semiconductors as ETMs with higher carrier mobilities such as SnO_2 or ZnO [57, 58], efficiency records are still held by devices based on sintered TiO_2 nanoparticles [39, 40].

2.1.3 TiO_2 Nanotubes

An alternative approach to improving electron extraction in DSCs without the need to abandon TiO_2 as the semiconductor material seeks to replace the dominant nanoparticulate topology by one-dimensional structures such as nanorods of nanotubes, which ought to provide a more direct percolation path for electrons to the anode contact. A sketch of corresponding device structures is shown in Figure 2.2. TiO_2 nanotubes can be easily and cheaply fabricated by an anodization process [59]. For this a titanium electrode is placed in a suitable fluorine-containing electrolyte together with a platinum counter-electrode. Under an applied voltage of between a few and a few ten volts the titanium is oxidized while, once a compact layer has formed, diffusion of fluoride ions into the material leads to etching of pores. In an equilibrium between dissolution and oxidation, growth of regular arrays of TiO_2 nanotubes can be achieved [60]. It has been found that control over the tube diameter can be exerted

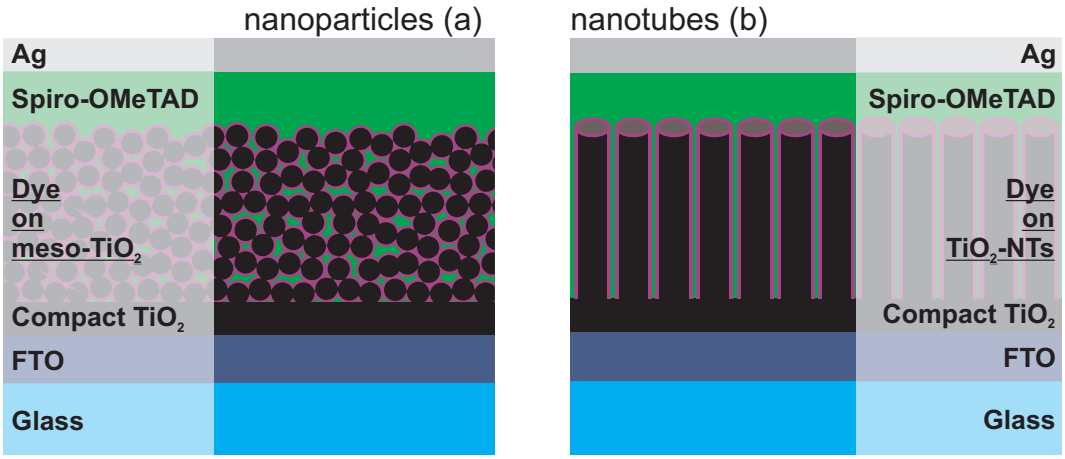

Figure 2.2: Sketch of possible structures of dye-sensitized solar cells based on TiO_2 nanoparticles (a) and TiO_2 nanotubes (b) as their electron transport material.

via the anodization voltage while anodization temperature has a strong influence on tube wall thickness [61].

As-anodized TiO_2 nanotubes are amorphous; therefore an annealing step is required to obtain polycrystalline material in either anatase or rutile structure depending on the annealing temperature used (roughly: $>250°C$ for anatase, $>450°C$ for rutile [62]).

Several attempts have been undertaken to fabricate dye-sensitized solar cells based on TiO_2 nanotubes [63, 64, 65, 66]. However, in spite of respectable power conversion efficiencies of up to 7.37 % [67] that have been achieved using a liquid electrolyte hole transporter, it has not been possible to break the records set by nanoparticle-based devices or demonstrate superior performance of nanotube-based ones in a direct comparison. [64]

An obvious drawback of nanotubes (and other 1-D nanostructures) in comparison to nanoparticles with respect to DSSC applications is their lower specific surface area, which leads to a slightly higher thickness required to support a sufficient amount of dye for complete absorption of the incident light. This in turn further increases the demands on diffusion length. A comparative study of solar cells employing TiO_2

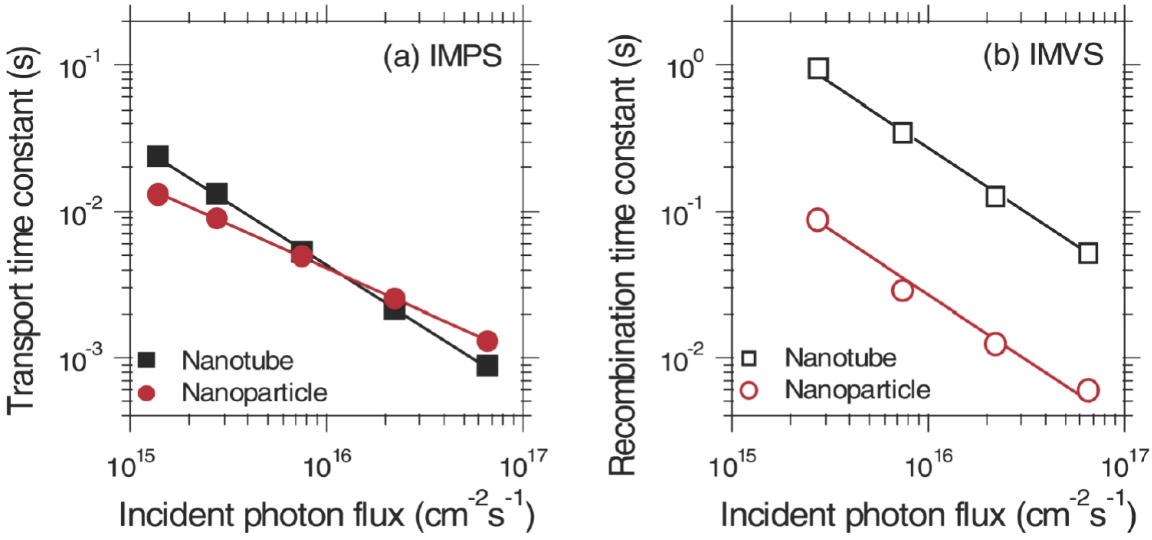

Figure 2.3: Comparison of collection time (here referred to as 'transport time', from *intensity-modulated photocurrent spectroscopy (IMPS)*) **(a)** and recombination lifetime (from *intensity-modulated photovoltage spectroscopy (IMVS)*)**(b)** in TiO_2 nanotube- and nanoparticle-based DSSCs as a function of incident photon flux. Reprinted with permission from [64]. Copyright (2007) American Chemical Society.

nanoparticle and nanotube films of the same thickness has revealed markedly enhanced recombination lifetimes for nanotubes, which may provide the necessary increase in diffusion length (see Figure 2.3. Reprinted with permission from [64]. Copyright (2007) American Chemical Society.). However, faster charge collection owing to shorter percolation paths has surprisingly not been observed, which suggest that electron mobility in TiO_2 nanotubes might on the other hand be reduced. This could be preventing nanotubes from unfolding greater potential as electron transporters in DSSCs. The study in Chapter 4 investigates the fundamental charge-carrier dynamics in this material with the intention to unravel the mechanisms underlying the observation of possible transport limiting effects in TiO_2 nanotubes.

2.2 Organometal Perovskite Solar Cells

The name *perovskite* in its original meaning refers to a mineral composed of $CaTiO_3$. However, the term is also used collectively for compounds of the chemical formula ABX_3 adopting the *perovskite structure* depicted in Figure 2.4. In its undistorted form, this structure consists of a cubic lattice of A-cations with body-centred B-cations and face-centred X-anions. From a perspective of the B-cation, the structure can be described in terms of surrounding, corner-sharing octahedral cages formed by X- anions with A-cations filling the voids in between these octahedra.

The present work studies a hybrid from of perovskites, in which an organic molecule replaces the (usually inorganic) A-cation. This modification makes these materials suitable for low-temperature solution processed fabrication routes [68], which introduces a major advantage towards low-cost large-scale device applications. As several organic-inorganic perovskites exhibit semiconducting properties, notable research efforts targeted at applications in thin-film transistors and light-emitting diodes were undertaken in the 1990s [69]. Investigations into this novel material class penetrated a large spectrum of varieties that hybrid perovskites can exist in, which also include 0D- and 2D- structures composed of larger organic A-cations separating layers of BX-octahedra or isolating individual octahedra.

First attempts to employ hybrid perovskites in solar cells were reported in 2006 by Kojima et al. using the (3D) compound methylammonium lead bromide ($CH_3NH_3PbBr_3$) as an absorber in a device architecture entirely analogous to a liquid-electrolyte dye-sensitized solar cell [12]. It was possible to improve the obtained power conversion efficiency of 2.19 % in the following years by optimization of the processing conditions and by moving to the triiodide perovskite $CH_3NH_3PbI_3$, which exhibits a more favourable bandgap than $CH_3NH_3PbBr_3$ [70, 71]. The breakthrough however was only achieved through a shift from liquid electrolyte hole transporters,

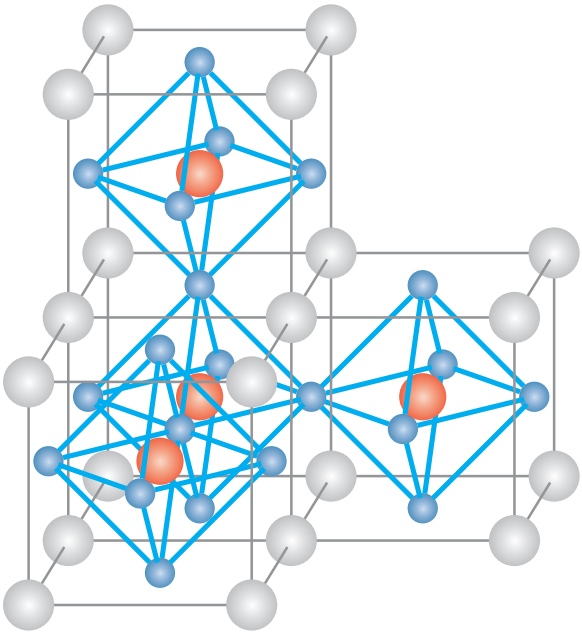

Figure 2.4: Sketch of the perovskite crystal structure. White: A-cation, red: B-cation, blue: X-anion.

which were found to rapidly decompose the perovskite, to the solid-state material spiro-OMeTAD, leading to the demonstration of device efficiencies around 10 % by two different groups in 2012 [13, 14].

The unique quality of organo-lead halides as solar cell sensitizers can be seen in a combination of solution-processability and strong optical absorption on one hand with good semiconducting properties on the other hand. Being able to transport photoexcited charge carriers, perovskite absorbers gain a tremendous advantage over dye sensitizers, due to the fact that they are not restricted in thickness to molecular mono-layers. This in turn enables much thinner active layers down to a few hundred nanometres and hence shorter distances for the extraction of photogenerated charges [15, 16, 72]. Upon this realization it was then discovered that solar cells using the mixed organo-lead halide $CH_3NH_3PbI_{3-x}Cl_x$ do not even require the electron-transporting mesoporous TiO_2 and in fact work more efficiently with the perovskite deposited on a passive Al_2O_3-scaffold, the conduction band edge of which is lies too high to allow electron injection [14].

From this point on, the further development of perovskite solar cells divided up into two paths pursuing two different designs. The first type may be categorized as a sensitized architecture, where the pure triiodide material $CH_3NH_3PbI_3$ is still deposited on mesoporous TiO_2 [13, 16, 73], whereas the second type abandons the electron-transporting scaffold and relies on the apparently superior charge-extraction performance of the mixed halide material $CH_3NH_3PbI_{3-x}Cl_x$ [14, 15, 72]. The benefit of the latter approach arises from the fact that the potential drop required by the electron injection step can to some extent be avoided and the open circuit voltage of the cell can thereby be increased [14]. Alternative to replacing mesoporous TiO_2 by Al_2O_3 for this purpose it has later been demonstrated that devices based on planar heterojunction architectures without any mesostructured scaffold can be realized with at least equally high power conversion efficiencies [15, 72, 74]. This again opens up possibilities for using a wider range of fabrication routes, such as vapour deposition techniques, which are capable of producing particularly homogeneous and reproducible films [15].

For both types of perovskite solar cells with and without electron transporter, remarkable progress in device performance has been made within less than two years through careful optimization of the processing routes. At present, the highest published power conversion efficiencies have reached the mark of 15 % for both types [15, 16]. Interestingly the composition of the main functional materials (HTM, absorber, ETM) have not changed during this time.

While earlier research on organic-inorganic perovskites had a rather broad scope encompassing a large variety of material sub-classes, the recent surge of interest stimulated by the development of perovskite solar cells has focussed the greatest part of the attention on the two record-efficiency materials $CH_3NH_3PbI_3$ and $CH_3NH_3PbI_{3-x}Cl_x$. Yet, the understanding of the fundamental optical and electronic properties of these systems is still at an early stage and a complete and detailed picture of the photo-

voltaic operation of perovskite solar cells is still emerging. In this work, ultrafast time-resolved studies of charge-carrier dynamics in $CH_3NH_3PbI_3$ and $CH_3NH_3PbI_{3-x}Cl_x$ are conducted to reveal the fundamental transport and recombination processes in these materials. Results obtained through THz- and photoluminescence spectroscopy are presented, which contribute to a better understanding of how organo-lead halide perovskites achieve such ground-breaking performance in solar cells and where further potential improvements are possible. The following section briefly reviews the current state of knowledge and the most important open questions in respect of the optoelectronic properties of the materials.

2.2.1 Optoelectronic Properties of Organo-Lead Halide Perovskites

Perhaps the most relevant figure among the optoelectronic properties of a photovoltaic absorber material is its intraband absorption onset. For the compounds of interest here, in which exciton binding energies are relatively small (see below), the absorption onset is located close to the band gap energy. In Table 2.1, reported values are summarized for the two materials, $CH_3NH_3PbI_3$ and $CH_3NH_3PbI_{3-x}Cl_x$, which are in the focus of this study, as well as for related materials with different organic cation, metal-ion or halide-ion. In most of the cited studies, band gap energies were obtained from optical absorption spectra, which is subject to uncertainties as an exact physical description of the nature of the onset is not yet available. Although band structure calculations unanimously indicate a direct band gap [75, 76, 77, 78] (see also Figure 8.1) and provide a description of the curvature of the band edges, which allows for a simulation of the absorption onset, the effects of excitonic enhancements cannot be appropriately accounted for at this point. Therefore, a rigorous distinction between the position of the absorption onset and the bandgap energy is not applied in this context.

Material	E_g	Method / Ref.	Comment
$\mathbf{CH_3NH_3PbI_3}$	1.678	OA [79]	
	1.65	OA / PL [80]	
	1.52 - 1.54	PC [81]	
	1.5	OA [13]	on mesoporous TiO_2
	1.54	OA [82]	
	1.57	OA [83]	
	1.57	OA [84]	
	1.6	OA [85]	
$\mathbf{CH_3NH_3PbI_{3-x}Cl_x}$	1.55	IPCE [14]	
	1.6	OA [85]	
	1.6	OA this work	
$\mathbf{CH_3NH_3PbBr_3}$	2.33	OA / PL [80]	
	2.35	OA [86]	
	2.29	OA [84]	
$\mathbf{CH_3NH_3PbCl_3}$	3.12	OA / PL [80]	
	3.11	OA [86]	
$\mathbf{FAPbI_3}$	1.48	OA [83]	
$\mathbf{CH_3NH_3SnI_3}$	1.20 - 1.28	OA [82]	dep. on preparation method

Table 2.1: Overview of the band gap energies (or optical absorption onsets) (E_g) of $CH_3NH_3PbI_3$, $CH_3NH_3PbI_{3-x}Cl_x$ and related 3D-organic-inorganic perovskites. Acronyms: OA - optical absorption, OR - optical reflectance, PC - photocurrent, IPCE - incident photon conversion efficiency, PL - photoluminescence, FA - formamidinium.

It has been demonstrated that the absorption onset can be continuously tuned through synthesis of the mixed halides $CH_3NH_3PbI_{3-x}Br_x$ [84] and $CH_3NH_3PbBr_{3-x}Cl_x$ [86] with the appropriate mixing ratio x. This does however not appear to be possible in the case of $CH_3NH_3PbI_{3-x}Cl_x$, where it was observed that only a small amount of chlorine on the order of a few percent can be incorporated into $CH_3NH_3PbI_3$, before a second phase of $CH_3NH_3PbCl_3$ is segregated [85]. For this reason the absorption onset of the mixed halide compound is practically the same as for the pure triiodide. The determination of only a small fraction of chlorine in $CH_3NH_3PbI_{3-x}Cl_x$ is also remarkable given the strongly enhanced charge collection capabilities observed.

The ideal value of the bandgap energy for a solar cell with a single absorbing transition is given by the *Shockley-Queisser-Limit* [18]. Under illumination by an AM1.5 solar spectrum the ultimate (i.e. highest theoretically possible) power conversion efficiency of 33.7 % can be attained by a device with an absorption onset at 1.34 eV *. With regards to bandgap optimization, $CH_3NH_3PbI_3$ is hence the ideal choice among the methylammonium lead halides. Whether a major shift of the attention to $FAPbI_3$ or $CH_3NH_3SnI_3$ as absorbers with an even more ideal bandgap is likely to occur in the near future depends on many other factors determining the suitability of the materials for photovoltaic device applications, such as long-term stability under operating conditions. Note that $CH_3NH_3SnI_3$ comes with the additional advantage of not containing the toxic element lead.

As mentioned before, the perhaps most crucial advantage of perovskite absorbers over sensitizing dyes is their semiconducting behaviour, which strongly facilitates charge extraction. Hence, two further very relevant quantities for their photovoltaic application are their charge-carrier mobility and lifetimes. These properties are in the main focus of this work on lead-halide perovskites. At the time the experimental studies for this thesis commenced, very little knowledge on charge-carrier dynamics in

*The original publication states an ultimate efficiency of 44 % for an absorption onset at 1.1 eV based on a black body radiation spectrum at $T = 6000$ K.

$CH_3NH_3PbI_3$ and $CH_3NH_3PbI_{3-x}Cl_x$ existed. However, due to the surge of research interest in this field, several other studies aimed at similar questions were conducted very recently by other groups. The most important results shall be summarized in the following. *Stoumpos et al.* reported very detailed structural, optical and electrical data on bulk poly- and single-crystalline samples of several organic-inorganic iodide perovskites including $CH_3NH_3PbI_3$ and $CH_3NH_3SnI_3$ [82]. Among these, electron mobilities of 66 $cm^2/(Vs)$ for $CH_3NH_3PbI_3$ and 2320 $cm^2/(Vs)$ for $CH_3NH_3SnI_3$ were determined by means of Seebeck- and Hall-Effect measurements. *Stranks et al.* investigated the decay time and quenching of photoluminescence emission due to hole or electron transfer from the perovskite to an adjacent layer of spiro-OMeTAD or PCBM, respectively [87]. The authors modelled the carrier diffusion across the distance from the point of photoexcitation to the interface, where the recombination-preventing charge transfer occurs. With additional knowledge of the recombination lifetimes of the material in absence of attached quenching layers, carrier diffusion lengths of just over 1 μm in $CH_3NH_3PbI_{3-x}Cl_x$ and just over 100 nm in $CH_3NH_3PbI_3$ could be extracted. The corresponding carrier lifetimes (at low excitation density) are 273 ns ($CH_3NH_3PbI_{3-x}Cl_x$) and 9.6 ns ($CH_3NH_3PbI_3$). Charge-carrier mobilities of 1.8 - 2.3 $cm^2/(Vs)$ ($CH_3NH_3PbI_{3-x}Cl_x$) and 0.47-0.72 $cm^2/(Vs)$ ($CH_3NH_3PbI_3$) can be computed from the diffusion coefficients reported in the article. A similar study of only $CH_3NH_3PbI_3$ coming to very similar results for this material was conducted by *Xing et al.* [88]. It remains unclear from these investigations however, whether the reported diffusion lengths and mobilities are to be ascribed to free electrons and holes or excitons.

Reported exciton binding energies in $CH_3NH_3PbI_3$ range from 19 meV (from temperature-dependent photoluminescence emission) [89] to 37 meV (from the diamagnetic shift of the absorption edge) [90]. For $CH_3NH_3PbI_{3-x}Cl_x$ 55 meV were very recently determined by *D'Innocenzo et al.* from the temperature-dependent width of the lifetime broadened peak created by resonant excitonic enhancement of optical

absorption at its onset [91]. Due to the closeness of these binding energies to the characteristic thermal energy at room temperature ($k_BT \approx 25.2\,\mathrm{meV}$ @ $\mathrm{T} = 293\,\mathrm{K}$), dynamically interchanging populations of both, free carriers and excitons have to be considered. To the present day, a consistent picture of the coexistence of the the two species is still emerging.

2.2.2 Fabrication of Active Layers for Perovskite Solar Cells

Typical perovskite solar cells are composed of the following components (see Figure 2.5):

- *Glass substrate*
- *Transparent electrode*: usually fluorine-doped tin oxide (FTO)
- *Electron-selective contact* (*hole-blocking layer*): usually compact TiO_2
- *Perovskite absorber layer:* predominantly either $CH_3NH_3PbI_3$ on mesoporous TiO_2 (*sensitized mesostructured type*) or $CH_3NH_3PbI_{3-x}Cl_x$ on mesoporous Al_2O_3 (*ETM-free, meso-superstructured type*) or compact $CH_3NH_3PbI_{3-x}Cl_x$ (*ETM-free, flat heterojunction type*)
- *Hole transporter:* usually spiro-OMeTAD
- *Back contact:* e.g. gold, silver or aluminium

In the vast majority of device studies on mesostructured cells, the TiO_2 or Al_2O_3 nanoparticle layer is spin-coated [14, 16, 72], doctor-bladed [13] or screen-printed [73] on top of the hole-blocking layer from a colloidal solution or paste. After drying [72] and, if required, sintering [13], the perovskite precursor solution (CH_3NH_3I and PbI_2 for $CH_3NH_3PbI_3$ or CH_3NH_3I and $PbCl_2$ for $CH_3NH_3PbI_{3-x}Cl_x$ in DMF or γ-butyrolactone), which infiltrates the mesoporous oxide, is deposited in a further spin-coating step [14, 72]. During subsequent annealing at temperatures of about

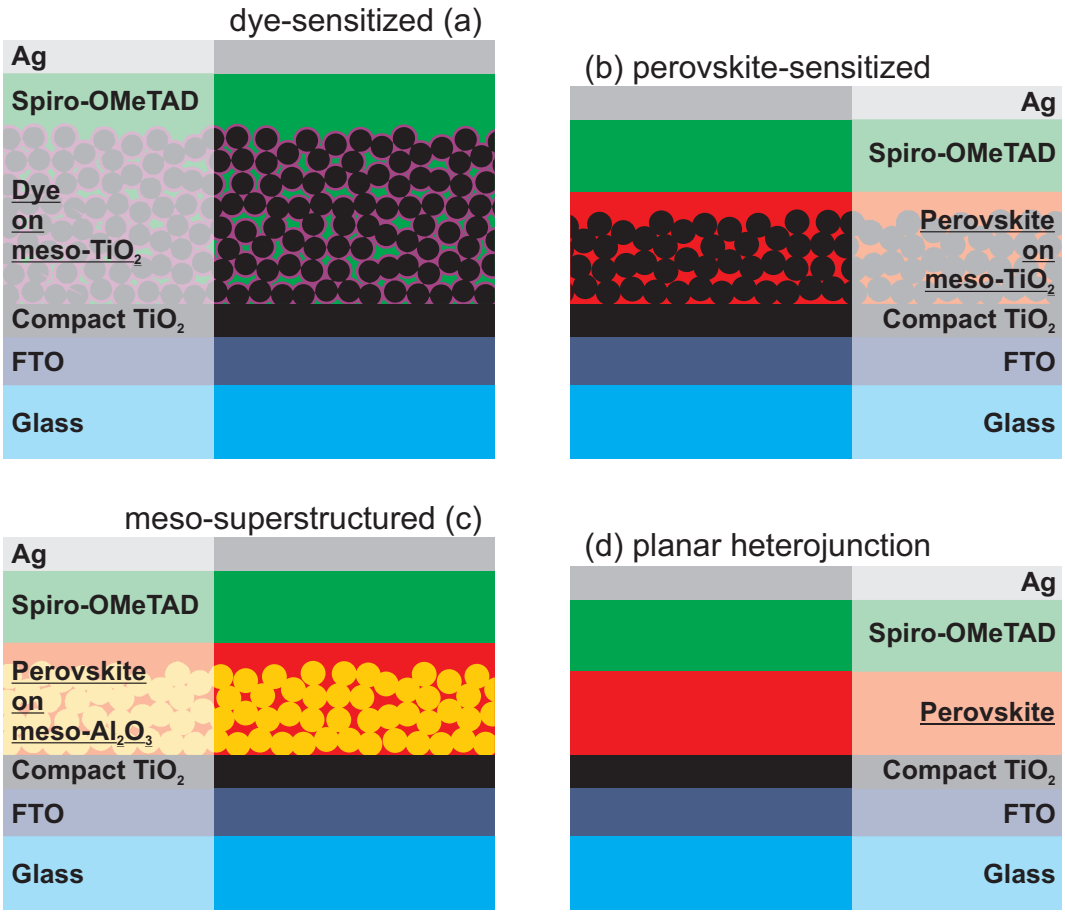

Figure 2.5: Sketches of the structures of a typical dye-sensitized, perovskite-sensitized, meso-superstructured perovskite, and planar heterojunction perovskite solar cells.

100-150 °C the perovskite structure is formed [14, 74]. Alternatively, *Burschka et al.* were able to prepare very high efficiency sensitized mesoporous cells by first spin coating a solution of only PbI_2 and then dipping the dried film into a solution of CH_3NH_3I [16]. To prepare flat heterojunction cells, the precursor is spun directly onto the hole-blocking layer [74, 92].

Solution processing techniques enable low-temperature, large-scale fabrication routes for thin film devices. It is however challenging to control the homogeneity of such films and to avoid defects such as short-circuiting pin-holes arising from de-wetting effects [74]. An alternative process for very high-yield and high-quality perovskite film production is dual-source vapour deposition [15]. The precursors (e.g. CH_3NH_3I and $PbCl_2$ for $CH_3NH_3PbI_{3-x}Cl_x$) are placed in two separate crucibles inside a high-vacuum chamber. These are then heated to individually optimized temperatures to create a vapour phase precursor with appropriate stoichiometry. Through condensation on the rotating substrates the film is grown. Finally, a similar annealing step is required as for solution processed films to allow the perovskite structure to form [15]. Figure 2.6 shows a comparison of scanning electron microscopy images of $CH_3NH_3PbI_{3-x}Cl_x$ films processed from solution and through dual-source evaporation.

In this thesis, attention is devoted to the properties of both, solution-processed (Chapter 5) and vapour-deposited perovskites (Chapters 6 and 7).

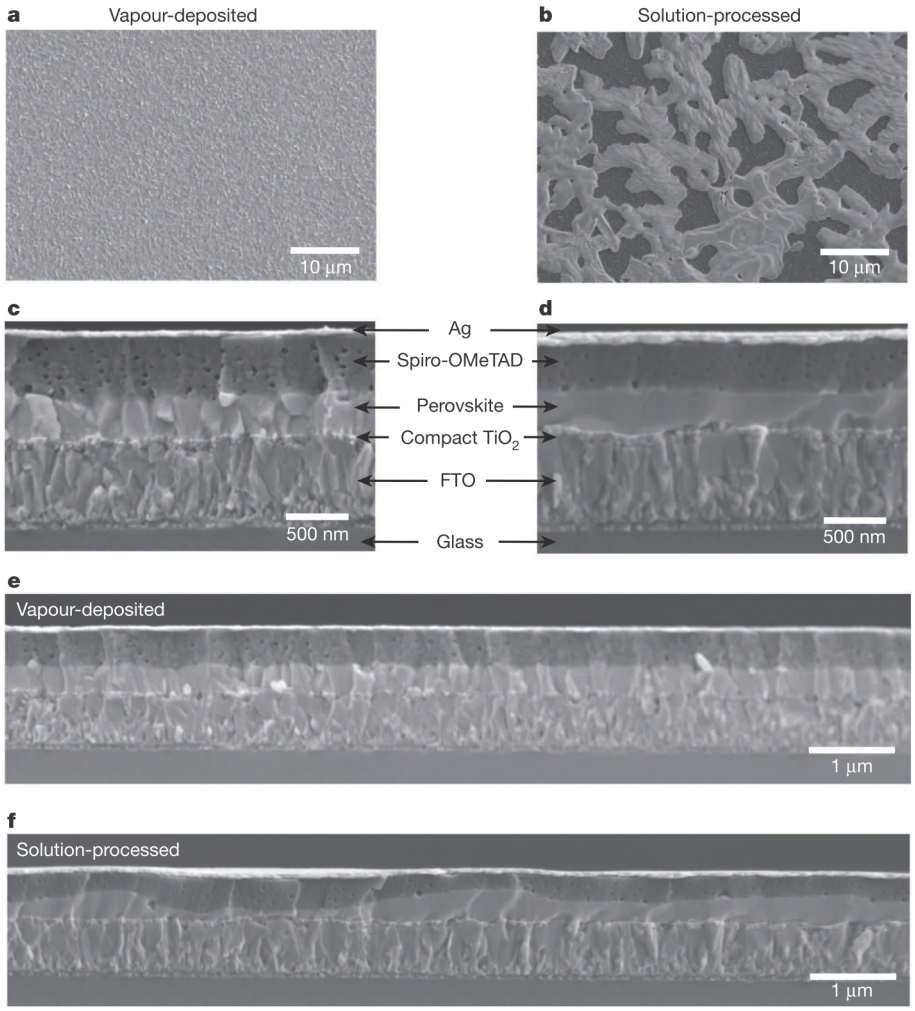

Figure 2.6: Scanning electron microscopy images of $CH_3NH_3PbI_{3-x}Cl_x$-films grown by dual-source evaporation (a, c, e) and from solution (b,d,f). **(a,b)** Top-views of perovskite films on compact TiO_2/FTO/glass (i.e. the bottom half of the full device structure). **(c-f)** Cross-sections of complete devices containing the perovskite as their absorber layer. Reprinted with permission from [15]. Copyright (2013) Nature Publishing Group

3

Experimental Techniques

Under investigation in this work are the dynamics of photoexcited charge carriers related to photovoltaic device operation. To study these processes experimentally, two advanced, *time-resolved* techniques - *THz-* and *photoluminescence spectroscopy* - are used. Both of these are based on a scheme in which the sample is first excited using an (ultra-)short light pulse before a time-resolved measurement of the response of the material is performed. In THz-spectroscopy, the transient conductivity provided by photoexcited charge carriers is probed by a short pulse of THz radiation incident on the sample at a precisely set time-delay with respect to the pump pulse. PL spectroscopy records the light emission from the various decay processes of photoexcited charges. The following sections describe the details of the experimental implementation of these techniques in this work as well as the fundamental steps of the associated data analysis.

3.1 THz Spectroscopy

Electromagnetic radiation can be used as a very versatile contactless probe for electronic processes in solids. Depending on the frequency range used, different interactions can be exploited to obtain information on the electronic state of the system [93, 94]. THz radiation, usually referring to radiation in the frequency interval be-

tween about 100 GHz and 20 THz, interacts strongly with mobile charges and therefore provides a means for studying the dynamics of those processes affecting the charge conductivity of a material [95, 96, 97, 98, 99, 100]. Within the photovoltaics-related context of this thesis these processes include charge injection, trapping and recombination. Furthermore, by excitation or injection of a defined number of free charge carriers into the material, the mobility of these carriers can be determined through measurement of the change in transmittance of THz radiation.

THz spectroscopy constitutes a relatively modern field in experimental materials science, since the generation and detection of THz radiation requires advanced methods often relying on modern electronics or optical technology. Its applications overlap with those of microwave-based techniques, which are also able to probe the dynamics of mobile charges [101]; however, the time resolution of THz spectroscopy, which is ultimately limited by the frequency of the probing radiation, is naturally much better that that of microwaves and hence provides access to ultrafast processes on the time-scale down to a few picoseconds.

3.1.1 Optical-Pump-THz-Probe Spectroscopy

As described in detail in Section 3.1.3, short, single-cycle THz pulses can be readily generated from ultrashort laser pulses in the visible or near-infrared range. This allows to work with precisely temporally correlated THz and optical pulses. In *optical-pump-THz-probe (OPTP)* experiments, an ultrashort optical pulse excites the sample before a THz pulse incident after a well-defined time-delay probes the response of the material. This scheme, which the remainder of this sections describes in detail, is sketched in Figure 3.1. OPTP spectroscopy is widely used in this work to study the decay processes of photoexcited free charge-carrier populations by observing the time-evolution of the photoinduced conductivity.

The detection of THz pulses is also conveniently accomplished in temporal correlation

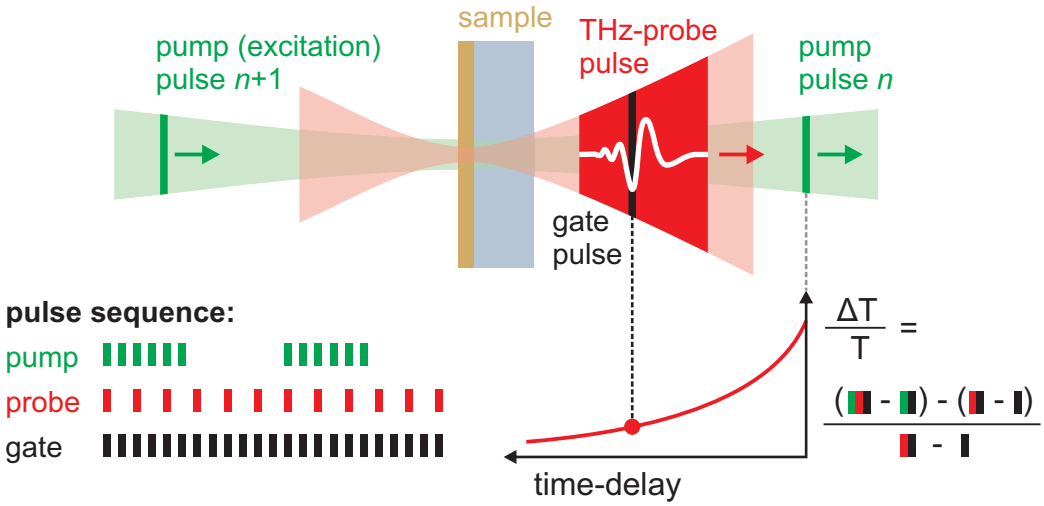

Figure 3.1: Sketch of the principle operation of an optical-pump-THz-probe experiment. Note that a transmitted pump (excitation) pulse is drawn for better illustration of the time-delay. In reality however, the excitation pulse is often fully absorbed in the sample. Furthermore the gate-pulse does not propagate through the sample and is overlapped with the probe pulse behind it (see Figure 3.2).

with ultrashort optical pulses using electro-optic sampling or photoconductive antennas (see Section 3.1.4). These methods allow the full reconstruction of the electric field waveform of the THz pulse in the time-domain. For this reason the described experimental technique relating to generation and detection of THz probe pulses is also often referred to as *THz time-domain spectroscopy (THz-TDS)*. As a consequence, not only the change in the amplitudes but also in the phases of the frequency components of the probe-pulse can be obtained through Fourier Transformation. This provides access to the full complex photoconductivity spectrum. Furthermore analogous to observing the relative conductivity change upon photoexcitation, careful comparison of the dark THz transmission of the sample to an appropriate reference (e.g., in the case of a thin film, an exactly identical substrate) allows direct extraction of the complex dielectric function in the THz range.

3.1.2 Data Analysis

For a thin slab of material with thickness $d \ll \lambda$ the complex sheet conductivity can be calculated from the relative photoinduced THz transmission change $\Delta T/T = (T_{\text{illuminated}} - T)/T$ using the relation [102]

$$\Delta S = -\epsilon_0 c(n_A + n_B)\left(\frac{\Delta T}{T}\right). \tag{3.1}$$

Here, T and $T_{\text{illuminated}}$ are the transmitted THz electric fields of the sample in the dark and after photoexcitation, respectively; n_A and n_B are the refractive indices of the media surrounding the thin film (usually vacuum $n_{\text{vac}} = 1$ and the substrate material $n_{\text{z-quartz}} = 2.13$).

In order to derive the charge-carrier mobility μ from the photoinduced sheet conductivity, the number of photo-excited charge carriers N needs to be determined using

$$N = \phi\frac{E}{hc}(1 - R_{\text{pump}})(1 - T_{\text{pump}}) \tag{3.2}$$

Here, E is the energy contained in an optical excitation pulse of wavelength λ, R_{pump} is the reflectivity of the sample at normal incidence of the excitation beam, T_{pump} the (small) fraction of light transmitted through the sample and ϕ is the ratio of free charge carriers created per photons absorbed, commonly referred to as the photon-to-charge branching ratio, which is technically undetermined in the experiment and related to factors such as the exciton binding energy in the material. The charge-carrier mobility μ is given by

$$\mu = \frac{\Delta S A_{\text{eff}}}{Ne} \tag{3.3}$$

where A_{eff} is the effective area of the overlap of optical pump and THz probe pulse (taking into account the spatial beam profiles), and e is the elementary charge. With ϕ unknown, the quantity which can be directly derived from the experiment is the

effective mobility $\tilde{\mu} = \phi\mu$ where

$$\phi\mu = -\epsilon_0 c(n_A + n_B)\frac{A_{\text{eff}}hc}{Ee\lambda(1-R_{\text{pump}})(1-T_{\text{pump}})}\left(\frac{\Delta T}{T}\right) \tag{3.4}$$

Because $0 \leq \phi \leq 1$, the effective mobility represents a lower limit, which becomes identical to the actual mobility for full photon to free carrier conversion. The determined charge-carrier mobility usually arises from the contributions of both electrons and holes, which often cannot be separated. Therefore, the extracted mobility value is, if not stated otherwise, the sum of electron and hole mobilities. To allow accurate determination of $\phi\mu$ it must be ensured that excitation conditions are in the linear regime, i.e. the initial amplitude of the THz response is proportional to excitation fluence. At strong excitation, nonlinear processes such as two-photon absorption usually create a sub-linear dependence.

The experimentally obtained THz conductivity covers the frequency range contained in the probe pulse, which in this work extends to 0.2-0.3 THz on the low end and 2-3.5 THz on the high end depending on the combination of emitter and detector in use. The response of most materials over this range shows a frequency dependence, which reveals valuable information about the nature of charge transport and the influences it is limited by. In order to obtain the complex frequency spectrum of the THz conductivity $\sigma(\omega)$ with a maximum bandwidth of $\omega_{\max}$ and a resolution of $\delta\omega$ one has to acquire the transmitted THz waveforms in the time domain $\hat{T}(t)$ and $\hat{T}_{\text{illuminated}}(t)$ over a time interval of $\Delta t \geq 1/\Delta\omega$ with a time-step of $\delta t = 1/(2\omega_{\max})$. The conductivity spectrum can then be computed by applying the Inverse Fourier Transform:

$$\sigma(\omega) = \frac{\Delta T(\omega)}{T(\omega)} = \frac{\mathcal{F}^{-1}[\Delta\hat{T}](\omega)}{\mathcal{F}^{-1}[\hat{T}](\omega)} = \overline{\left(\frac{\mathcal{F}[\Delta\hat{T}](\omega)}{\mathcal{F}[\hat{T}](\omega)}\right)} \tag{3.5}$$

The *inverse* transform is applied as most of the literature uses a definition of the conductivity $j(\omega) = \sigma\omega E(\omega)$ based on a time-dependent electric field expressed as

$\hat{E}(t) = \int E(\omega)\mathrm{e}^{-i\omega t}\,\mathrm{d}t = \mathcal{F}[E](t)$ (i.e. where the transition from the frequency- to the time-domain is defined through the *non-inverse* transform).

Within the limits of time-frequency uncertainty $\Delta t \geq 1/\Delta\omega$, conductivity spectra are acquired at specific pump-probe time-delays τ. For the determination of the transient photoconductivity, i.e. $\Delta T/T$ as a function of the time-delay τ, in general full spectra have to be recorded over a range of time-delays to obtain the individual transients for every frequency component. However, if only negligible changes in the spectral shape are observed over the investigated time-delay interval, a frequency-averaged transient can be established by measuring the THz transmission change $\Delta\hat{T}(t)$ at a fixed point t within the waveform. Usually the point of maximum electric field is chosen for this purpose.

As mentioned at the end of the previous section, a dark conductivity spectrum of a thin film sample can be obtained in an analogous way to a photoconductivity spectrum by measuring the THz electric field transmission of the sample and of the appropriate reference. Equation 3.1 retains its validity with $\Delta T = T_{\mathrm{sample}} - T_{\mathrm{ref}}$ and $T = T_{\mathrm{ref}}$. The complex permittivity can then be calculated from the (sheet) conductivity by [103]

$$\epsilon(\omega) = 1 + i\frac{\sigma(\omega)}{\epsilon_0\,\omega} = 1 + i\frac{S(\omega)}{d\,\epsilon_0\,\omega}. \tag{3.6}$$

3.1.3 Generation of Terahertz-Pulses

There are several ways to generate THz pulses from ultrashort light pulses including photoconductive antennas [104], air plasmas [105] or nonlinear optical rectification [106], which differ in duration (and thereby bandwidth) and intensity of the emitted pulse. Moreover the available optical pulse energy and duration play an important role in selecting a suitable generation method and have a potentially high influence on its performance. In this work, optical rectification in one of two available emitter materials is used, which again differ in bandwidth and intensity of the produced pulse.

The first emitter, a 2 mm thick ZnTe crystal produces strong THz emission with a bandwidth of about 2 THz from the output of a regenerative Ti:sapphire amplifier. Alternatively a 450 μm thick GaP crystal is used emitting slightly weaker pulses with a bandwidth however of 3.3 THz. Optical rectification relies upon the nonlinear optical process of difference frequency generation between the frequency components contained in the incident optical pulse. Because of the high line-width of femtosecond pulsed lasers ($\Delta\lambda \approx 25$ nm at $\lambda \approx 800$ nm, corresponding to $\Delta f \approx 12$ THz) the available spectrum of difference frequencies is broad and hence conversion to radiation in the THz frequency is possible.

3.1.4 Detection of Terahertz-Pulses

There is a similar variety of methods for the detection of THz radiation as there is for its generation, analogously achieving different specifications in terms of sensitivity and bandwidth. These again include photoconductive antennas [107] and air-plasma based techniques [108] as well as electro-optic detectors [106], which can in some way be seen as the counterparts to optically rectifying emitters and are based on the same or similar materials. In the present case, ZnTe crystals of different thicknesses are employed for electro-optic detection. For this technique a weak ultrashort optical probe pulse is overlapped with the THz pulse. In the crystal, the THz electric field changes the refractive indices of the birefringent material through the electro-optic effect, causing a proportional rotation of the polarization of the optical probe pulse. By adjusting the relative time-delay of THz and optical pulse, the electric field at selected points in the time-domain waveform of the THz pulse can be measured. This in turn allows to extract amplitude as well as phase information in frequency space. When choosing the thickness of the electro-optic detector, a balance has to be struck between two requirements. First, the total polarization rotation is proportional to the thickness of the detector and hence thicker crystals offer higher sensitivity. However, if the detector is *too thick*, the difference between THz and optical refractive indices

changes the temporal alignment of the pulses during propagation and therefore limits the bandwidth of the detection. On the other hand, if the crystal is *too thin*, the twice internally reflected THz pulse follows the original pulse in quick succession, which limits the available window in the time-domain and hence the frequency resolution of the measurement. The latter issue can be mitigated by using a fused combination of a thick crystal in an inactive orientation (e.g. (100)-ZnTe)) and a thin layer of the same material in its active orientation (e.g. (110)-ZnTe). For early experiments in this thesis, either 0.2 or 2 mm thick (110)-ZnTe was used for THz detection, whereas for later measurements a 0.2 mm (110)-ZnTe layer on a 3 mm (100)-ZnTe crystal was available.

3.1.5 Experimental Setup

The experimental setup for all optical-pump-terahertz-probe experiments is sketched in Figure 3.2. Light pulses of 40 fs duration are emitted by a Ti:Sapphire based regenerative amplifier system. The ultrashort pulses are first generated in a mode-locked Ti:Sa laser and then amplified by passing multiple times through another Ti:Sa crystal, which is pumped by a high energy Nd:YLF laser. The beam is then split into two equally intense parts, one of which is later used for the optical excitation of the sample after a possible wavelength conversion (*pump*). The other part generates the THz probe pulse (*probe*) after a third beam of 2 % of the original intensity is split off to serve the THz detection (*gate*).

Optical excitation of different samples may require light of very different wavelengths depending on the band structure of the contained materials. To meet this requirement, various options for wavelength conversion have been integrated into the setup. An optical parametric amplifier (OPA) combined with two additional mixer stages provides continuous tunability of the output wavelength over a range of 240 nm to 2600 nm. However, when two mixing processes as well as optical parametric amplifi-

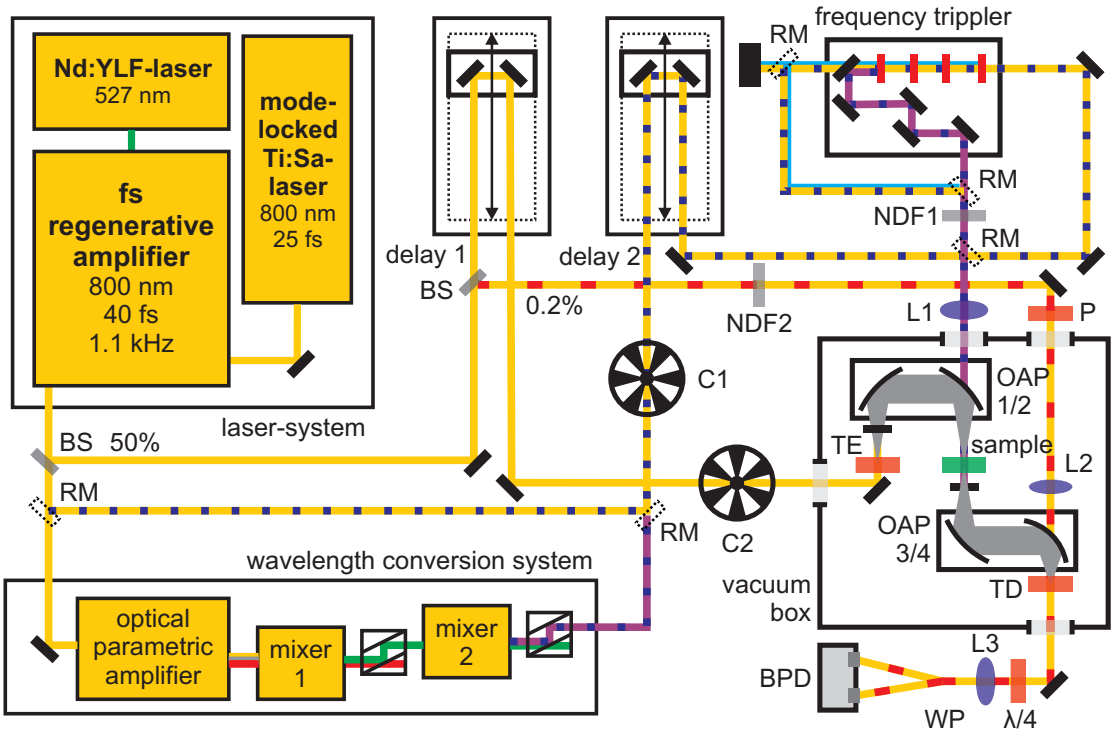

Figure 3.2: Setup of the optical-pump-terahertz-probe experiment. (NDF: neutral density filter, C: chopper, P: polariser, L: lens, TE: THz emitter, TD: THz detector, $\lambda/4$: quarter-wave plate, WP: wollaston prism, OAP: off-axis parabolic mirror, RM: removable mirror, BS: beam splitter, red-dashed beam: gate, blue-dotted beam: pump, solid beam: probe)

cation are involved in the light conversion, which is neccesary to generate wavelengths below 400 nm, the output pulse energy can be prohibitively low. To be able to optically excite samples at low wavelengths with as high energy as possible, the second and third harmonic of the original pulse are alternatively generated directly using beta-barium borate (BBO) crystals (not using the OPA). This provides between five times (3rd harmonic) and 50 times (2nd harmonic) higher pulse energies at the expense of missing tunability. In more detail, the third harmonic (266 nm), which is used for the excitation of TiO_2, is obtained in a two-stage process, where the second harmonic is generated first and mixed with the remaining fundamental wave after polarization rotation and adjustment of temporal overlap. In order to generate a finely adjustable delay (a few fs) of up to 2 nanoseconds between pump-, probe- and gate-pulse, motorized mechanical stages are employed, which create these delays by extending the optical path length of a chosen beam.

Since water has some strong absorption lines in the THz spectral range, the parts of the experiments the THz pulses travel through have to be placed in a sealed box, which is either evacuated or flushed with dry nitrogen. The first component in the path of the probe beam after entering the box is the THz emitter. A PTFE beam blocker stops the remainder of this pulse while transmitting THz radiation with practically no attenuation. Two gold off-axis parabolic mirrors collimate and then focus the THz pulse onto the sample with a profile of about 2 mm FWHM in diameter, overlapped by the larger profile of the optical pump pulse, the diameter of which is controlled by lens L1. Depending on the positions of the delay stages, the pump pulse arrives at a well-defined time before the probe pulse.

Another PTFE block stops any remaining parts of the pump pulse while the THz probe pulse is collimated and focused into the detector crystal by another pair of gold OAPs. With the focus of L2 set close to the detector crystal, it is ensured that the gate beam samples the probe pulse's electric field in a very narrow region right in

the centre of its profile, since the high frequency components possesses a comparably small beam waist.

The gate beam is linearly polarised before it enters the detector crystal, where this polarization is, in general, turned into an elliptic one. A quarter-wave plate is placed in the gate beam such that an unaffected linear polarization would be turned into a perfectly circular polarization. The Wollaston Prism then separates horizontally and vertically polarised components, leading to a levelled illumination of the balanced photodiodes in this case and hence zero output. If a rotation of polarisation is induced by a THz pulse while passing through the detector, the gate beam will leave the QWP with a slightly elliptical polarization with its main axis rotated and hence the balanced photodiodes will measure a difference in the intensity of polarization components.

The signals measured are generally very weak and hard to separate from the noise floor. By using a *lock-in* technique, which is based on modulation of the corresponding excitation onto a chosen carrier-frequency, these signals can be reliably recovered. Here, modulation is achieved by periodically blocking the excitation beam using a rotating light chopper wheel. The carrier frequency component in the output of the photodiodes is then isolated using a *lock-in amplifier*. The OPTP experiment employs two stages of signal lock-in. The generation of the THz-probe pulse is modulated onto a high carrier frequency. In a second stage the effect of the optical excitation of the sample is locked-in using an about ten-times lower frequency.

3.2 Photoluminescence Spectroscopy

Much valuable information about the nature of excited states and their associated decay routes in functional photovoltaic materials can be obtained by observation of the light emission (*luminescence*) during these decay processes [109]. The term *photoluminescence (PL)* describes the emission of light by a material caused by prior photoexcitation. In the simplest case of an ensemble of identical two-level systems

with a dipole-allowed transition between ground- and excited state, a photon is emitted upon every decay event back into the ground state. Time-resolved detection of this emission then allows extraction of the lifetime of the excited state. In more complex cases, multiple decay routes exist, possibly involving several intermediate states. The transitions between these may be partly or fully non-radiative and hence not or only weakly contributing to PL emission. The combination of time- and spectrally resolved detection and tunable excitation helps to isolate individual transitions in order to reconstruct the overall decay process as accurately as possible.

In this work two experimental setups were used to perform PL spectroscopy, one based on a mode-locked Ti:sapphire femtosecond pulse laser and another one using a set of pulsed diode lasers. Both are capable of time- and spectrally resolved detection and provide more or less variability in the photoexcitation of the sample. However, the relevant specifications of the two systems including the available ranges of excitation power, repetition rate, excitation and detection wavelength as well as detection sensitivity and time resolution differ considerably. Before describing the individual setups in detail, a common technique for time-resolved PL detection, time-correlated single photon counting (TCSPC), shall be introduced. TCSPC can be performed on both systems and has been used for all time-resolved PL measurements presented in this thesis.

3.2.1 Time-Correlated Single Photon Counting

Straightforwardly, the time-dependent light emission from a sample may be recorded in a simple way using a fast photodetector (e.g. a biased photodiode or a photomultiplier tube) a wide-band amplifier and a fast analog-to-digital (ADC) converter (e.g. in form of a PC based DAQ system or an oscilloscope). Difficulties with this approach arise when pulsed light sources with high repetition rates are employed (up to 80 MHz in this work), as it becomes technically extremely demanding to record and process

full intensity time traces in the correspondingly short time intervals. Furthermore, the time-resolution of such a system is limited by the rise-time of the detector, the bandwidth of the amplifier and the sampling rate of the ADC. Using very advanced electronics, figures down to a nanosecond may be reached. Better time resolutions of down a few ten picoseconds are possible by moving to an acquisition scheme that solely relies on the timing of the detection of single photons. More importantly such a scheme also reduces the processing effort per cycle from a full intensity time-trace to a single timing-value. Measurements of short delay times can be realized without great technological effort, even in the range of tens of picoseconds. Hence the time-resolution of TCSPC is practically only limited by the rise-time of the photodetector. Note that as single photon detection merely involves registration of the detector output crossing a certain threshold value, accuracies even below the detector rise time are achievable.

In detail the acquisition scheme of TCSPC, which is illustrated in Figure 3.3 works as follows: The PL emission of the sample is attenuated to an extent that the probability of detecting any photons during a single photoexcitation cycle is low (usually below 1 %), i.e. the detection (*counting*) rate is much lower than the repetition rate (of photoexcitation). As a consequence the probability of detecting multiple photons during one cycle is again much lower than detecting a single one. This is essential to the correct operation of the system, because it is generally only possible to time the first incident photon. Multi-photon-events would lead to a bias towards short time-delays as later photons would be systematically ignored. During the course of the acquisition a histogram of the photon arrival times is created, which eventually represents the photoluminescence flux as a function of time. Further to the improved time resolution this method features excellent linearity as the photon flux values are simply a result of countings. The sensitivity of TCSPC (i.e. the ability to measure the time-dependence of very weak PL) is naturally extremely high and only limited by the efficiency with which single photons can be detected. In cases of strong photo-

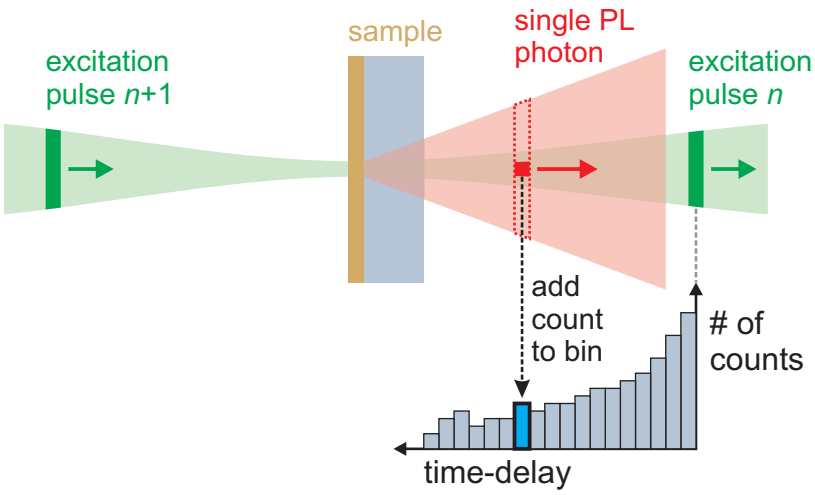

Figure 3.3: Sketch of the principle procedure of time-correlated single photon counting. Note that a transmitted excitation pulse is drawn for better illustration of the time-delay. In reality however, the excitation pulse is often fully absorbed in the sample.

luminescence emission, TCSPC has the disadvantage of always requiring a minimum acquisition time determined by the signal-to-noise level that is supposed to be reached. This is due to the aforementioned limit for the counting rate.

3.2.2 Experimental Setup

The fundamental structure of the two PL spectrometers used in this work is very similar. Both systems can be decomposed into the following fundamental components (See also the sketches of the experimental setups in the following subsections):

1. *Excitation light source:* pulsed laser
2. *Excitation conditioning:* variable attenuator and polariser
3. *Sample chamber:* vacuum cell or cryostat
4. *PL collection optics:* lens or curved mirrors
5. *PL conditioning:* variable attenuator
6. *PL filtering:* analyser, long pass filter and monochromator

7. *Photodetector*

Light pulses from the source are attenuated to the desired pulse energy to control the excitation density in the sample. The PL is (partly) collected by a lens or curved mirror covering a substantial solid angle from the perspective of the sample. A detection attenuator reduces the intensity of the collected PL if required to prevent saturation of the detector or to meet the count rate limit for TCSPC experiments. Excitation light scattered from the sample is blocked by a long-pass filter. If PL at wavelengths very close to or around the excitation light wavelength is to be detected, a long-pass filter cannot be used. In these cases a crossed pair of polarisers in the excitation and detection beam path can provide some filtering of scattered excitation light instead. Finally the collected light is spectrally filtered in a grating monochromator before being measured by a photodetector.

3.2.3 Setup 1: Mode-Locked fs-Laser-Based

The fs-laser based PL spectrometer (Figure 3.4) uses a mode-locked Ti:sapphire laser, optionally in combination with an optical parametric oscillator (OPO) to generate light pulses for the excitation of the sample. The output wavelength of the laser itself is continuously tunable between 690 nm and 1040 nm. Pulses of an energy of up to ∼30 nJ at a duration of 100 fs and a fixed repetition rate of 80 MHz can be generated. If the OPO is used, the wavelength tuning range extends to 345 nm - 2500 nm; however, the maximum achievable pulse energy is reduced depending on the chosen wavelength range (e.g. max 0.3 nJ at 510 nm). A combination of half-wave-plate and polariser provides variable excitation attenuation. A small fraction of the excitation pulse is split off onto a fast photodiode, which provides the timing reference for time-resolved experiments. The sample is either placed in a simple vacuum cell or a liquid helium microscope cryostat (*Oxford Instruments Microstat*). PL is collected, collimated and refocussed by a pair of off-axis parabolic mirrors (OAPs) and, if nec-

essary, attenuated using neutral density filters. Two detectors are available working in conjunction with the grating monochromator - an avalanche photodiode and a silicon CCD. The avalanche photodiode, provides excellent sensitivity, low dark-count rate and a short rise-time allowing time-dependent measurements with up to 35 ps resolution. The silicon CCD does not provide time resolution, but in turn enables the acquisition of a full PL emission spectrum in parallel (while, to perform such an acquisition using the photodiode, a sequential scan of the desired wavelength range is required). In order to be able to record optical transmittance spectra in alternation with the PL during temperature-dependent measurements the setup has been extended. White light from an incandescent lamp (100 W) is guided onto the rear-surface of the sample and the transmitted light collected using the detection optics already available for PL.

3.2.4 Setup 2: Diode-Laser-Based

The diode-laser sources of the second PL spectrometer (Figure 3.5) only offer the four discrete excitation wavelengths 405, 450, 510 and 635 nm. Their maximum output pulse energy of up to ~ 30 pJ is significantly lower than that of the fs-laser. On the other hand the diode lasers offer a widely variable repetition rate from arbitrarily low frequencies up to 40 MHz. Low repetition rates are required for time-resolved measurements of slow processes on correspondingly long time scales. This most importantly includes the determination of long decay lifetimes, where the observation of a sufficiently long interval of the decay trace is necessary for accurate extraction of the lifetime. The perovskite materials investigated in Chapters 5, 6 and 7 for example exhibit photoexcited carrier lifetimes of hundreds of nanoseconds which are far outside the accessible time-scale of 12.5 ns of the fs-laser system. Excitation attenuation is accomplished through a discrete neutral density filter wheel, while a variable aperture in the collimated PL beam is responsible for detection attenuation. The sample is kept in a vacuum chamber. PL from the sample is collected and collimated

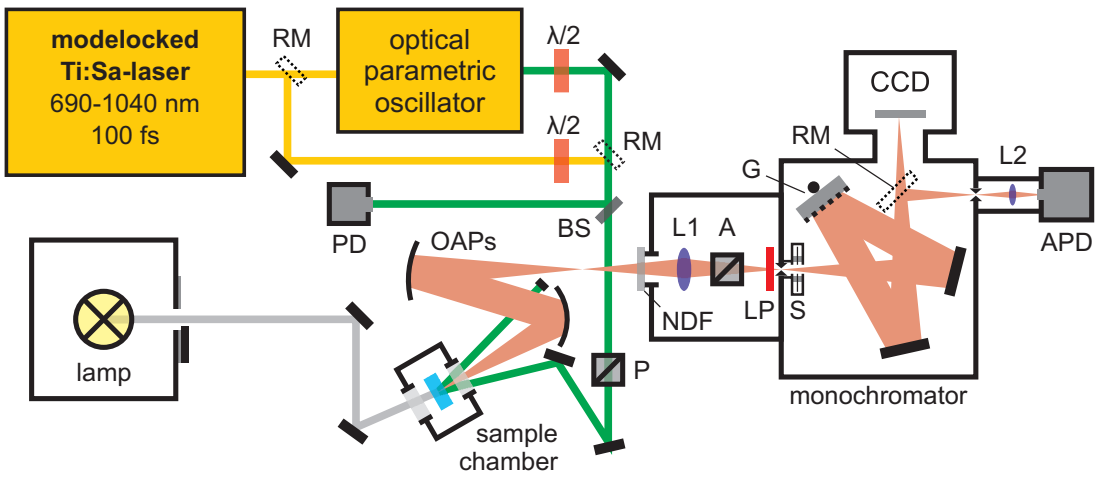

Figure 3.4: Setup of the fs-pulse-laser based photoluminescence experiment. (RM: removable mirror, $\lambda/2$: half-wave plate, BS: beam splitter, PD: photodiode, P: polariser, OAP: off-axis parabolic mirror, NDF: neutral density filter, L: lens, A: analyser, LP: long-pass filter, S: shutter, G: grating, APD: avalanche photodiode)

by a lens and detected by a hybrid photodetector (HPD). In essence an HPD consist of a photocathode from which photoelectrically released electrons are accelerated towards an avalanche diode, where impact ionization induces an amplified current. The achievable time-resolution on the diode-laser based system is about 150 ps.

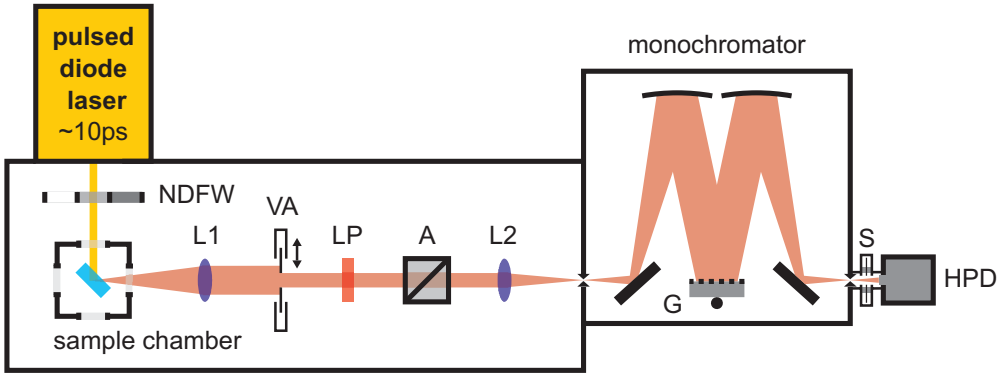

Figure 3.5: Setup of the diode-laser based photoluminescence experiment. (NDFW: neutral density filter wheel, L: lens, VA: variable aperture, LP: long pass filter, A: analyser, G: grating, S: shutter, HPD: hybrid photodetector)

4

Charge-Carrier Dynamics in TiO_2 Nanotubes

During the past ten years, several studies have investigated the capabilities of TiO_2-nanotubes as an alternative to the dominantly employed nanoparticles as electron transport materials (ETMs) in dye-sensitized solar cells (DSSCs). With anodization, a relatively simple and scalable fabrication technique exists for films of highly ordered TiO_2-nanotube-arrays. In Section 2.1.2 it was highlighted that the long-range charge-carrier mobility in nanoporous TiO_2 is dramatically lowered compared to that of the bulk material and that - particularly in solid state DSSCs - reduced diffusion lengths may be a critical limiting factor for device performance. On first sight, nanotubes seem to promise superior charge extraction by providing continuous percolation paths for electrons from the point of injection to the anode contact. It therefore appears sensible to explore the potential of such one-dimensional structures as alternative ETM morphologies. So far however, device studies show that although recombination lifetimes in nanotube based DSSCs under full sun operating conditions surpass those of nanoparticle based ones, record-breaking efficiencies and - most importantly - faster charge collection are not achieved (see Section 2.1.3).

In this chapter, results from optical-pump-terahertz-probe experiments on TiO_2 nanotubes prepared by anodization are presented. These indicate that trapping of elec-

trons occurs on timescales of a few ten picoseconds, which is about 20 times faster than in sintered nanoparticles at similar photoexcitation density. The observations are interpreted within a model involving shallow traps, from which thermal detrapping is possible and deep traps, which irreversibly immobilize carriers. The influence of the wall thickness of the tubes, which can be varied through temperature control of the anodization bath, on trapping lifetimes is studied. Finally, it is discussed in how far this phenomenon can be responsible for the less-than-ideal charge transport in devices.

4.1 Experimental Details

4.1.1 Samples

TiO_2 nanotube films were prepared on quartz substrates by anodization at different temperatures and subsequent annealing. The substrates were cleaned in ultrasonic baths of acetone and isopropanol for 30 min each and by oxygen plasma treatment. Using a Surrey Nano-Systems Gamma 1000C sputter coating system, approximately 1 µm of Ti was DC sputtered at 500 °C under an Ar atmosphere at a pressure of 4 mTorr. Afterwards the samples cooled down slowly under high vacuum. Anodization was performed in an ethylene glycol bath with 0.3 wt% NH_4F (Sigma Aldrich) using a Pt counter electrode. Two batches of samples were anodized at a range of temperatures between 5 °C and 55 °C in steps of 10 °C, at an anodization voltage of 20 V and for durations between 1 min and 2 h. Afterwards the samples were rinsed with water and ethanol and dried in air. Since anodization produces amorphous nanotubes, the films were annealed to obtain polycrystalline material. Annealing of the first batch was performed ramping the temperature up to 450 °C at a heating rate of 3 °C/min in ambient atmosphere under observation by means of in-situ x-ray. The second batch was annealed for three hours at 310 °C, which is closely above the crystallization temperature of the anatase phase found in the x-ray study. This batch has

also been checked for complete crystallization by XRD after the annealing process.

At a later stage, the nanotubes were covered in a monolayer of a ruthenium based dye (Z907) by immersion in a solution of 3 mg Z907 in 20 ml ethanol for 18 h (The terms *undyed* and *dyed* are used in this chapter to distinguish between the state of the samples before and after this processing step). In preparation for the dye attachment, the films were heated up to 200 °C in order to remove any surface adsorbed water. After immersion, excess dye was removed by cleaning the samples in acetonitrile. Finally, the dye was removed from one batch of samples again by immersion in base (KOH in ethanol) for 5 h. These samples were then cleaved and sputter-coated in 2 nm of Pt for scanning electron microscopy (SEM) imaging.

A set of reference samples of 20 nm TiO_2 nanoparticles have been prepared by spin-coating a 1:1.5 solution of Dyesol nanoparticle paste in ethanol at 1000 rpm for 10 s followed by 2000 rpm for 40 s on a quartz substrate. The films were then dried and sintered for 30 min at 450 °C. The thickness of the reference samples is about 3 µm as determined by surface profiling.

4.1.2 Scanning Electron Microscopy (SEM)

Top-view and cross sectional SEM images were taken of all samples of the first batch (annealed at 450 °C) after all spectroscopic experiments were completed. A *Hitachi S-4300* microscope was used at an acceleration voltage of 5 kV, an emission current of 10 μA and 14 mm working distance.

4.1.3 THz Time-Domain Spectroscopy

An optical-pump-THz-probe setup based on a regenerative Ti:Sapphire amplified femtosecond laser as described in Section 3.1 was used. Terahertz pulses were generated by optical rectification in a 2 mm thick ZnTe crystal and detected by electro-optic sampling in another ZnTe crystal of 0.2 mm thickness. Undyed TiO_2-nanotubes were ex-

cited directly at a wavelength of 266 nm corresponding to a photon energy of 4.66 eV, which is well above the bandgap of anatase-TiO_2 (3.2 eV [41, 110]). Pulses of this wavelength are generated by third harmonic generation (THG) [111] of the laser output. Dyed samples on the other hand were excited at 545 nm using the output of the optical parametric amplifier (OPA). The corresponding photon energy of 2.27 eV lies well below the bandgap of anatase, but is at the same time strongly absorbed by the dye Z907. If not explicitly stated otherwise, measurements have been performed with the sample in an evacuated chamber, at a pressure in the range of 10^{-2} mbar to 10^{-1} mbar.

4.2 Results and Discussion

4.2.1 Morphological Characterization

Figure 4.1 shows a typical SEM cross sectional image of one of the nanotube films. The most notable feature is that the morphology of the tubes differs from the top, where the surface is smooth, to the bottom, where the tubes exhibit rings similar to a bamboo-stick. This phenomenon can be observed on all samples with the exception of the one anodized at 55 °C; it has been reported before by various groups [59, 60] and is commonly termed *ripples* (while *bamboo-rings* generally refers to a more pronounced, intentionally created feature). Ripples have been associated with regular current fluctuations, the occurrence and amplitude of which depends on the acid concentration in the anodization bath [112]. Analysis of the full set of images reveals a pore-to-pore distance of about 80 nm (independent of the tube wall thickness as reported in [61]) and tube lengths between 1 µm and 2 µm for all samples.

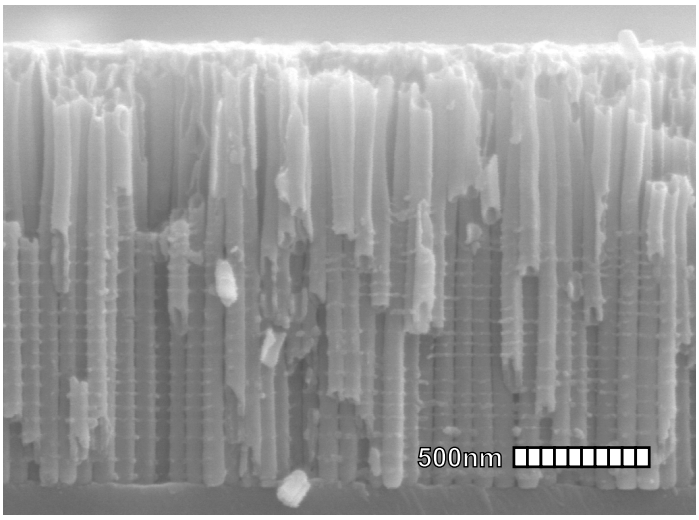

Figure 4.1: SEM cross sectional image of TiO_2 nanotubes anodized at 45 °C. The image has been taken at $V_{acc} = 5$ kV after sputtering a 2 nm layer of platinum onto the cross sectional area.

4.2.2 Decay Dynamics - Undyed TiO_2 Nanotubes

As a starting point for the study of the early-time carrier decay dynamics in TiO_2 nanotubes, the excitation-density dependent transient THz photoconductivity was recorded. Previous reports have already shown that the response of photoexcited TiO_2 to a THz probe [53, 113] or a microwave probe [114] is dominated by the contribution from electrons. Further evidence for this will also be presented later in this chapter.

Figure 4.2 shows the photoinduced THz response of a TiO_2 nanotube film as a function of time after excitation with fluences between 13 and 126 $\mu J/cm^2$. Here, the term *THz response* is used in short for the change in electric field transmission, which according to Equation 3.1 is proportional to the conductivity of the probed thin film, i.e. the product of free carrier density n and mobility μ. In general, changes in both charge-carrier mobility and concentration determine the shape of the THz transmission transient. However, the most plausible cause for the partially rapid dynamics displayed by the curves in Figure 4.2 is a decay of free carrier population through mechanisms like trapping or recombination. This interpretation is supported

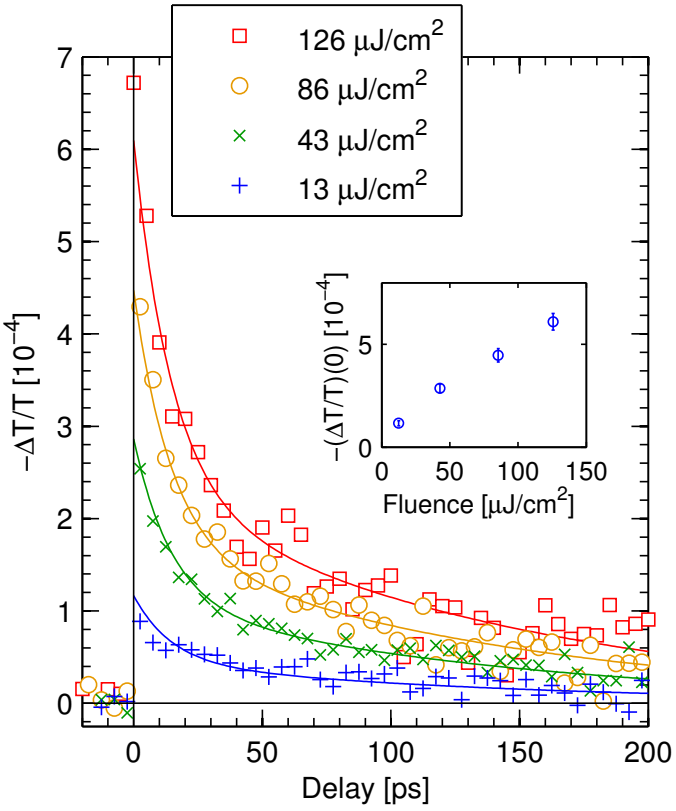

Figure 4.2: THz transmission transients (266 nm excitation in vacuum) of undyed TiO_2 nanotubes (T_{ano} = 5 °C) for a range of excitation fluences. Symbols: Experimental data. Lines: Simultaneous fits to Equation 4.2 as described in the text. Inset: Amplitudes of the initial THz response vs. excitation fluence.

by the invariance of the THz photoconductivity spectra taken at different pump-probe delays, which are shown in Section 4.2.5. If there was a change of the intrinsic mobility on the investigated timescale, e.g. due to carrier cooling effects or a reduced influence of carrier-carrier scattering processes, its frequency dependence would be likely to change as well. The data however does not show any changes of the spectral shape with increasing pump-probe delay. Here, an approach is therefore made to interpret the THz transmission transients on the assumption that their shape is predominantly determined by the decay of carrier concentration while the carrier mobility is taken to be constant, at least over the picosecond-to-nanosecond observation window. The most striking feature of the data in Figure 4.2 is a rapid population decay within tens of picoseconds irrespective of the excited carrier density, which indicates that it arises from a mono-molecular process such as carrier trapping. The data additionally shows a longer-lived component; hence a simple mono-exponential decay function alone does not provide an adequate model for extraction of physically sensible lifetimes.

It has been well established that charge transport in nanostructured TiO_2 is inhibited by frequent trapping-detrapping events [115, 116, 117, 118] (see also Section 2.1.1). Such trapping events are very likely to be reflected in the transient THz response as already observed for TiO_2 nanoparticles [53]. Further studies on nanoparticles using photoluminescence and visible/IR transient absorption [119, 120] have suggested that the carrier recombination process also involves deep trap sites assignable to surface states or defects such a oxygen vacancies [121, 122], to which shallowly trapped carriers can transfer, but from which no thermal escape is possible. On the basis of these insights a model is formulated, which describes the observed decay dynamics in terms of trapping, detrapping and deep-trapping processes as expressed by the

following equations:

$$\begin{aligned}\frac{\mathrm{d}}{\mathrm{d}t}n_{\mathrm{fr}}(t) &= -k_{\mathrm{tr}}n_{\mathrm{fr}}(t) + k_{\mathrm{dtr}}n_{\mathrm{tr}}(t) - k_{\mathrm{deep}}n_{\mathrm{fr}}(t)\\ \frac{\mathrm{d}}{\mathrm{d}t}n_{\mathrm{tr}}(t) &= k_{\mathrm{tr}}n_{\mathrm{fr}}(t) - k_{\mathrm{dtr}}n_{\mathrm{tr}}(t) - k_{\mathrm{deep}}n_{\mathrm{tr}}(t)\end{aligned} \tag{4.1}$$

Here, n_{fr} is the density of free electrons and n_{tr} the density of shallowly trapped electrons. Furthermore, k_{tr} represents the shallow-trapping rate, k_{dtr} the detrapping rate (from shallow traps) and k_{deep} the deep-trapping rate. This system of equations can be solved analytically resulting in a bi-exponential expression for the free-electron density:

$$\begin{aligned}n_{\mathrm{fr}}(t) &= \frac{n_{\mathrm{fr}}(0)}{k_{\mathrm{tr}}+k_{\mathrm{dtr}}}\left(k_{\mathrm{tr}}\,e^{-(k_{\mathrm{dtr}}+k_{\mathrm{tr}}+k_{\mathrm{deep}})\,t} + k_{\mathrm{dtr}}\,e^{-k_{\mathrm{deep}}\,t}\right)\\ n_{\mathrm{tr}}(t) &= \frac{n_{\mathrm{fr}}(0)}{k_{\mathrm{tr}}+k_{\mathrm{dtr}}}\left(-k_{\mathrm{tr}}\,e^{-(k_{\mathrm{dtr}}+k_{\mathrm{tr}}+k_{\mathrm{deep}})\,t} + k_{\mathrm{tr}}\,e^{-k_{\mathrm{deep}}\,t}\right)\end{aligned} \tag{4.2}$$

The solution was simultaneously fitted to the THz photoconductivity transients for all excitation fluences, i.e. the entire dataset shared a single common fit parameter for each rate constant. Figure 4.2 displays this fit as solid lines showing that these are able to reproduce the shape of the decays well. The resulting rate constants, expressed in terms of lifetimes are: $\tau_{\mathrm{tr}} = 1/k_{\mathrm{tr}} = (27 \pm 6)\,\mathrm{ps}$, $\tau_{\mathrm{dtr}} = 1/k_{\mathrm{dtr}} = (43 \pm 10)\,\mathrm{ps}$, and $\tau_{\mathrm{deep}} = 1/k_{\mathrm{deep}} = (140 \pm 16)\,\mathrm{ps}$. In the scenario described by the model the simultaneous processes of trapping and detrapping lead to a relaxation into an equilibrium. Eventually, on a longer timescale, all carriers are immobilised irreversibly in deep traps.

In the next step, the observed carrier recombination dynamics in TiO_2 nanotubes are compared to those in sintered TiO_2 nanoparticles. Figure 4.3 displays THz photoconductivity transients for both morphologies. It is immediately visible that under comparable excitation conditions, the early time decay of the free electron population

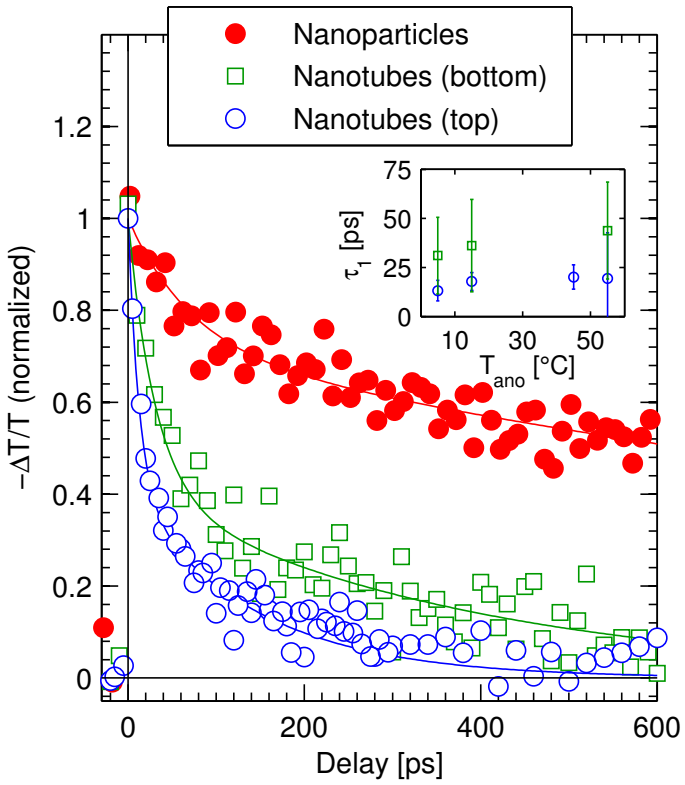

Figure 4.3: THz transmission transients (-dT/T, normalized) after excitation with a 40 fs/266 nm light pulse in vacuum. Open circles: TiO_2 nanotubes (T_{ano} = 5 °C, undyed, excitation fluence: 125 μJ/cm^2), excited from their free side. Open squares: TiO_2 nanotubes (T_{ano} = 5 °C, undyed, excitation fluence: 100 μJ/cm^2), excited from the substrate side. Closed circles: Sintered TiO_2 nanoparticles (Dyesol, 20 nm, undyed, excitation fluence: 125 μJ/cm^2). Lines: Fits to Equation 4.2 (bi-exponential) as described in the text. Inset: Shorter decay time constant from fit $\tau_1 = \tau_{tr} + \tau_{dtr} + \tau_{deep}$ for TiO_2 nanotubes anodized at different temperatures, symbol assignment as in (a).

is at least an order of magnitude faster in nanotubes, which suggests a much higher density of trap states present in this material.

The variations in the fast trapping lifetimes are compared between the top and the bottom part of the nanotubes as well as between samples to different tube wall thicknesses. A separate investigation of the top and bottom parts is possible due to the fact that the absorption depth of the excitation light into the films is only about 70 nm compared to a film thickness of the order of 1 μm.* As shown in Figure 4.3, slightly, but not significantly slower trapping ($\tau_{\mathrm{tr}} = (57 \pm 40)\, ps$) is found in the bottom parts. The inset compares the results from tubes grown at different anodization temperatures, which allows a variation of the tube wall thickness over about a factor of 2 as demonstrated in [61] (higher T_{Ano} leads to thinner walls). Unfortunately, due to the critically low signal to noise ratio achievable with reasonable experimental effort, only trends can be extracted from this comparison. A systematic dependence of lifetimes on wall thickness is not observed, particularly not in a way that thinner walls (i.e. higher T_{Ano}) lead to faster decay as it might be expected for a predominant concentration of traps at the surfaces of the tubes. The trend of slower trapping in the bottom parts of the tubes appears to be confirmed across different wall thicknesses. As the SEM image in Figure 4.1 indicates, the geometrical differences along the growth direction of the tubes are very small, hence an explanation of the change in trapping lifetime is more likely to relate to the growth process itself. Such a connection could e.g. exist through the longer exposure of the top parts to the ammonium fluoride containing bath introducing impurities into the material [124, 125], which may be responsible for the incorporation of trap states. Alternatively a variation in ionic concentrations in the bath during the procedure could have a similar effect.

Since it is well known that exposure to oxygen can cause tremendous DC conductivity

*An absorption depth of about 35 nm has been reported for single crystalline anatase [123] and it is assumed that the absorbance approximately scales with the volume filling fraction, which is about 0.5 for the NT samples studied here).

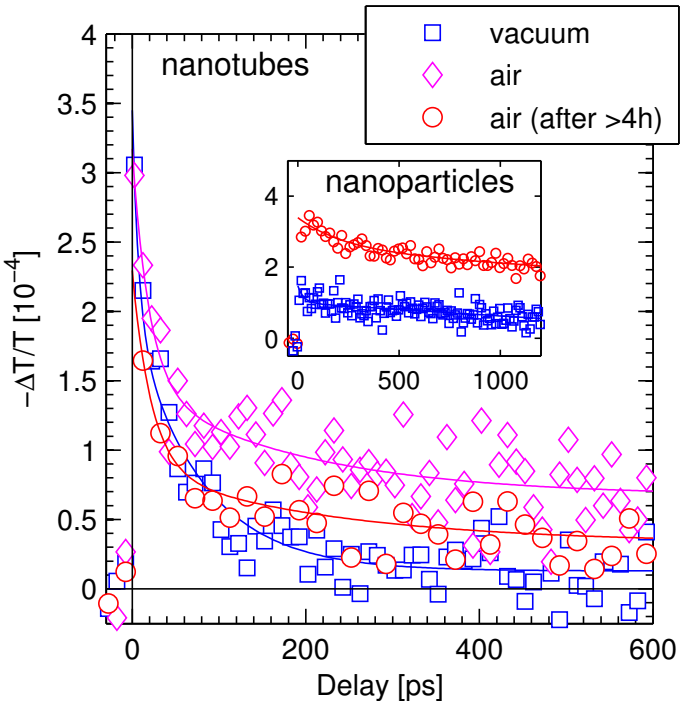

Figure 4.4: Comparison of THz transmission transients (266 nm excitation at fluence: 55 $\mu J/cm^2$) of undyed TiO_2 nanotubes in vacuum (blue squares), immediately after exposure to air (pink diamonds) and after at least four hours of exposure to air (red circles). Inset: Result of the same experiment on sintered, undyed TiO_2 nanoparticles.

changes in TiO_2 [122, 126], measurements under ambient air were performed in order to reveal its influence on the THz response. Unless explicitly stated otherwise, all other OPTP experiments have been performed under vacuum ($< 10^{-1}$ mbar). The study of the influence of air is additionally useful considering that only limited control can be exerted over how much oxygen is adsorbed to the nanotube surface at the time when the sample chamber is evacuated.

Measurements were taken in air at atmospheric pressure, at low vacuum (10^{-1} mbar) and at high vacuum (10^{-4} mbar). Changes under exposure to the UV pump pulses were continuously monitored. No changes in the THz transmission transients were observed between a pressure of 10^{-1} mbar and even lower pressures (down to 10^{-5} mbar). However, comparing measurements taken in air at atmospheric pressure ($\sim$30 % relative humidity) to those at 10^{-1} mbar or less as shown in Figure 4.4, it is found that already during the first acquisition after exposure to atmospheric air, a long-lived component (with a lifetime much longer than the experimentally accessible 1.2 ns) emerges in the decay curves. Later, on timescales of tens of minutes to a few hours, it is also observed that the amplitude of the THz response decreases. This change is reversible on slightly longer timescales (several hours) under exposure to the 266 nm excitation light.

The interaction of ambient gases with TiO_2 surfaces is complex and has been subject to numerous studies [122, 127, 128]. In particular adsorbed oxygen has been found to cause tremendous changes to carrier dynamics in TiO_2 due to its ability to scavenge free electrons. It can thereby turn an oxygen deficient n-doped surface into a p-doped one. Desorption of oxygen can occur after electron capture and is hence facilitated by UV irradiation [129]. The observed drop in THz conductivity under air-exposure may be caused by a reduction of the incident photon-to-free-charge conversion ratio ϕ. This may occur through several potential mechanisms such as ultrafast immobilization of carriers on the sub-ps timescale, the emergence of additional absorbing states and

transitions which do not lead to the creation of free charges. With respect to the slow emergence of a long-lived component under oxygen exposure, diffusion processes of oxygen (and titanium) atoms from and into the bulk of the material may cause changes of the concentration of deep trap states arising from oxygen vacancies [122, 130, 131]. The data obtained in this work is not sufficient to point out the exact mechanism causing the observed changes, but with respect to the present study of electron lifetimes it is concluded that, in spite of the changes caused by the presence of air, the initial fast trapping process still appears to be active as the cause for the immobilisation of a large part of the initial free carrier population on an unaltered timescale. In particular it is noted that an influence of surface doping on fast trapping in TiO_2 nanotubes is therefore unlikely.

4.2.3 Decay Dynamics - Dye-Sensitized Nanotubes

After up to this point, electrons in TiO_2 have been excited directly from the valence band by the pump pulse, the attention is now turned to dye-sensitized nanotubes as they would be used in actual dye-sensitized solar cells. In these, excitation takes place in the dye and electrons are subsequently injected from the dye into the TiO_2-nanostructure [132]. A wavelength of 545 nm is chosen for photoexcitation of sensitized samples, which corresponds to a photon energy of 2.27 eV well below the bandgap of anatase TiO_2. This way it is ensured that no direct excitation of the nanotubes themselves takes place. The most important difference in this situation is that no holes are generated in the TiO_2 and recombination can only take place with the oxidized dye at the surface.

THz-conductivity decay curves on dyed samples for a range of excitation fluences are shown in Figure 4.5(a). The fluence dependence of the signal amplitude (at zero pump-probe delay) is linear indicating that charge injection is not limited by saturation effects within the employed range of excitation fluences. The shape of the decay

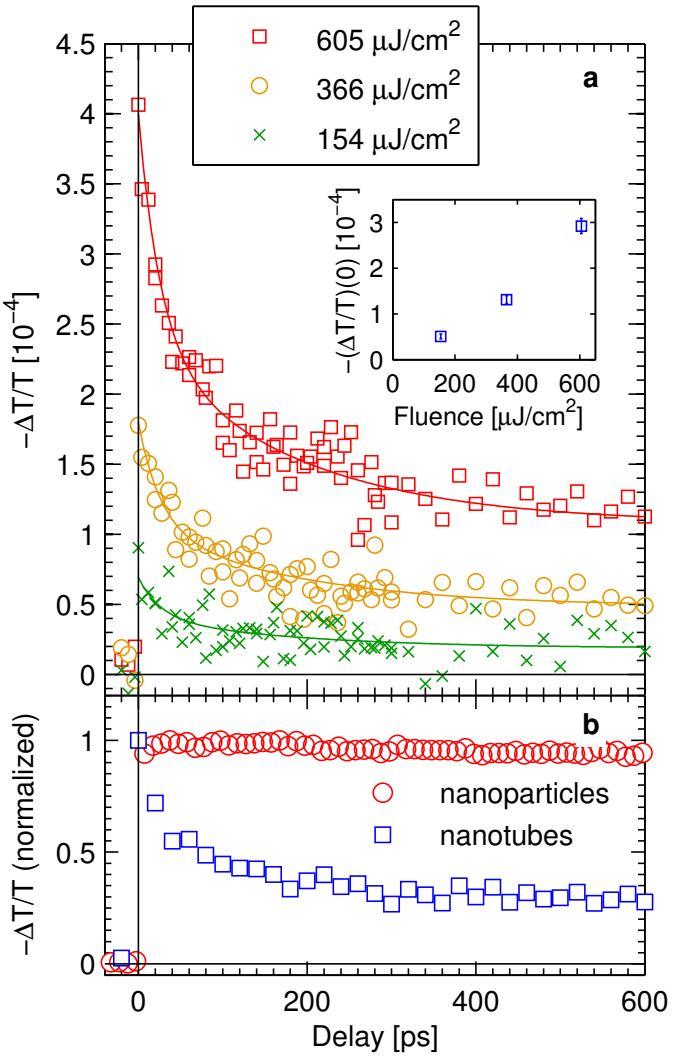

Figure 4.5: THz transmission transients (545 nm excitation, in vacuum) **(a)** of dye-sensitized TiO_2 nanotubes ($T_{ano} = 5$ °C) for different excitation fluences. Inset: Amplitude of the initial THz response and the long-lived (constant) contribution vs. excitation fluence as extracted from fits (see text); **(b)** of dye-sensitized TiO_2 nanotubes (as in (a), highest fluence) in comparison to dye-sensitized, sintered TiO_2 nanoparticles (20 nm, Dyesol).

curves closely resembles the undyed case with the one very notable difference that the conductivity does not fully decay to zero within the experimentally accessible time range of 1.2 ns, but rather levels off to a constant value, i.e. a very long-lived contribution remains. A similar behaviour has also been observed in sintered nanoparticles [53]. Here, data on dyed TiO_2 nanoparticles was taken as well to serve as a reference measurement and is shown in Figure 4.5(b). An almost complete elimination of early time decay of the free-electron population is observed.

The influence of dye-sensitization may be explained as follows: From photovoltage decay measurements it is known that recombination lifetimes of injected electrons with the oxidized dye are on the order of milliseconds or even seconds [34, 47]. As the excitation pulse repetition rate is 1.1 kHz, i.e. the time between subsequent pump-probe cycles is shorter these lifetimes, it can be expected that deep interband trap states which usually mediate recombination processes are gradually filled by injected electrons and hence passivated [32]. Consequently an equilibrium between trapping and detrapping of electrons in shallow trap states is reached on a nanosecond timescale with a certain fraction of the initially excited carriers in the conduction band. Figure 4.6 gives a simplified illustration of the charge generation, injection and recombination processes for the dye-sensitized and the undyed case as proposed and modelled here. In the case of nanoparticles, where the concentration of shallow traps was concluded to be significantly lower than in nanotubes, it appears to be possible that even these states are entirely passivated.

A rough comparison of conductivity decay in dyed and undyed samples (Figures 4.5 and 4.2) suggests similar to slightly higher trapping lifetimes in both systems and the same excitation-density independent behaviour. Sensible fitting of the data for the dyed case is difficult, since there might be injection dynamics on the ps-timescale superposing carrier decay processes [53]. However, in order to verify mono-molecular decay behaviour and to come to at least a rough estimation of the fast decay life-

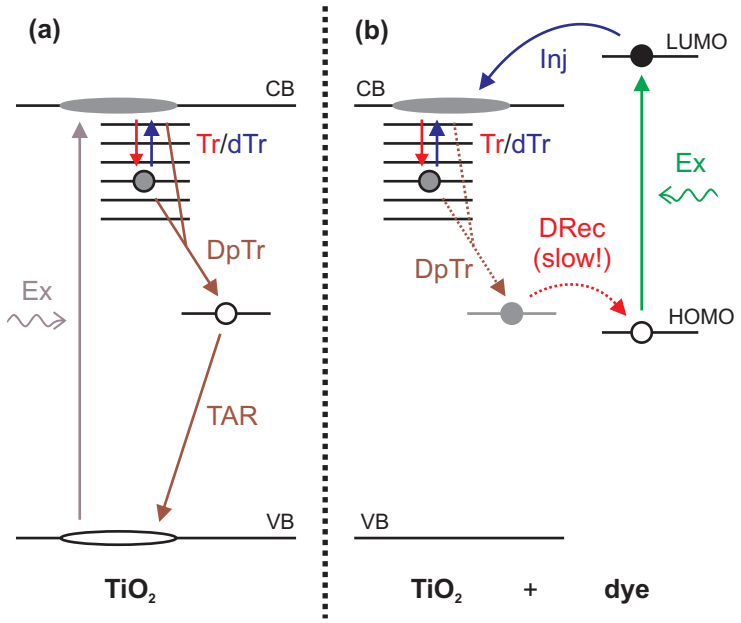

Figure 4.6: Illustration of processes within the applied model for charge-carrier dynamics in **(a)** undyed and **(b)** dye-sensitized TiO_2 nanotubes. Possible hole trapping processes are neglected here. The deep trap state in (b) is greyed out to depict that this state is almost permanently filled due to the recombination process with the oxidized dye (DRec) being much slower than the trapping process (DpTr). The corresponding recombination path is therefore very slow overall as indicated by the dotted arrows. See text for details. Closed circles/ellipses: electrons, Open circles/ellipses: holes/normally unoccupied electron traps. Acronyms: CB: conduction band, DpTr: deep trapping, DRec: recombination with oxidized dye, dTr: (shallow) detrapping, Ex: (optical) excitation, HOMO: highest occupied molecular orbital, Inj: injection, LUMO: lowest unoccupied molecular orbital, TAR: trap-assisted recombination, Tr: (shallow) trapping, VB: valence band.

time, bi-exponential fits according to Equation 4.1 were again applied - here with an additional constant contribution reflecting the long-lived electron population after saturation of all available deep trap states. All lifetimes and the relative magnitude of the long-lived component are shared among all transients for the different excitation fluences and globally optimized.

For the initial fast decay component (first term in Equation 4.2) a time constant of 26 ps is obtained in comparison to 14 ps for undyed samples. The similarity of trapping times under direct excitation and after electron injection is worth noting as it suggests that shallow trap states occur homogeneously distributed throughout the bulk of TiO_2 nanotubes rather than predominantly at the surface. For this argument, the plausible assumption is made that direct interband excitation results in a homogeneous photoexcited carrier density over the cross-section of the tubes, whereas electrons injected from an attached dye would mainly be found close to the surfaces. Consequently, if shallow trap states were also predominantly located at the tube surfaces, reduced lifetimes would be expected for injected electrons in dye-sensitized samples. Here, on the contrary, slightly longer lifetimes are determined, which may be the result of a weakly passivating effect of dye-attachment or simply reflecting a superposition of population decay with a finite injection-related rise time component.

4.2.4 Estimation of THz Electron Mobilities

Early-time THz-mobilities of free electrons in TiO_2 nanotubes can be estimated from the data acquired in this chapter. Before proceeding to the results, two important potential sources of systematic error have to be remarked, which cause an underestimation of the absolute mobility value of nanostructured TiO_2 from the photoinduced THz transmission change. Firstly, the calculation of carrier mobilities from photoconductivity data requires an assumption on the efficiency of incident photon-to-free carrier conversion as detailed in Section 3.1.2. It was discussed in conjunction with

the results on the influence of ambient air, which has been shown to cause a drop in the initial THz response, that several possible processes may potentially reduce the conversion ratio ϕ. These include ultrafast immobilization processes, immediate formation of excitonic states [133] or non-intraband absorption. In the case of dye-sensitized nanotubes, the injection efficiency affects the value of ϕ as well. Hence the values reported here, namely the effective mobilities $\phi\mu$ represent a lower limits to the actual carrier mobility.

Secondly, since the relative permittivity of TiO_2 is high (bulk anatase THz permittivity: $\epsilon_{\mathrm{bulk}} \approx 30$ [134, 135]) and the characteristic structure size is well below the THz wavelength, the bulk of the structure is partly screened from the electric field of the THz wave. This issue has been identified before by *Hendry et al.* [52] and while the authors employ Maxwell-Garnett effective medium theory to account for electric field screening, here a numerical calculation is performed to estimate the strength of this effect. Figure 4.7 shows the 2D-electric field distribution in a cross-section of a TiO_2-nanotube array as obtained by numerically integrating Maxwell's equations under the boundary conditions of a given potential difference from north to south. Periodic boundary conditions are applied at the east- and west-ends of the matrix. The results of these calculations show that the extent to which screening reduces the strength of the electric field inside the material is highly dependent on the gap between the tubes. This makes it difficult to obtain a reliable correction factor, as the width of these gaps is hard to determine and not constant along the length of the tubes due to the ripples in the walls observed under the SEM.

Electron mobilities are calculated using Equation 3.4. Evaluating several measurements on dye-sensitized samples of all available wall thicknesses, values between $\phi\mu_{\mathrm{n}} = 0.07\,\mathrm{cm}^2/(\mathrm{Vs})$ are obtained for the sample anodized at $T_{\mathrm{Ano}} = 55\,^{\circ}\mathrm{C}$ (thinnest walls) and $\phi\mu_{\mathrm{n}} = 0.2\,\mathrm{cm}^2/(\mathrm{Vs})$ for the sample anodized at $T_{\mathrm{Ano}} = 5\,^{\circ}\mathrm{C}$ (thickest walls). For undyed samples the resulting values are: $\phi\mu_{\mathrm{n}} + \phi\mu_{\mathrm{p}} = 0.1\,\mathrm{cm}^2/(\mathrm{Vs})$ for

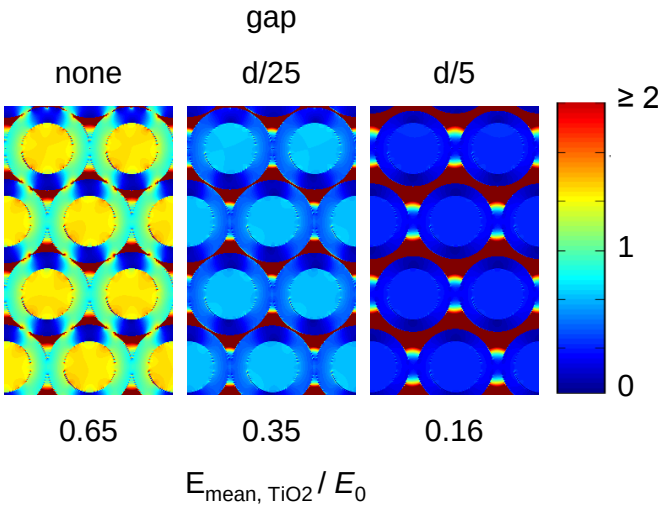

Figure 4.7: Simulated distribution of the electric-field amplitude in a 2D-cross-section of TiO_2-nanotubes ($\epsilon_r = 30$) surrounded by vacuum ($\epsilon_r = 1$) for three different sizes of the gap x between neighbouring tubes with respect to their diameter d ($x = 0$, $x = d/25$ and $x = d/5$). Below the colormap plots, the averaged value of the electric field amplitude within the nanotubes normalized to the average electric field across the matrix is stated.

$T_{\mathrm{Ano}} = 55\,^{\circ}\mathrm{C}$ and $\phi\mu_{\mathrm{n}} + \phi\mu_{\mathrm{p}} = 0.4\,\mathrm{cm}^2/(\mathrm{Vs})$ for $T_{\mathrm{Ano}} = 5\,^{\circ}\mathrm{C}$. The discrepancy between the results for dye-sensitized and undyed samples may go back to less-than-unity injection efficiencies, the precise value of which is unknown and can hence not be factored into the mobility calculation. When accounting for electric field screening based on the performed simulation, the stated values increase by a factor of 1.5 or more depending on the size of the gap between the tube walls. This effect may also be a cause for the variation of the as-measured mobility with anodization temperature consistent with the observation of greater spaces between tubes at higher temperatures [61].

With regards to the charge extraction performance of TiO_2-nanotubes in dye-sensitized solar cells this study provides two main results. Firstly it is noted that the THz electron mobilities on TiO_2 nanotubes determined here are similar to those found for sintered TiO_2 nanoparticles ($\phi\mu_{\mathrm{NP}} \approx 0.1\,\mathrm{cm}^2/(\mathrm{Vs})$ [53]). Hence electron motion on very short time- and lengthscales ought to be similarly fast in both materials. Secondly however this study revealed an order of magnitude faster trapping of

electrons in shallow traps as a transport-limiting phenomenon. The fraction of electrons immobilized in photovoltaic devices at any one time can be predicted from the shallow trapping and detrapping rates k_{tr} and k_{dtr}. Considering that deep intraband trap states are expected to be filled under steady state illumination conditions and hence $k_{\mathrm{deep}} \approx 0$ (see sketch in Figure 4.6), the equilibrium between shallow trapping and detrapping is reached at $n_{\mathrm{tr}}/n_{\mathrm{fr}} = k_{\mathrm{tr}}/k_{\mathrm{dtr}}$ following Equation 4.1. A fraction of immobilized electrons of $n_{\mathrm{tr}}/(n_{\mathrm{fr}} + n_{\mathrm{tr}}) \approx 63\,\%$ is obtained using the values extracted from the data on undyed nanotubes in Figure 4.2. This is consistent with the observation of a long-lived free electron population in actual dye-sensitized tubes, which is found to consist of about 36 % of the initially injected density. In dye-sensitized nanoparticles on the other hand, a near-complete saturation of trap states is observed. The circumstance that only about a third of the injected electrons are available as free carriers in TiO_2-nanotubes reduces the long-range mobility in the material accordingly. Moreover it is noted that trapping events act as a scattering process, which further slows down diffusion. Hence, overall the observed much fast electron trapping provides a plausible explanation for why TiO_2-nanotubes so far failed to outperform sintered nanoparticles in terms of charge collection times despite the existence of more direct percolation paths.

4.2.5 THz Conductivity Spectra of TiO_2 Nanotubes

Photoinduced THz conductivity spectra were taken on dyed and undyed TiO_2 nanotubes at early and at later time after excitation with respect to the timescale of the fast trapping process. The results are shown in Figure 4.8. Undyed TiO_2 nanotubes show a predominantly flat response with a negligible imaginary part. Note that the slight drop-off towards low frequency can be attributed to an artefact arising from the diffraction limited THz beam waist approaching the size of the optical pump beam spot. The spectrum is otherwise compatible with drude-like transport at frequencies below the characteristic relaxation rate ($f \ll 1/\tau$) [100]. This stands in contrast

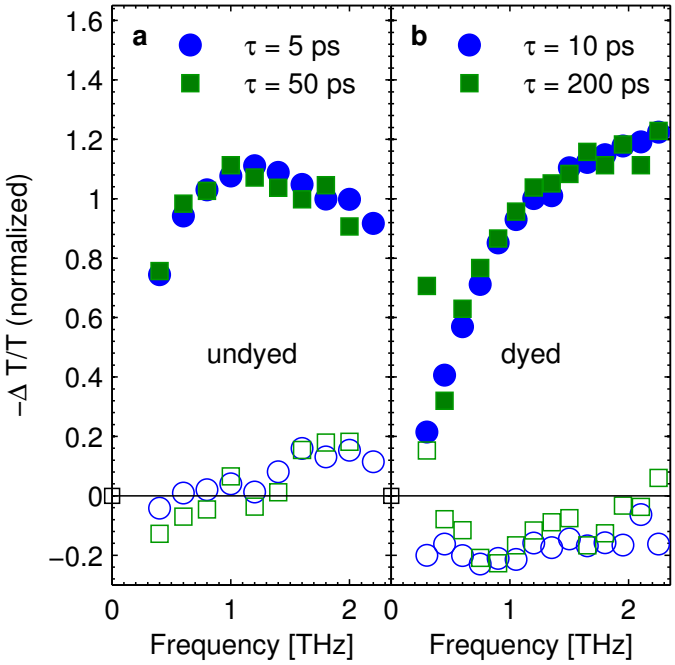

Figure 4.8: THz conductivity spectra (closed symbols: real part, open symbols: imaginary part). **a**: undyed TiO_2 nanotubes, at early time (5 ps) and at 50 ps after excitation at 266 nm (Fluence: 125 $\mu J/cm^2$). **b**: dyed TiO_2 nanotubes, at early time (10 ps) and at 200 ps after excitation at 545 nm (Fluence: 680 $\mu J/cm^2$). All spectra taken in vacuum ($p \approx 2 \cdot 10^{-2}$ mbar). A 450 µm GaP wafer has been used for THz generation in these measurements.

to the THz photoconductivity spectra of TiO_2 nanoparticles [52, 53], which exhibit clear localization effects [136, 137]. The different behaviour may be attributed to the slightly larger 'free path' for the electron in the cross-section of the nanotubular structure (diameter ∼50 nm) than in the one of the nanoparticle matrix (diameter ∼20 nm), particularly given that the probing electric field primarily penetrates the section of the tube walls tangential to the direction of the field vector as shown in Figure 4.7.

Dye-sensitized nanotubes on the other hand show a very similar THz-conductivity spectrum to nanoparticles, indicating significant localization effects as expressed in the strong decrease of conductivity towards low frequencies and the negative imaginary part leading to a 'capacitive' behaviour. A reason for the altered spectral response may lie in the spatial distribution of carriers which is spread out through the bulk for the case of direct excitation in undyed TiO_2 and concentrated at the surfaces for the case of electron injection from a dye. Coulombic interactions with the negatively charged, oxidized dye may strengthen this effect. Other possible explanations may be based on the presence of a (trapped) electron population which has built up over many injection cycles due to the slow back-transfer to the oxidized dye altering the shape of the electric potential within the tubes.

Previously, Richter et al. [133] have reported a resonant feature in the spectra of TiO_2 nanotubes at about 1.8 THz, which is ascribed to an exciton-like state. The authors argue this state acts as a trap which limits carrier mobility. Such a resonance was not observed in any of the samples here; however it has to be noted that the growth conditions and the resulting tube dimensions differ significantly between the said study and this work. Richter et al. studied about 30 times longer tubes with an about three times larger diameter, which resulted from at least 25 times longer anodization time. Given that the excitonic state was linked to an increased concentration of trap states arising from fluorine and titanium impurities, which are introduced during the

growth process, the absence of this state in the samples used here can be plausibly explained.

4.3 Conclusion

In conclusion, the decay dynamics of directly excited and of injected free electrons in TiO_2 nanotubes were studied by means of optical-pump-terahertz-probe spectroscopy. The results may be described within a simple model of shallow trapping, detrapping from shallow traps, and irreversible immobilization in deep traps. Interestingly shallow trapping lifetimes are found to be as short as 20-50 ps and thereby making the decay process at least an order of magnitude faster than in sintered TiO_2 nanoparticles. This provides a possible explanation for why the charge-collection performance of TiO_2 nanotubes in dye-sensitized solar cells does not seem to surpass that of TiO_2-nanoparticles despite their more direct electron percolation paths. A comparison of nanotube samples, which were anodized at different temperatures and therefore have different wall thicknesses, showed no significant influence of this parameter on carrier lifetimes. Similarly fast trapping dynamics were observed upon direct interband excitation of the material and upon injection from an attached dye. These results suggest that there is no predominantly high concentration of shallow traps at the surface of the tubes. Under sufficiently strong electron injection it is revealed that while dye-sensitized nanoparticles exhibit almost complete elimination of carrier decay on the nanosecond timescale due to trap-filling, no saturation effects are observed for shallow traps in nanotubes. Effective early time carrier mobilities were found to be similar in both materials with values on the order of $0.1\,\mathrm{cm}^2/(\mathrm{Vs})$. It is noted that due to electric field screening effects, this value represents a lower limit with the actual electron mobilities expected to be higher by at least a factor 1.5. In view of device applications the results from this chapter suggest that potential improvements to the charge transport performance of TiO_2 nanotubes may be achieved, if modifi-

cations to the anodization process can be identified which reduce the concentration of incorporated trap states.

5

Charge Transport and Recombination in Meso-Superstructured Organo-Lead Halide Perovskites

Given the rapid rise in performance of lead-halide perovskite photovoltaic devices, little is known about what makes these materials so successful at generating and transporting photocurrents. Some work on transport properties has been published on the related tin halides [138, 139] and recently Hall-effect conductivity measurements have been performed on $CH_3NH_3PbI_3$ [82]. Other studies on lead halides mostly focused on optical and excitonic properties [69, 79, 140, 141] or theoretical band structure calculations [75, 76, 77, 78]. It has recently been shown that charge carriers are capable of travelling over distances of up to a micron in some perovskite absorbers, which exceeds their typical absorption depth [87]. However, the mechanism causing such an extended diffusion range remains mysterious, given that long charge-carrier diffusion distances require both low recombination rates and/or high charge mobility. Satisfying both requirements simultaneously is generally difficult given the fundamental proportionality relation between them established by the Langevin model for kinetic recombination, which typically applies for conductors with charge mobilities below the order of 1-10 $\mathrm{cm}^2/(\mathrm{Vs})$ [142, 143].

In this chapter, it is shown that both $CH_3NH_3PbI_3$ and $CH_3NH_3PbI_{3-x}Cl_x$ exhibit unexpectedly long charge-carrier diffusion lengths because of non-Langevin charge-carrier recombination. Using ultrafast optical-pump-THz-probe spectroscopy, unusually low bi-molecular recombination rates are determined in these materials, falling at least four orders of magnitude short of the Langevin prediction. Lower bounds for the high-frequency charge mobility are established of $11.6\,cm^2/(Vs)$ for $CH_3NH_3PbI_{3-x}Cl_x$ and $8\,cm^2/(Vs)$ for $CH_3NH_3PbI_3$, which are remarkably high for solution-processed materials. The combination of high charge mobility and low bi-molecular recombination leads to carrier diffusion lengths that exceed one micron and are significantly longer for the mixed halide system. It is proposed that such reduced bi-molecular charge recombination arises from spatial separation of electrons and holes in the system, which may be tuned through substitutions affecting the electronic structure of the metal-halide system.

In order to highlight the relevance of this spectroscopic study to solar cell operation, the spectroscopic findings of this chapter are correlated with the performance of matching devices. Figure 2.5(c) shows a schematic of the device structure employed: the metal-halide perovskite acts as both, light absorber and charge transporter while spiro-OMeTAD functions as the hole transporter. The organo-lead halide perovskite is infiltrated into a 400 nm-thick scaffold layer of Al_2O_3 nanoparticles whose main function is to improve uniformity of coating, inhibiting pin-hole formation and the associated dark current leakage [72, 74]. Here, this device is termed a meso-superstructured solar cell (MSSC); however, it is important to note that electrons and holes have to travel through the perovskite layer to reach the respective extraction layers, compact TiO_2 and spiro-OMeTAD, in analogy to a planar-heterojunction device structure. For spectroscopic measurements, metal-halide perovskite films were deposited under identical conditions on z-cut quartz, but with the electrodes and spiro-OMeTAD layers omitted.

The mixed halide perovskite $CH_3NH_3PbI_{3-x}Cl_x$ was synthesized as described in [14] and [72] with excess methylammonium which may compensate losses of the organic material during the annealing process. The triiodide halide perovskite $CH_3NH_3PbI_3$ reported in [13] and [73] on the other hand was synthesized at a 1:1 molar ratio of CH_3NH_3I to PbI_2. For best comparability, two kinds of $CH_3NH_3PbI_3$ materials were prepared the non-stoichiometric type with excess methylammonium (3:1) and the stoichiometric type (1:1). Spectroscopy samples and devices were made using the same stock of perovskite precursor. Full details are given in the following section. All samples and devices were prepared by *Giles E. Eperon.*

5.1 Experimental Details

5.1.1 Material Synthesis

$CH_3NH_3PbI_{3-x}Cl_x$ precursor: Methylammonium iodide (MAI) was prepared by reacting methylamine, 33 wt% in ethanol (Sigma-Aldrich), with hydroiodic acid (HI) 57 wt% in water (Sigma-Aldrich), at room temperature. HI was added dropwise while stirring. Upon drying at 100 °C, a white powder was formed, which was dried overnight in an open dish on a hotplate before use. To form the non-stoichiometric $CH_3NH_3PbI_{3-x}Cl_x$ precursor solution, methylammonium iodide and lead (II) chloride (Sigma-Aldrich) are dissolved in anhydrous N,N-Dimethylformamide (DMF), at a 3:1 molar ratio of MAI to $PbCl_2$, with final concentrations 0.88 M lead chloride and 2.64 M methylammonium iodide. This solution is stored under a dry nitrogen atmosphere.

Stoichiometric precursor: MAI was dissolved in a 1:1 molar ratio with lead (II) iodide (Sigma-Aldrich) in DMF, with final concentrations 0.88 M.

Non-stoichiometric precursor: MAI was dissolved in a 3:1 molar ratio with lead (II) iodide (Sigma-Aldrich) in DMF, with final concentrations 0.88 M lead iodide and 2.64 M MAI.

Device substrates: Devices were fabricated on fluorine-doped tin oxide (FTO) coated glass (Pilkington TEC7, 7 Ω/sq). Initially FTO was removed from regions under the anode contact, to prevent shunting upon contact with measurement pins, by etching the FTO with 2 M HCl and zinc powder. Substrates were then cleaned sequentially in 2 % hallmanex detergent, acetone, propan-2-ol and oxygen plasma. A hole-blocking layer of compact TiO_2 was deposited by spin-coating a mildly acidic solution of titanium isopropoxide in ethanol, and annealed at 500 °C for 30 min.

5.1.2 Sample Preparation

Perovskite solar cells: A colloidal dispersion of <50 nm Al_2O_3 nanoparticles in isopropanol was spin-coated on the substrates followed by drying at 150 °C. Then, to form the perovskite layer, the perovskite precursor solution was deposited and spin-coated at 2000 rpm. Films were then annealed at 100 °C for 10 min (stoichiometric $CH_3NH_3PbI_3$), 150 °C for 15 min (non-stoichiometic $CH_3NH_3PbI_3$), or 100 °C for 45 min ($CH_3NH_3PbI_{3-x}Cl_x$). A hole-transporting layer was then deposited in air by spin-coating at 2000 rpm a 0.79 M solution in chlorobenzene of 2,2',7,7'-tetrakis-(N,N-di-p-methoxyphenylamine)9,9'-spirobifluorene (spiro-OMeTAD), with additives of lithium bis(trifluoromethanesulfonyl)imide and 4-tert-butylpyridine [144]. Devices were then left overnight in air for the spiro-OMeTAD to dope via oxidation. Finally, 60 nm gold electrodes were thermally evaporated under vacuum of $\sim 10^{-6}$ mbar, at a rate of ~ 0.1 nm/s, to complete the devices.

Samples for THz and PL experiments: Samples for THz and PL measurements consist of a layer of perovskite infiltrating a film of 500 nm mesoporous Al_2O_3. This layer was deposited by spin coating on 2 mm thick z-cut quartz in the same way as described above for the active layer of the solar cells.

5.1.3 Solar Cell Characterization

The current density-voltage (J-V) curves were measured (2400 Series SourceMeter, Keithley Instruments) under simulated AM 1.5 simulated sunlight at 100 mW/cm^2 irradiance generated by an Abet Class AAB sun 2000 simulator, with the intensity calibrated with an NREL calibrated KG5 filtered Si reference cell. The mismatch factor was calculated to be less than 1 %. The solar cells were masked with a metal aperture to define the active area, typically 0.09 cm^2 and measured in a light-tight sample holder to minimize any edge effects and ensure that the reference cell and test cell are located in the same spot under the solar simulator during measurements.

5.1.4 THz Time-Domain Spectroscopy

The optical-pump-THz-probe setup (described in detail in section 3.1) uses a Ti:Sapphire regenerative amplifier to generate 40 fs pulses at 800 nm wavelength and a repetition rate of 1.1 kHz. Terahertz pulses are generated by optical rectification in 450 µm thick (110)-GaP and detected by electrooptic sampling in ZnTe crystal (0.2 mm (110)-ZnTe on 3 mm (101)-ZnTe). Pulses for optical excitation of the samples at a wavelength of 550 nm have been generated using an optical parametric amplifier (OPA). Optical excitation was carried out through the substrate side of the sample. The diameters of pump and probe beam at the sample position are 2.6 mm and 1.5 mm (FWHM). Measurements have been performed with the entire THz beam path (including emitter, detector and sample) in an evacuated chamber at pressure $p < 10^{-1}$ mbar.

5.1.5 Photoluminescence Spectroscopy

The experimental PL setup based on a pulsed didode laser and described in Section 3.2.4 is used as it provides sufficiently low repetition rates required for the measurement of long mono-molecular decay lifetimes (see 5.2.3). The excitation wave-

length for all acquisitions is 510 nm and the repetition rate was chosen as 1 MHz. Counting rates were kept below 1 % of the repetition rate to avoid multi-photon events. All PL measurements were performed with the sample under vacuum ($p < 10^{-5}$ mbar).

5.2 Results and Discussion

5.2.1 Device Performance

Figure 5.1(a) displays typical current-density-voltage-characteristics of solar cells incorporating the three different lead-halide perovskites. Maximum power conversion efficiencies (PCE) recorded under simulated sunlight (AM1.5) were 12.7 % for the mixed halide, 8.5 % for the non-stoichiometric (3:1) triiodide, and below 1 % for the stoichiometric (1:1) triiodide lead perovskite. Table 5.1 lists detailed statistics. Minimum, maximum and average values for power conversion efficiency (PCE), short circuit current density (j_{SC}), open circuit voltage (V_{OC}) and fill factor (FF) for all batches are summarized in the table. The low performance of devices incorporating $CH_3NH_3PbI_3$ (1:1) may in part be attributed to poor film formation as evidenced by the large amount of scattering seen in the corresponding UV/vis absorption spectrum (Figure 5.1(b)).

5.2.2 THz Charge-Carrier Dynamics

In the next step, THz spectroscopy is used to unravel the charge dynamics in the perovskite materials following pulsed photoexcitation. It is still unclear to what extent primary photoexcited species in lead-halide perovskites at room temperature divide into free charges or exciton populations. Exciton binding energies of between 37 meV [90] and 50 meV [141] have been proposed for (orthorhombic) $CH_3NH_3PbI_3$ at low temperature (5 K). * In both studies the diamagnetic shift of the magnetoabsoption

*After the conclusion of the analysis for this chapter, further reports of exciton binding energies were published [89, 91]. See Section 2.2.1 for details.

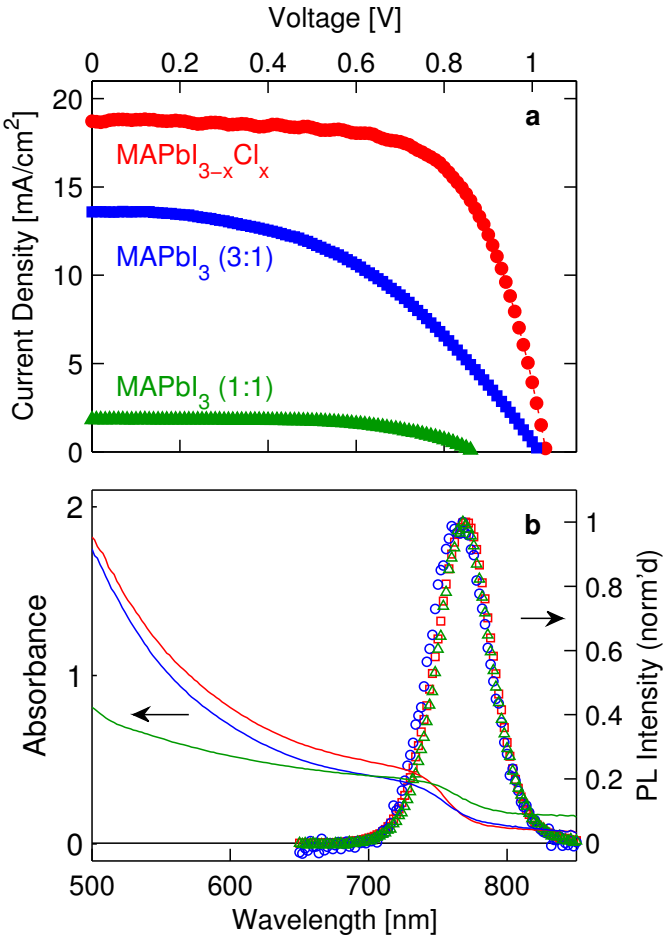

Figure 5.1: **(a)** Current density-voltage characteristics of photovoltaic devices employing triiodide ($CH_3NH_3PbI_3$) and mixed halide ($CH_3NH_3PbI_{3-x}Cl_x$) lead perovskite absorbers, recorded under 1.5 AM simulated sunlight. Full device performance statistics are given in Table 5.1 [Data kindly provided by *Giles E. Eperon*]. **(b)** Absorbance spectra of thin films of $CH_3NH_3PbI_{3-x}Cl_x$ (red line) $CH_3NH_3PbI_3$ (3:1) (blue line) and $CH_3NH_3PbI_3$ (1:1) (green line) together with photoluminescence spectra collected following excitation at 510 nm ($CH_3NH_3PbI_{3-x}Cl_x$ (red squares) $CH_3NH_3PbI_3$ (3:1) (blue circles) and CH_3NH_3-PbI_3 (1:1) (green triangles)).

Absorber Material		j_{SC} [mA/cm^2]	V_{OC} [V]	FF []	η [%]
	min	4.9	0.67	0.57	2.6
$CH_3NH_3PbI_{3-x}Cl_x$	max	18.9	1.05	0.68	12.7
	avg	12.6	0.98	0.64	8.0
	min	3.9	0.92	0.46	2.3
$CH_3NH_3PbI_3$ (3:1)	max	13.6	1.04	0.74	8.5
	avg	10.0	0.99	0.60	6.7
	min	0.5	0.79	0.34	0.2
$CH_3NH_3PbI_3$ (1:1)	max	1.9	0.91	0.72	0.9
	avg	1.1	0.86	0.56	0.5

Table 5.1: Device performance statistics for solar cell batches fabricated with the mixed and triiodide halide perovskites as absorbers on mesoporous Al_2O_3 scaffolds, fabricated as described in the main manuscript. The numbers of devices tested were: 44 ($CH_3NH_3PbI_{3-x}Cl_x$), 37 ($CH_3NH_3PbI_3$ (3:1)) and 26 ($CH_3NH_3PbI_3$ (1:1)). [Data kindly provided by *Giles E. Eperon*]

spectrum was measured to magnetic fields in excess of 40 T and the exciton binding energy was derived making assumptions about the value of the high frequency dielectric function [90]. Here, it is found that emission spectra and absorption onsets (Figure 5.1(c)) for all three investigated metal-halide perovskites are very similar, therefore any variation in exciton binding energy is likely to be relatively small. The proposed exciton binding energies of 37-50 meV are comparable to thermal energies at room temperature $k_BT \approx 26$ meV. Following photoexcitation, both free charge carriers and excitons may therefore be present, with their populations interchanging dynamically over the course of their lifetime.

Figure 5.2 displays the transient THz transmission dynamics following photoexcitation of $CH_3NH_3PbI_{3-x}Cl_x$ and $CH_3NH_3PbI_3$ for a range of different excitation fluences. In these experiments, the sample is excited by an optical light pulse at a wavelength of 550 nm and subsequently probed by a terahertz-frequency pulse after a well defined delay (see Section 3.1 for details of the apparatus). In the presence of free charges, the measured relative change in THz electric field transmission is proportional to the photoinduced conductivity in the material (see Section 3.1.2). In principle, any

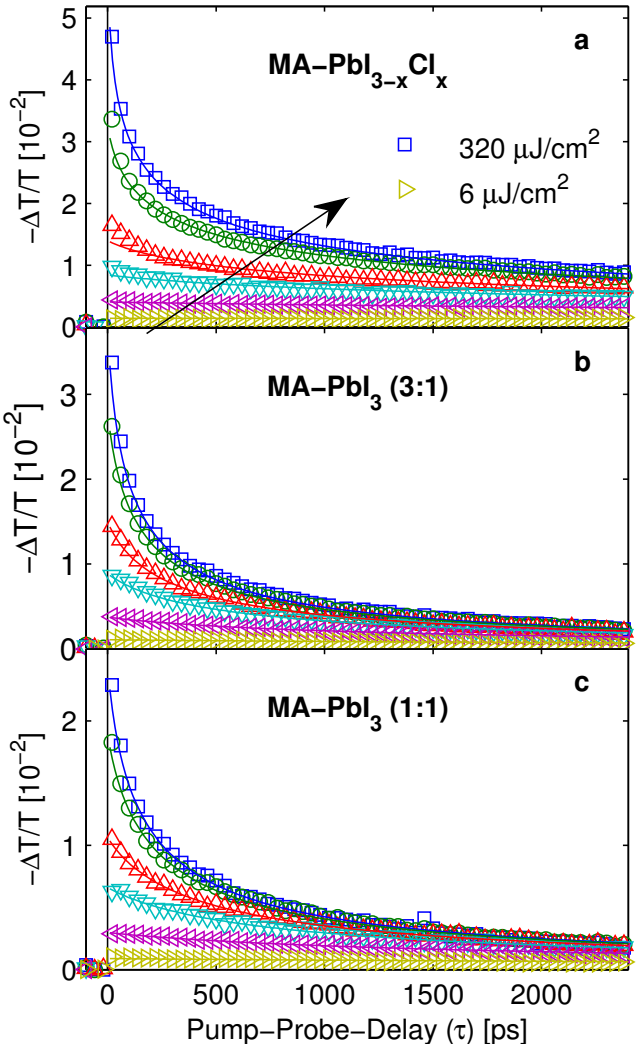

Figure 5.2: THz photoinduced absorption transient of **(a)** $CH_3NH_3PbI_{3-x}Cl_x$, **(b)** $CH_3NH_3PbI_3$ (3:1), and **(c)** $CH_3NH_3PbI_3$ (1:1) after excitation at 500 nm for fluences between 6 µJ/cm^2 and 320 µJ/cm^2. Solid lines are fits based on second- and third-order charge recombination as described in the text.

photoexcited species coupling to electro-magnetic THz radiation may be responsible for the observed THz transmission transients. Here it is argued that the observed dynamics arise solely from the photoconductivity of free charges. First, for an assumed exciton binding energy of ∼40 meV, the energy of probe photons employed here (1 THz corresponds to 4 meV) is too low to couple to significant intra-excitonic resonances. Second, the shape of the transient THz spectra (see Section 5.2.5) is incompatible with an excitonic absorption and more akin to those reported to describe charge motion in polycrystalline materials [100]. Third, it is shown below that the shape of the fluence-dependent transients is incompatible with a significant mono-molecular decay contribution from geminate recombination of excitons. It shall however be noted that a presence of excitons in the materials following photoexcitation is not ruled out; they simply do not appear to couple effectively to the THz probe.

Figure 5.2 reveals striking differences in the photoconductivity decay dynamics between the mixed halide and triiodide perovskites. Both $CH_3NH_3PbI_{3-x}Cl_x$ and $CH_3NH_3PbI_3$ show a fast initial decay component that becomes increasingly significant with increasing excitation fluence. However, for the triiodide perovskite, the fast component is much more pronounced at identical fluences. The lowest fluence employed (6 $\mu J/cm^2$) corresponds to an absorbed peak photon density of $\sim 6\times10^{17}\,cm^{-3}$. At elevated charge-carrier densities, higher-order effects such as bi-molecular (second order) and Auger (third order) charge recombination processes increasingly come into play. While bi-molecular recombination simply relies on an overlap of electron and hole wavefunctions, Auger processes involve energy and momentum transfer of the recombining electron-hole pair to a third charge carrier [145, 146].

To determine the charge recombination rates associated with both mono-molecular (arising e.g. from trap-assisted recombination) and higher-order processes, solutions

to the differential equation

$$\frac{\mathrm{d}n(t)}{\mathrm{d}t} = -k_3 n^3 - k_2 n^2 - k_1 n \ , \tag{5.1}$$

where n is the photoinduced charge-carrier density, are fitted to the transient THz photoconductivity data. The fitting of this model is based on the assumption that the photoconductivity decay is solely influenced by a change in charge-carrier density, rather than mobility, which is reasonable given the absence of visible photoconductivity decay in the low fluence regime over the observation window (Figure 5.2a).

For the correct scaling of the fit-results it has to be considered that the experimentally observed quantity is the photoinduced THz transmission change $x(t) \stackrel{\text{def}}{=} (\Delta T/T)(t)$, which relates linearly to the free carrier density (see Equation 3.1 and 3.3):

$$n(t) = \phi C x(t) \tag{5.2}$$

Here $C = \tilde{n}_0/x(0)$ is the proportionality factor between the immediate THz response $x(0)$ and the absorbed photon density

$$\tilde{n}_0 = \frac{E\lambda\,\alpha(\lambda)}{hcA_{\text{eff}}}(1 - R_{\text{pump}}), \tag{5.3}$$

which can be calculated from the pump beam parameters and the absorption coefficient of the sample α at the excitation wavelength λ. Due to the onset of nonlinear interactions, $x(0)$ does not remain proportional to $\tilde{n}_0$ at very high excitation fluences ($> 50\,\mu\text{J/cm}^2$). The dependence of the initial amplitude of the THz response on excitation fluence was evaluated and a significant effect of nonlinear processes was only observed at fluences beyond $60\,\mu\text{J/cm}^2$. The constant C is therefore determined based on data acquired in the weak excitation regime below this limit.

Substituting (5.2) into (5.1) yields

$$\begin{aligned} \frac{\mathrm{d}x}{\mathrm{d}t} &= -C^2\phi^2 k_3 x^3 - C\phi k_2 x^2 - k_1 x \\ &= -A_3 x^3 - A_2 x^2 - A_1 x \end{aligned} \tag{5.4}$$

with $A_i = C^{i-1}\phi^{i-1}k_i$. Numerical solutions to this equation are fitted simultaneously to all acquired THz transients of a fluence-dependent set (i.e. there is only one globally optimized value A_i for each rate constant, which is applied to all fluences).

A good reproduction of the data could be achieved even if the linear term was omited. Hence, fits are performed without the linear terms in order to determine the second- and third-order decay constants with high accuracy. By comparison to the full fits with the linear component inserted it is verified that neglecting the first order contribution was actually justified, and upper limits of values for k_1 of $(25\,\mathrm{ns})^{-1} = 4\times10^7\,\mathrm{s}^{-1}$ for $CH_3NH_3PbI_{3-x}Cl_x$ and $(6\,\mathrm{ns})^{-1} \approx 1.6\times10^8\,\mathrm{s}^{-1}$ for $CH_3NH_3PbI_3$ were established in agreement with visually flat curves observed for $CH_3NH_3PbI_{3-x}Cl_x$ in the low fluence regime over the 2.5 ns window.

As the photon-to-free-carrier conversion ratio ϕ is unknown, strictly speaking, only the values ϕ^2k_3, ϕk_2 (and k_1) can be deduced from the fits. These equal the actual decay rate constants k_3, k_2 (and k_1) in case the material exhibits full photon-to-free-charge conversion. All fit results are summarized in Table 5.2. To account for the spatially varying charge density profile, the fit routine takes into account the exponential charge density profile created by the pump beam by dividing the sample into 50 equally thick slabs and computing the decay function for all of these individually.

Two striking observations are made from the results of the fits. First, the monomolecular charge-carrier recombination rate is found to be exceptionally low in the investigated organo-lead halide perovksites. Such absence of trap- or impurity-assisted recombination over the timescale of nanoseconds is excellent news for use of these

materials in solar cells and is in contrast with other materials commonly used, such as GaAs [147] and mesoporous TiO2 [53]. Second, the bi-molecular charge recombination rate extracted for the mixed halide perovskite is an order of magnitude lower than for the triiodide materials. As shown below, this leads to markedly larger diffusion lengths even at elevated charge-carrier densities for the mixed halide making this material more suitable for planar-heterojunction devices.

Performance differences between the three organo-lead-halide perovskites could also potentially arise from discrepancies in the charge-carrier mobility μ. Such effects are elucidated by deriving the effective charge-carrier mobility for the three organo-lead-halide perovskites in the low-fluence regime. These values can be directly derived from the photoinduced change of THz electric field transmission $\Delta T/T$ using Equations 3.1 and 3.3. The effective charge-carrier mobility $\phi\mu$ is extracted from the photoconductivity onset value (prior to charge recombination) with knowledge of the absorbed photon density and optical parameters (see Section 3.1.2). Here, ϕ is the ratio of free charge-carrier density generated per photon density absorbed, which is unknown and may depend on factors such as the exciton binding energy. Excitation conditions are again ensured to be in the linear regime (fluence here: $6\,\mu J/cm^2$) to avoid systematic errors in the determination of the photoexcited carrier density due to multi-photon absorption processes.

Effective mobilities are determined of $11.6\,cm^2/(Vs)$ for $CH_3NH_3PbI_{3-x}Cl_x$ and $\sim 8\,cm^2/(Vs)$ for both $CH_3NH_3PbI_3$ variants. These values are exceptionally high for solution-processed materials, surpassing charge mobilities reported for mesoporous TiO_2 used in dye-sensitized solar cells by at least a factor of 20 [52, 53], and those of typical π-conjugated molecular semiconductors by several orders of magnitude [148, 149]. Note that effective charge-carrier mobility values represent lower bounds for the actual mobilities since the photon-to-charge branching ratio ϕ must fall between 0 and 1. Interestingly, *Stoumpos et al.* recently reported a DC dark electron

mobility of $\sim$66 $cm^2/(Vs)$ for unintentionally doped single crystalline bulk $CH_3NH_3PbI_3$ obtained from 4-probe resistivity and Hall-effect measurements [82]. Comparison with the values measured here suggests that, within the nanosecond diffusion range, the investigated solution-processed materials do not incur substantial charge-carrier mobility losses at grain boundaries. It shall be stressed that effective charge-carrier mobilities are relatively similar for the mixed and pure halide perovskite materials. Given that the emission spectra for the two types of materials suggest similar exciton binding energies, ϕ is likely to vary little, and hence the cause in the differences in planar-heterojunction PV performance is unlikely to arise from differences in charge-carrier mobility. It is therefore proposed that the improved performance of the mixed halide in perovskite MSSCs originates from lower charge recombination rates, rather than better charge mobility.

Table 5.2 summarizes the second- and third-order recombination constants and effective mobilities determined for the three lead-halide perovskite materials. From these values, the ratio, k_2/μ, of the bi-molecular recombination constant to the charge-carrier mobility may be computed and compared to the value expected from Langevin theory, $e(\epsilon_r\epsilon_0)^{-1}$, where e is the elementary charge and ϵ_r the appropriate value of the dielectric function [142, 143]. Remarkably, all three lead-halide perovskite materials exhibit recombination rates at least 4 orders of magnitude short of the theoretical value from the Langevin model (see Table 5.2). The Langevin model is based on a purely kinetic approach assuming that recombination will occur once an electron and a hole move within their joint capture radius, which is presumed to be larger than their mean free path [142, 143]. Materials in which the ratio of k_2/μ falls substantially short of the Langevin limit are naturally highly suitable for use in photovoltaics, allowing a low charge recombination rate without the penalty of lowered charge mobility. Note that charge recombination rates beyond the Langevin limit have been observed in other low-mobility materials that have been successfully incorporated in photovoltaic cells, such as solution-processed de-mixed blends of conjugated polymer

Material	Charge-Carrier Decay Constants			Mobility	Langevin	Device
CH_3NH_3...	3rd order $[cm^6s^{-1}]$	2nd order $[cm^3s^{-1}]$	1st o. (PL) $[\mu s^{-1}]$	$\phi\mu$ $[cm^2/(Vs)]$	$\frac{(k_2/\mu)_{ex}}{(k_2/\mu)_L}\,\epsilon_r^{-1}$	PCE_{max} [%]
...$PbI_{3-x}Cl_x$	9.9×10^{-29}	8.7×10^{-11}	4.9	11.6	4.2×10^{-6}	12.7
...PbI_3 (3:1)	3.7×10^{-29}	9.4×10^{-10}	15	8.1	6.4×10^{-5}	8.5
...PbI_3 (1:1)	1.3×10^{-28}	9.2×10^{-10}	14	8.2	6.2×10^{-5}	0.9

Table 5.2: Charge-carrier decay constants, Langevin ratio, charge mobility and device efficiencies for the investigated lead-halide perovskite materials listed in Column 1. Columns 2 and 3 show the third ($\phi^2 k_3$) and second (ϕk_2) order charge-carrier decay constants as determined from fits to the excitation-fluence dependence of the THz transient photoconductivity data (Figure 5.2). Column 4 gives mono-molecular recombination rates k_1 derived from mono-exponential fits to the tails of photoluminescence decay transients taken under low-fluence excitation (see Figure 5.3). Column 5 lists the effective charge-carrier mobilities $\phi\mu$ at THz frequencies taken from low-fluence THz transient photoconductivity traces (Figure 5.2). Since the branching ratio ϕ of generated free charge-carrier density per absorbed photon density is unknown, the second- and third order decay constants, k_2 and k_3 and the charge-carrier mobility μ can only be determined subject to multiplication with ϕ. Since $0 \leq \phi \leq 1$, values listed in Columns 2, 3, 4 represent lower limits of k_2, k_3 and μ. Column 6 compares the bi-molecular-recombination-rate-to-mobility ratio $(k_2/\mu)_{ex}$ (from Columns 3 and 5) to that expected from Langevin theory $(k_2/\mu)_L = e(\epsilon_r\epsilon_0)^{-1}$, multiplied by ϵ_r^{-1}. The possible range for ϵ_r is limited to the interval between the electric permitivities of its consituents: Vacuum ($\epsilon = 1$), Al_2O_3 ($\epsilon \approx 1.77$, [150]) and $CH_3NH_3PbI_3$ ($\epsilon \approx 6.5$, [90]). Column 7 lists maximum power conversion efficiency achieved with the material incorporated into full photovoltaic device structures.

with fullerene derivatives [148, 151] and amorphous silicon [152]. In the former, such effects have been attributed to electrons and holes being separated into two material components, while in the latter, spatial charge separation through a random potential landscape has been postulated. As further discussed later in this chapter, the metal-halide electronic structure may induce an intrinsic spatial charge separation that reduces recombination rates.

5.2.3 Time-Resolved Photoluminescence

To be able to assess the lifetimes of charge carriers at very low excitation densities, where bi-molecular processes become negligible, the value of the mono-molecular recombination rate has to be determined. As the THz photoconductivity study shows, a suitable experiment requires access to timescales of the nanosecond to microsecond range and sufficient sensitivity to work at very low carrier densities. For these reasons, time-resolved photoluminescence spectroscopy by means of time-correlated single photon counting (TCSPC) is chosen for this purpose (see 5.1.5). The dynamics observed with this technique may reflect a combination of both excitonic and free charge-carrier populations. However, given the relatively low estimates for the exciton binding energy in these systems, excitons and charges may coexist and are probably influenced by similar mono-molecular decay channels. In addition, in the low-fluence regime, exciton formation will most likely precede charge recombination. The determined mono-molecular rates therefore represent an upper limit to what free charge carriers will experience and provide a useful reference point. Note that both exciton geminate recombination, and trap-assisted recombination (if outside the saturation regime) may lead to the observed fluence-independent, mono-molecular PL decay components. While both channels may be either radiative, or non-radiative, they will decimate the exciton and/or charge population which will be reflected in the observed PL dynamics.

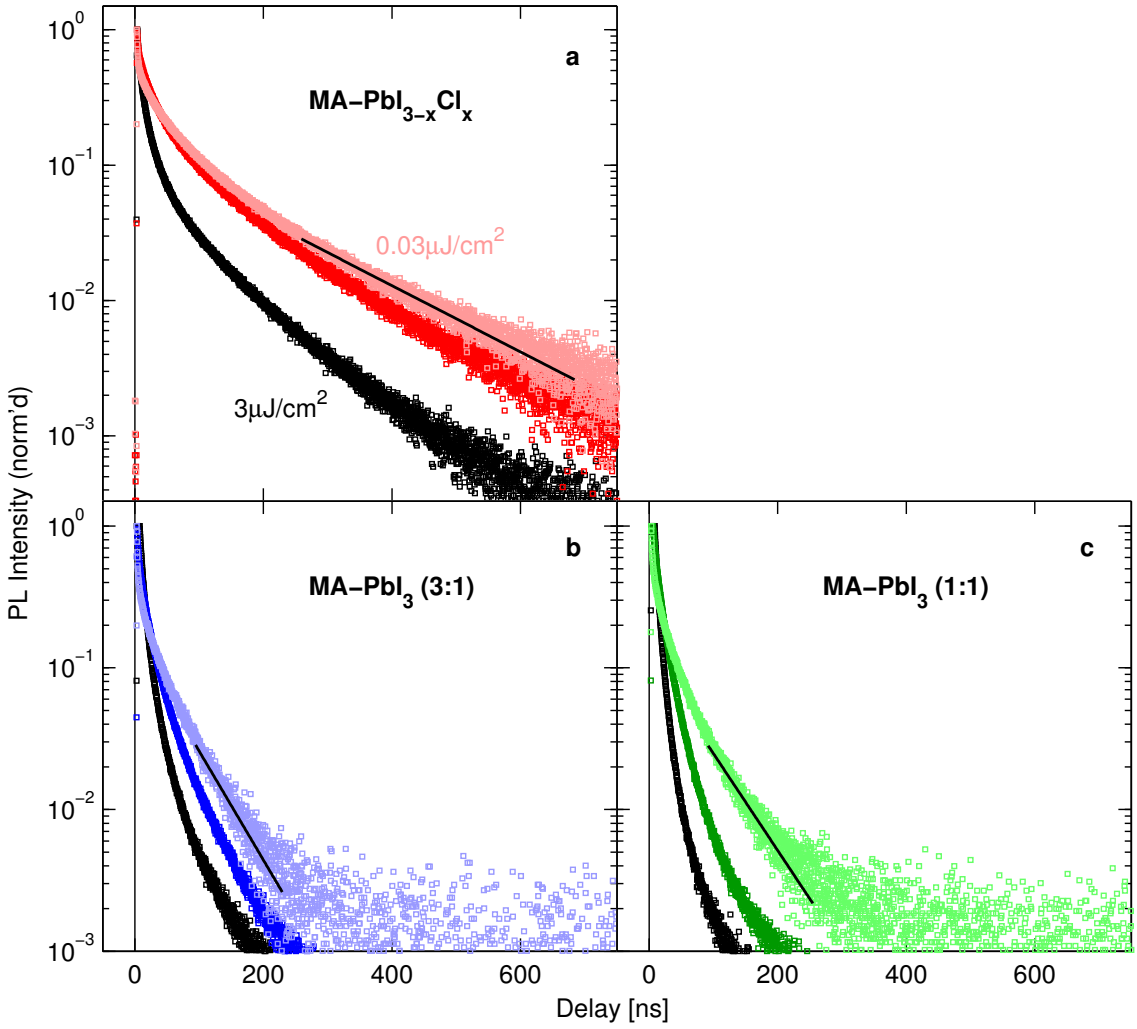

Figure 5.3: Time-resolved photoluminescence of $CH_3NH_3PbI_3$ and $CH_3NH_3PbI_{3-x}Cl_x$ for excitation fluences of 3 $\mu J/cm^2$, 0.3 $\mu J/cm^2$ and 0.03 $\mu J/cm^2$. (Excitation wavelength: 510 nm). A first order decay function was fitted to the tails of the lowest fluence data to extract an estimate of the mono-molecular decay rate.

Time resolved photoluminescence traces of $CH_3NH_3PbI_3$ and $CH_3NH_3PbI_{3-x}Cl_x$ were acquired for three fluences in the interval of $3\,\mu J/cm^2$ down to $0.03\,\mu J/cm^2$, which correspond to initial absorbed photon densities between $6 \times 10^{17}\,cm^{-3}$ and $6 \times 10^{15}\,cm^{-3}$. The data is displayed in Figure 5.3. Based on the rate constants determined by THz spectroscopy, bi-molecular recombination is expected to only contribute significantly at the highest fluence of this range, and for lower fluences at early times before the charge density has decayed significantly. However, for the 700-ns observation window, significant charge-carrier diffusion is expected to occur, which will complicate any analysis of the decay traces in terms of higher-order decay mechanisms. In order to extract a value for the mono-molecular decay constants, the attention is therefore directed towards the longer-delay, low fluence data which will be mainly dominated by first-order processes. Figure 5.3 shows that indeed at longer delays the decay approaches a mono-exponential shape reflecting the mono-molecular contribution; a small curvature however remains which introduces a systematic error of $\sim$10 % to the analysis. The mono-molecular rate constants are extracted from the tails of the lowest fluence PL data by performing a mono-exponential decay fit to an appropriate interval (i.e. as far from the initial steep decay as possible, but still sufficiently wide). The rate constants k_1 obtained from fits shown as solid lines in Figure 5.3 are: $CH_3NH_3PbI_{3-x}Cl_x$: $4.9 \times 10^6\,s^{-1}$, $CH_3NH_3PbI_3$ (3:1): $15 \times 10^6\,s^{-1}$ and $CH_3NH_3PbI_3$ (1:1): $14 \times 10^6\,s^{-1}$.

5.2.4 Charge-Carrier Diffusion Lengths

To illustrate their relative contributions to the overall charge decay rate (R_{total}), Figure 5.4(a,b) shows the first-, second- and third order electron-hole recombination rates as a function of charge-carrier density in the medium. The decay rates were computed from the rate constants summarized in Table 5.2 (k_1 as extracted from PL measurements, k_2 and k_3 as extracted from OPTP measurements) according to the

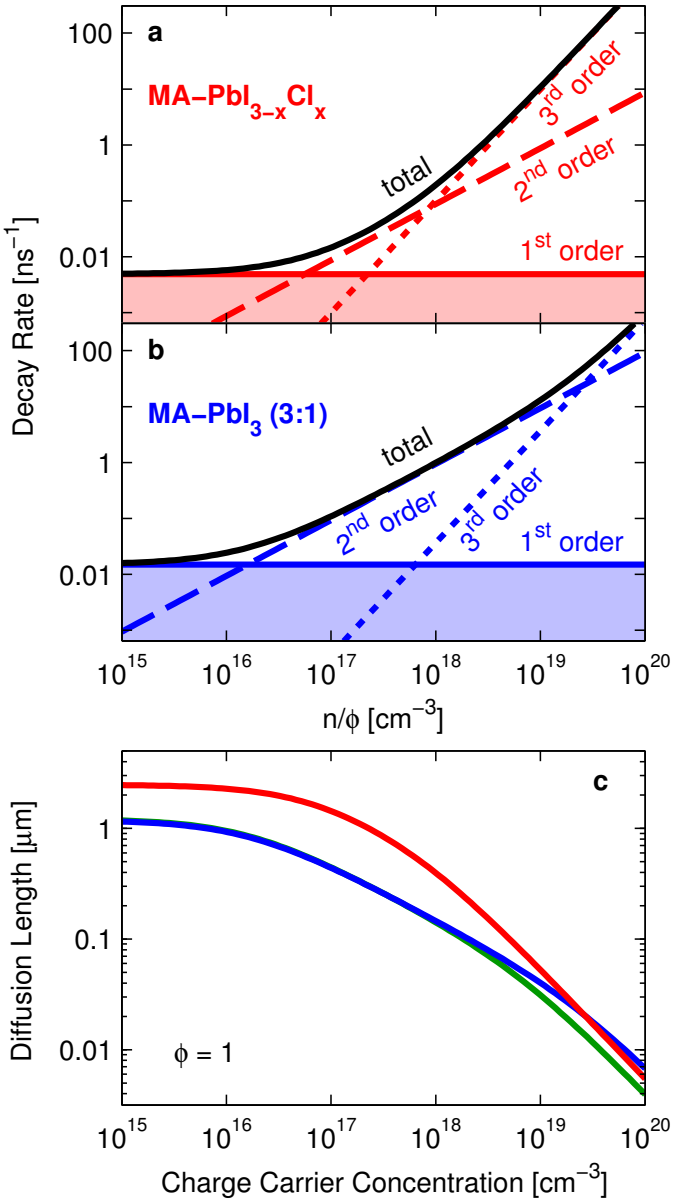

Figure 5.4: Charge-carrier decay rates and diffusion lengths of lead-halide perovskites as a function of charge-carrier concentration, extracted from analysis of transient photoconductivity and photoluminescence measurements. **(a/b)** Charge-carrier decay rates for $CH_3NH_3PbI_{3-x}Cl_x$ and $CH_3NH_3PbI_3$ (3:1) as a function of $n\phi$, where n is the charge-carrier density in the materials and ϕ the ratio of n to the absorbed photon density. Rates are computed from the rate constants determined in this work (see Table 5.2). Plotted are the 1st (mono-molecular, solid), 2nd (bi-molecular, dashed) and 3rd order (Auger, dotted) contribution to the total decay rate (black, solid), where $R_1 = k_1$, $R_2 = \phi k_2\,(n/\phi)$, $R_3 = \phi^2 k_3\,(n/\phi)^2$ and $R_{\text{total}} = \mathrm{d}n/(n\mathrm{d}t)$ is the sum total. **(c)** Charge-carrier diffusion lengths $L = (\mu k_B T/(eR_{\text{total}}))^{1/2}$ for $CH_3NH_3PbI_{3-x}Cl_x$ (red), $CH_3NH_3PbI_3$ (3:1) (blue) and $CH_3NH_3PbI_3$ (1:1) (green) as a function of charge-carrier concentration n, derived from charge-carrier decay rates and THz mobilities of 11.6cm^2/(Vs), 8.1cm^2/(Vs) and 8.2cm^2/(Vs) ($\phi = 1$).

expression:

$$R_{\text{total}}(n) = -\frac{1}{n}\frac{\mathrm{d}n}{\mathrm{d}t} = \phi^2 k_3 \left(n/\phi\right)^2 + \phi k_2 \left(n/\phi\right) + k_1 \stackrel{\text{def}}{=} R_3 + R_2 + R_1. \tag{5.5}$$

Figure 5.4(a,b) shows that both mono- and bi-molecular recombination make dominant contributions at effective charge-carrier densities of $n\phi = 10^{15} - 10^{17}\,\text{cm}^{-3}$, but the associated rate constants (k_1 and k_2) are significantly lower for the mixed halide than the triiodide halide perovskite under typical device operating conditions.

From these rates and the effective mobilities, charge-carrier diffusion lengths are computed as a function of carrier density as follows:

$$L(n) = \sqrt{\frac{D}{R_{\text{total}}(n)}} = \sqrt{\frac{\mu k_B T}{e R_{\text{total}}(n)}} \tag{5.6}$$

Here, $D = \mu k_B T e^{-1}$ is the diffusion constant at room temperature $T = 293\,\text{K}$ as determined from the carrier mobility. The total charge-carrier recombination rate $R_{\text{total}}(n)$ is determined from Equation 5.5.

Figure 5.4(c) displays the dependence of the diffusion length on charge-carrier density derived for the cases of a photon to charge branching ratio of 1, corresponding to THz mobilities of $11.6\text{cm}^2/(\text{Vs})$ and $8.1\text{cm}^2/(\text{Vs})$ for $CH_3NH_3PbI_{3-x}Cl_x$ and $CH_3NH_3PbI_3$ (3:1), respectively. Note that for $\phi < 1$ diffusion lengths would be even larger. The plots show that substantial diffusion lengths in the micron-range are achievable for low charge-carrier densities, in agreement with recent measurements based on diffusive exciton quenching [87]. In accordance with device performance, the mixed-halide perovskite exhibits a diffusion length that is up to a factor four larger than that of the triiodide perovskite over charge-carrier densities corresponding to realistic device operating conditions. In the presence of long range structural disorder, diffusion lengths may be somewhat shorter, as THz conductivity probes sample the material mobility on shorter length scales that may not include full conduction pathways to

electrodes [58]. Such extended charge diffusion lengths are to be expected, given that planar-heterojunction devices have now been realized [15], which require diffusion lengths to be comparable to or exceed optical absorption depths (typically 445 nm at 700 nm excitation and 120 nm at 500 nm excitation wavelength). Here it is shown that the reason for the long charge diffusion lengths is that lead-halide perovskites show strongly sub-Langevin carrier recombination rates. If bi-molecular decay processes were as fast as derived from a kinetic model (Langevin theory), charge diffusion lengths would be reduced to the tens of nanometre range necessitating the use of a bulk heterojunction (mesostructured) device layout. These findings therefore show that the observed combination of low charge-carrier recombination and high mobility is crucial to the development of planar heterojunction photovoltaic devices incorporating organo-lead-halide perovskites.

To propose an explanation for these effects, interesting parallels with early low-temperature measurements on lead-halide ionic crystals are pointed out, which showed that while PbI_2 exhibited sub-nanosecond PL lifetimes [153], the lighter-halide $PbCl_2$ [154] exhibited much longer (microsecond) lifetimes. In some metal halide systems, such effects have been attributed to spatial localization of the hole in the halide vicinity [155]. Clearly, in the lead-halide perovskites under investigation here, charges are found to be highly mobile and trapping mechanisms surprisingly absent. However, a weak preferential localization of electrons and holes in different regions of the perovskite unit cell may still result in a reduction in the spatial overlap of electron and hole wavefunctions and hence recombination rates. Note that density functional calculations on lead-iodide perovskites have revealed that valence band maxima consist of 6s- and 5p orbitals of lead and iodine, respectively, while conduction band minima mostly incorporate 6p-orbitals of lead [78]. This scenario is reminiscent of the case of metal alkali halides for which long life times had been reported earlier [155]. Such spatial charge separation may explain the stark deviation from Langevin theory observed here for charge recombination in the organo-lead-halide perovskites. Understanding

and predictive modelling of such effects will therefore allow for directed photovoltaic material and device development.

5.2.5 THz Conductivity Spectra

In order to support the assumptions made for the modelling of THz photoconductivity transients (i.e. in terms of the decay of the free carrier population), and to obtain further insights into the nature of charge transport in the materials, frequency spectra of the THz photoconductivity were acquired. These are shown for $CH_3NH_3PbI_3$ and $CH_3NH_3PbI_{3-x}Cl_x$ in Figure 5.5 as recorded at pump-probe delays between 5 ps and 2 ns. Importantly for each sample there is no significant change in the spectra as a function of time after photoexcitation (i.e. no pump-probe delay dependence of the photoinduced phase shift of the transmitted THz pulse in the time domain). In this case carrier dynamics may be recorded by observing changes in the peak terahertz signal in the time domain as a function of pump-probe delay [100].

The shape of the transient THz photoconductivity spectra are consistent with the motion of photogenerated free charge exhibiting long-range scattering [98, 99, 100, 136, 137, 156]. Over the measurable frequency range (0.2–3 THz) the real part of the conductivity ($\propto \Delta T/T$ see Eqn. 3.1) is offset from zero and relatively constant and the imaginary part of the conductivity is close to zero. This is consistent with a Drude conductivity, with relaxation rate $\gg 3$ THz [99, 100]. In addition the features observable at 1 THz and 2 THz originate from a photoinduced modulation of LO-phonon modes superimposed on the Drude response. The LO-photon modes can be seen in the absorption spectrum of the unilluminated samples, which are shown in Figure 5.6.

Furthermore a control experiment was performed showing that the shape of the THz spectrum is independent of the electric field strength of the THz pulse (see Figure 5.7), to confirm that the THz pulse was acting as a weak probe.

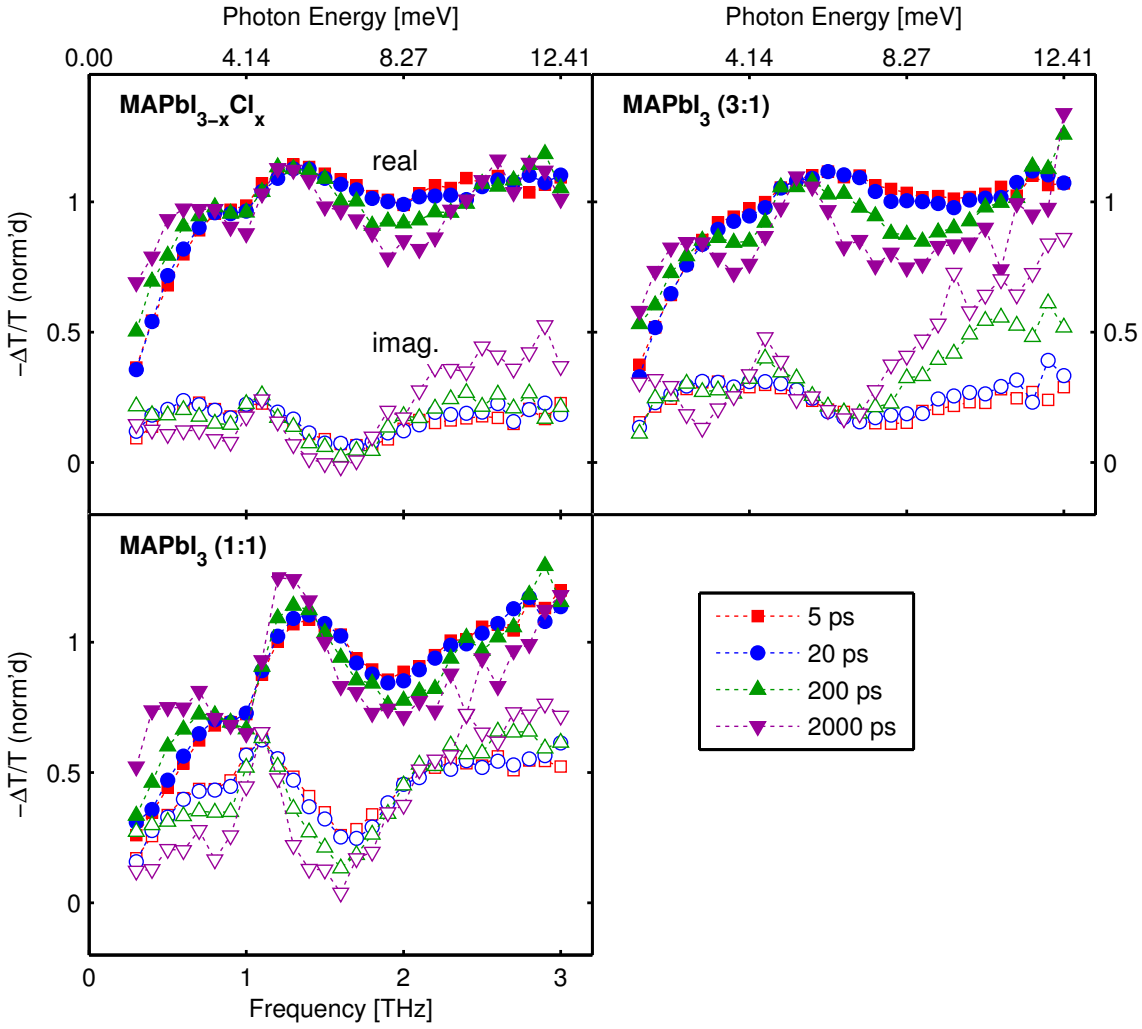

Figure 5.5: Photoinduced THz absorption spectra of $CH_3NH_3PbI_3$ and $CH_3NH_3PbI_{3-x}Cl_x$ at various times after excitation. (Excitation wavelength: 550 nm), fluence: 320 $\mu J/cm^2$. For comparability, all spectra are normalized by their frequency-averaged absolute value.

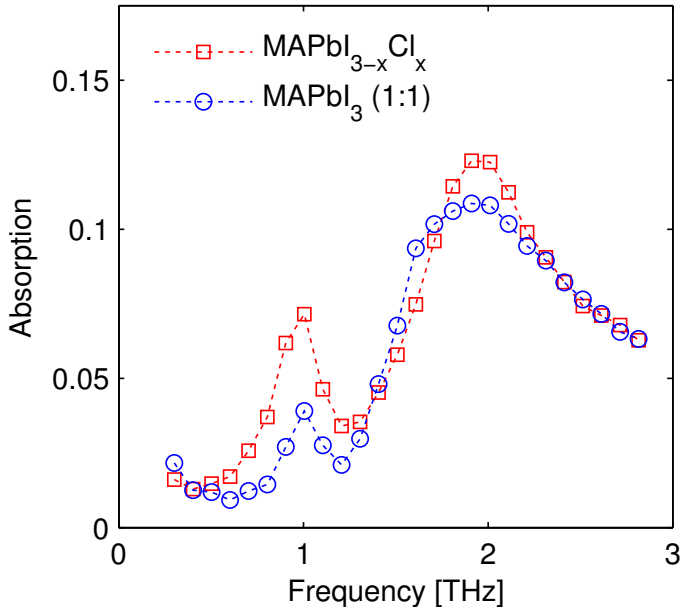

Figure 5.6: Dark THz absorption spectra of $CH_3NH_3PbI_{3-x}Cl_x$ and stoichiometric $CH_3NH_3PbI_3$.

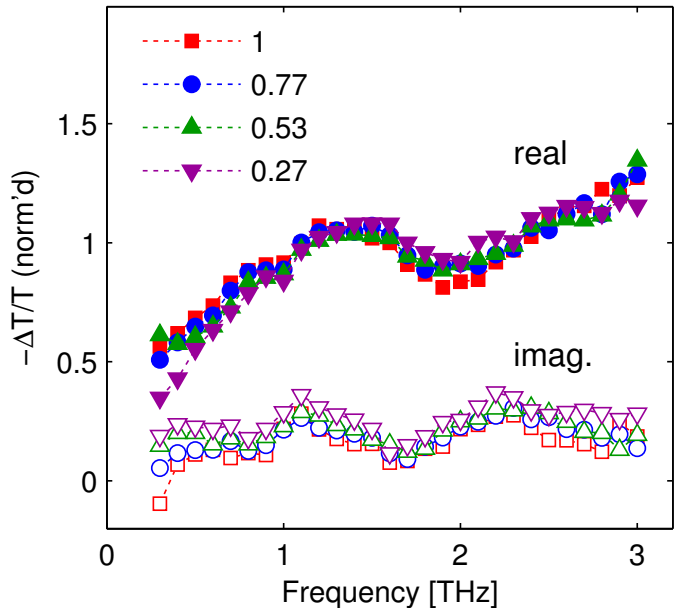

Figure 5.7: Photoinduced THz absorption spectra of meso-superstructured $CH_3NH_3PbI_{3-x}Cl_x$ at various electric field strengths of the THz probe pulse. (Excitation wavelength: 550 nm), fluence: 320 $\mu J/cm^2$. The legend indicates the relative electric field strengths used. For comparability, all spectra are normalized by their frequency-averaged absolute value.

5.3 Conclusion

The results presented in this chapter reveal that $CH_3NH_3PbI_3$ and $CH_3NH_3PbI_{3-x}Cl_x$ are particularly well-suited as light absorbers and charge transporters in photovoltaic cells, because they allow an unexpected combination of both low charge recombination rates and high charge-carrier mobilities. Lower bounds of $\sim 10\,\mathrm{cm}^2/(\mathrm{Vs})$ for the high-frequency charge mobility are established, which is remarkably high for a solution-processed material. Planar heterojunction photovoltaic cells may only be achieved because the ratio of bi-molecular charge recombination rate to charge mobility is over four orders of magnitude lower than that predicted from Langevin theory. Such effects are likely to arise from spatial separation of opposite charge carriers within the metal-halide structure. Modelling and tuning recombination channels, e.g. through halide and metal substitutions, will hold the clue to raising material performance.

6

Charge Transport and Recombination in Vapour-Deposited, Compact Films of $CH_3NH_3PbI_{3-x}Cl_x$

Vapour deposition is a well-established technique in the commercial fabrication of optoelectronic devices, offering a wide range of benefits in terms of cost, scalability, environmental impact and high film quality [157, 158, 159]. An exciting recent example has been the demonstration of thin-film organo-lead halide perovskites solar cells from a simple dual-source evaporation protocol [15]. These cells were found to exhibit high power conversion efficiencies of up to 15.4 % based on a simple planar heterojunction device design. In comparison to solution processing techniques, vapour deposition allows for high film homogeneity, avoiding problems caused by de-wetting and subsequent pin-hole formation [72]. In addition, vapour deposition greatly simplifies the fabrication of tandem cells comprising material layers of complementary absorption spectra, obviating the need for orthogonal solvents and more elaborate cross-linking schemes. Such tandem cells can potentially surpass the theoretical Shockley-Queisser limit for the power conversion efficiency of 33 % for single-junction cells [18, 21]. For cells based on $CH_3NH_3PbI_{3-x}Cl_x$, this concept is particularly attractive since the bandgap energy of near 1.6 eV (see Figure 5.1) is larger than the optimum value,

leaving a wide spectral range in the near-infrared unused.

The past year has seen a tremendous surge of research on organo-lead halide perovskites after the first high-efficiency solid state solar cells based on these materials were reported [13, 14]. Data on many fundamental material properties of these materials is emerging and the understanding of the principal optoelectronic processes governing photovoltaic operation has increased significantly [9, 10]. Apart from the intrinsic material properties that render organo-lead halide perovskites so suitable as absorbers in solar cells, non-intrinsic factors such as morphology [74, 160], crystallinity and stoichiometry ([77] and Chapter 5) have been found to have considerable effects on device performance [161]. However, past studies have almost exclusively been performed on materials prepared through solution-based deposition protocols. Given the attractive benefits of vapour deposition, further knowledge on relevant properties for photovoltaic operation of these films is therefore urgently required. Such information may also reveal which particular aspects of the charge generation and recombination processes are inherent to a given material, and which elements may be further tuned through suitable alterations of the fabrication protocol.

In this chapter, recombination lifetimes and carrier mobility as two key properties for photovoltaic operation are measured in vapour-deposited films of the lead halide perovskite $CH_3NH_3PbI_{3-x}Cl_x$ in a similar way as done for the meso-superstructured, solution processed perovskties in the previous chapter. Materials were made using a dual-source evaporation protocol (CH_3NH_3I / $PbCl_2$) in the same way as previously reported for incorporation in high-efficiency solar cells [15]. Again, the photoinduced THz conductivity of the film was monitored over a wide range of excitation densities and recombination rate constants extracted. In addition, a remarkably high charge-carrier mobility in excess of $33\,cm^2/(Vs)$ is determined. Taken together, the results in this chapter show that vapour-deposited $CH_3NH_3PbI_{3-x}Cl_x$-films allow for charge-carrier diffusion lengths in excess of several microns under typical solar-cell

operating conditions. As also observed in meso-superstructured, solution processed materials, these long diffusion lengths result from a combination of both, low bimolecular electron-hole recombination rates far below the prediction of the Langevin model, and slow effective trap-mediated recombination of charge carriers.

6.1 Experimental Details

6.1.1 Sample Preparation

Thin films of the perovskite $CH_3NH_3PbI_{3-x}Cl_x$ were deposited by *Mingzhen Liu* using dual-source evaporation as described in detail in [15]. Lead chloride ($PbCl_2$) and methylammonium iodide (CH_3NH_3I) were deposited simultaneously onto 2 mm thick z-cut quartz substrates under high vacuum. Before starting the evaporation, the tooling factor (which is a ratio of the material deposited on the sensors to that on the samples) was estimated for each source individually.

Approximately 500 mg of CH_3NH_3I and 100 mg of $PbCl_2$ were loaded into separate crucibles and the substrates were placed in a substrate holder above the sources. To eliminate volatile impurities in the chamber before coating the substrates with perovskite, the two crucibles were heated above the desired deposition temperatures under high vacuum (10^{-5} mbar) for approximately 5 min. To prepare representative perovskite films, key deposition parameters such as the deposition rates and duration for the two sources were set as previously optimized for best performance of the material in solar cells [15]. This includes using a CH_3NH_3I:$PbCl_2$ molar ratio of 4:1 and deposition rates of 5.3 $Å s^{-1}$ for CH_3NH_3I (crucible temperature around 116 °C) and 1 $Å s^{-1}$ for $PbCl_2$ (crucible temperature of around 320 °C), maintained for approximately 128 min of evaporation. The substrate holder was rotated to ensure uniform coating while the film was deposited on the substrate. Annealing the as-deposited films at 100 °Cfor 45 min in a N_2-filled glove box enabled full crystallization of the per-

ovskite, darkening the colour and resulting in an apparent growth of crystal features visible in SEM images [15]. The resulting film thickness is 330 ± 5 nm.

6.1.2 THz Time-Domain Spectroscopy

The optical-pump-THz-probe setup used is identical to the one described in 5.1.4.

6.2 Results and Discussion

6.2.1 THz Charge-Carrier Dynamics

For the interpretation of the photoinduced THz response of $CH_3NH_3PbI_{3-x}Cl_x$, similar considerations apply regarding which photoexcited species the THz probe pulse couples to, as in Chapter 5. First the frequency spectrum of the photoinduced THz response is therefore analysed, which reveals information about the types of excitations the probe pulse interacts with. Figure 6.1 shows THz photoinduced absorption spectra for $CH_3NH_3PbI_{3-x}Cl_x$ recorded at 20 ps and 2 ns pump-probe delay. The spectral shape does not change with time after excitation and displays an essentially flat real part and only a very small imaginary component. Such a response is consistent with the predictions of a standard Drude conductivity model for free carriers at frequencies much lower than the relaxation rate [99, 100]. It is therefore concluded that also in evaporated films, the observed OPTP signal predominantly arises from the interaction of the THz probe with free charge carriers.

It is also worth noting that the THz spectra show no substantial signs of disorder-induced scattering phenomena, which generally cause a drop of the real part and the emergence of a non-zero imaginary part of the conductivity towards low frequencies [136, 137]. This is in agreement with the existence of relatively large crystalline domains previously reported for these vapour-deposited thin films [15].

It can also be seen that the THz spectra show some weak additional features centred

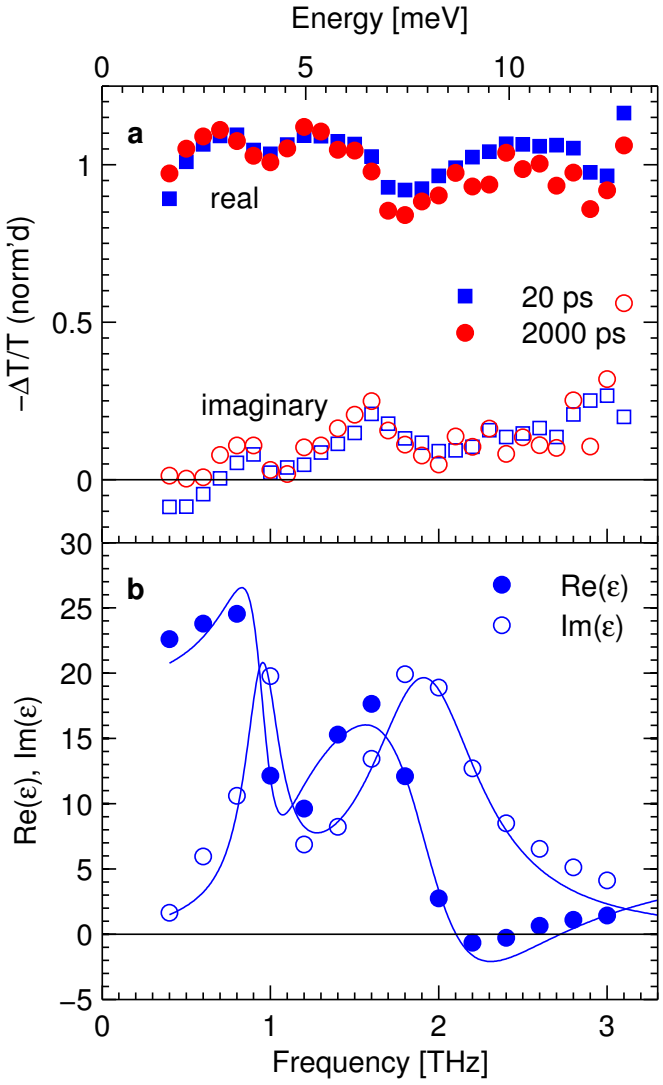

Figure 6.1: **(a)** Normalized, complex THz photoinduced absorption spectra of vapour-deposited $CH_3NH_3PbI_{3-x}Cl_x$ (closed symbols real parts, open symbols imaginary parts) for two different time-delays (20 ps and 2000 ps) after excitation at 550 nm (2.25 eV) with pulse fluence 280 $\mu J/cm^2$. The slight drop-off towards low frequencies (< 0.5 THz) is due to an artefact resulting from the large diffraction limited beam waist for these frequency components approaching the diameter of the optical pump beam. **(b)** THz dark permittivity spectra (no photoexcitation), fitted with the output of a Lorentz Oscillator model including two resonances as described in the text.

at around 1 THz and 2 THz. Such features may arise from resonant interaction of light e.g. with phonon modes or intra-excitonic transitions [103, 162]. To examine the origin of these features, the THz permittivity spectrum was also measured in absence of photoexcitation, which is shown in Figure 6.1b. These spectra show two clear resonances in the same spectral regions for which weak features are observed in the photoinduced conductivity spectra. The contribution of these resonances to the dark spectra can be modelled as Lorentzian oscillators resulting in the Drude-Lorentz response described by the equation [103]:

$$\epsilon_{\mathrm{ph}}(\omega) = -\Delta\epsilon_s \frac{\omega_0^2}{\omega^2 - \omega_0^2 + i\gamma\omega} \tag{6.1}$$

Here, $\Delta\epsilon_s$ is the contribution of the mode to the static permittivity, ω_0 its (angular) resonance frequency and γ its half line width. The complete expression includes the sum of the two oscillator terms as well as the (high-frequency) background permittivity ϵ_∞ arising from all contributions above the accessible frequency range.

$$\epsilon(\omega) = \epsilon_{\mathrm{ph}}^{(1)}(\omega) + \epsilon_{\mathrm{ph}}^{(2)}(\omega) + \epsilon_\infty \tag{6.2}$$

This complex valued function was fitted simultaneously to the real and imaginary part of the measured permittivity. The results are summarized in Table 6.1. The low-frequency permittivity (i.e. the high-frequency background for the range below 0.5 THz) may be calculated as

$$\epsilon_s = \epsilon_\infty + \Delta\epsilon_s^{(1)} + \Delta\epsilon_s^{(2)} \tag{6.3}$$

The spectral resolution of the measurement is given by the Fourier-transform limit through the length of the acquired interval in the time-domain ($\Delta t = 5$ ps) resulting in $\Delta\omega = 2\pi/\Delta t = 1.26$ THz. The widths of the Drude-Lorentz peaks determined through the fits ($2\gamma > 1.26$ THz) are therefore not affected by the spectral resolution

limit. Note that phonon lifetimes can be directly obtained from these line width as $\tau = 1/\gamma$ [103].

The fits yield resonance frequencies $f_0^{(1)} = 0.96\,\mathrm{THz}$ and $f_0^{(2)} = 1.96\,\mathrm{THz}$. A mode centred at a wavenumber of $62\,\mathrm{cm}^{-1}$ (1.86 THz) has previously been observed in Raman spectra of $CH_3NH_3PbCl_3$ [163] and $CH_3NH_3PbI_3$ [164], and was assigned to vibrational modes associated with bending and stretching of the lead-halide bonds. The features observable in the photoconductivity spectra therefore most likely arise from a photoinduced modulation of such lead-halide sub-lattice phonon modes superimposed on the Drude conductivity response. This scenario suggests that charge carriers couple effectively to lattice vibrations in $CH_3NH_3PbI_{3-x}Cl_x$. Hence polaronic effects may have to be taken into account when the electronic properties of this material are considered.

In the following charge-carrier recombination dynamics in vapour-deposited $CH_3NH_3PbI_{3-x}Cl_x$ films are investigated in a similar way as in Chapter 5 through analysis of the results from time-dependent optical-pump-THz-probe experiments. Figure 6.2 shows THz absorption transients after photoexcitation at 550 nm (2.25 eV) for a range of excitation fluences between 6 and $188\,\mu\mathrm{J/cm}^2$. Again, the time-dependence of the transients is modelled in terms of a free-charge population decay, neglecting possible changes of carrier mobility on the investigated timescale.

First a value is extracted for the charge-carrier mobility at THz frequencies for the material from the photoinduced THz transmission change extrapolated to zero pump-

	$\epsilon_{\mathrm{ph}}^{(\mathbf{1})}$	$\epsilon_{\mathrm{ph}}^{(\mathbf{2})}$	ϵ_∞	ϵ_s
$\boldsymbol{\Delta\epsilon_s}$	4.8	7.98	6.81	19.59
$\omega_{\mathbf{0}} = \mathbf{2\pi f_0}$ [THz]	6.04	12.28		
γ [THz]	1.60	5.11		

Table 6.1: Results of the fit of Equation 6.2 to the THz permittivity spectra. Note that ϵ_s is given as calculated from Equation 6.3 and not itself a fit parameter.

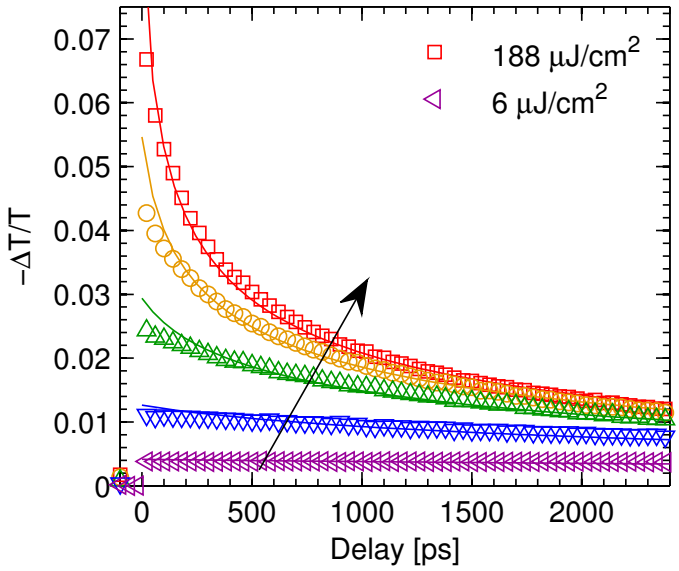

Figure 6.2: THz photoinduced absorption transients of vapour-deposited thin films of $CH_3NH_3PbI_{3-x}Cl_x$ at excitation fluences between 6 and 188 µJ/cm^2 and for excitation wavelength 550 nm (2.25 eV). Solid lines represent fits with a 1st-, 2nd- and 3rd-order decay function with globally optimized rate constants (equal for all fluences) as described in the text.

probe delay. Regarding the relevance of the photon-to-free-carrier conversion ratio ϕ, very similar arguments apply as for the experiments on meso-superstructured, solution processed perovskites. Hence, while noting the same highly non-resonant excitation conditions, which in principle ought to primarily generate free carriers, the effective carrier mobility $\phi\mu$ is stated as a lower limit to the actual mobility (since $0 < \phi < 1$).

A value of $\phi\mu = 33\,\mathrm{cm}^2/(\mathrm{Vs})$ is calculated, which is remarkably high, in agreement with the efficient charge extraction from photovoltaic devices made from such films [15]. This effective mobility for films of evaporated $CH_3NH_3PbI_{3-x}Cl_x$ is higher than that determined in Chapter 5 for the solution-processed material within a mesoporous scaffold, which is most likely the result of the different film morphologies and crystalline domain sizes [15, 72]. Note moreover that $\phi\mu$ as determined here is only a factor of two lower than the value of μ obtained by means of Hall-effect measure-

ments for annealed polycrystalline pellets of the related $CH_3NH_3PbI_3$ [82]. This observation suggests that the photon-to-free-charge conversion efficiency ϕ is sizeable in these materials, i.e. for the non-resonant excitation used in the experiments here, the majority of species generated appear to be free charges, rather than excitons. Therefore, it seems that free charges are readily available in these materials following non-resonant photoexcitation, which is highly advantageous for their use in photovoltaic energy conversion.

In the next step, the charge-carrier recombination dynamics that govern the decay of the photoconductivity transients shown in Figure 6.2 are analysed. Drawing from the insights of Chapter 5, a simple model involving recombination processes of first, second and third order as described by the rate equation

$$\frac{\mathrm{d}n(t)}{\mathrm{d}t} = -k_3 n^3 - k_2 n^2 - k_1 n \ , \tag{6.4}$$

is applied, where k_3 is the decay constant describing Auger recombination [145, 146], k_2 the bi-molecular recombination constant, and k_1 the rate for mono-molecular processes such as trap-assisted charge recombination. Note that, again, fitting the above rate equation to the transients actually results in the extraction of the decay constants $k_3\phi^2$, $k_2\phi$ and k_1, with the former two representing lower limits to the actual values k_2 and k_3 (refer to 5.2.2 and specifically Equation 5.4 for the mathematical details of the fits). Decay constants were only allowed to vary globally (i.e. had constant values across curves taken at all fluences). The resulting fits are plotted as solid lines in Figure 6.2 with the extracted values for the effective second- and third-order decay constants given in Table 6.2. A generally low value for the effective bi-molecular recombination rate is found, which is similar to (i.e. 20 % lower than) the value determined previously for meso-superstructured, solution-processed $CH_3NH_3PbI_{3-x}Cl_x$ (see Chapter 5).

While extracting the mono-molecular rate constant k_1 from the fits to the THz pho-

Material	$CH_3NH_3PbI_{3-x}Cl_x$
Decay constants	
3rd order ($\phi^2 k_3$)	$2.7 \times 10^{-29}\,\mathrm{cm^6 s^{-1}}$
2nd order (ϕk_2)	$1.1 \times 10^{-10}\,\mathrm{cm^3 s^{-1}}$
1st order (k_1, see Chapter 7)	$1.2 \times 10^{7}\,\mathrm{s^{-1}}$
Eff. mobility ($\phi\mu$)	$33\,\mathrm{cm^2/(Vs)}$
Langevin Ratio	$2 \times 10^{-6} \times \epsilon_r$

Table 6.2: Charge-carrier decay rate constants and mobility for vapour-deposited $CH_3NH_3PbI_{3-x}Cl_x$. Strictly, the given values for second and third order decay constants, and the effective charge-carrier mobility are lower limits to the actual values of k_2, k_3 and μ because the photon-to-free-charge conversion efficiency ϕ may be lower than unity ($0 \leq \phi \leq 1$). The *Langevin Ratio* denotes the ratio between the observed value of k_2/μ to that theoretically predicted by the Langevin model $e/(\epsilon_0\epsilon_r)$. The value stated is exclusive of the factor accounting for the relative permittivity. The static dielectric constant of $CH_3NH_3PbI_3$ $\epsilon_s = 60$ [165] may serve as an upper limit. The mono-molecular decay rate k_1 is determined from time-resolved photoluminescence measurements in Chapter 7.

toconductivity transients, again extremely low values are also found for this rate-constant, indicating than a precise measurement requires a longer accessible time-scale than the THz experiment provides. From the uncertainty of the fits an upper limit can however be established for k_1 of approximately $2 \times 10^7\,\mathrm{s^{-1}}$. As explained in detail in 5.2.3 an estimate of the mono-molecular charge-carrier decay rate may be derived from the time-resolved photoluminescence (PL) decay, which can straightforwardly be acquired over timescales of hundreds of nanoseconds by means of time-correlated single photon counting. This data has been collected in the course of the study presented in Chapter 7 (Figure 7.3b). There it is shown that for low-fluence excitation, the PL transients exhibit mono-exponential decay tails from which a mono-molecular rate constant $k_1 = 1.2 \times 10^7\,\mathrm{s^{-1}} = (83\,\mathrm{ns})^{-1}$ is extracted. It was argued in 5.2.3 that although possibly reflecting a combination of both excitonic and free charge-carrier populations, the dynamics observed through time-resolved PL provide a useful reference point and at least an upper limit for k_1. This assumption is supported by recent observations of similar decay dynamics observed for both photoinduced absorption

and PL emission in $CH_3NH_3PbI_{3-x}Cl_x$ films [87], and a study of transient microwave conductivity of $CH_3NH_3PbI_3$ on nanosecond-to-microsecond timescales showing coinciding decay lifetimes for photoluminescence and photoconductivity [166]. The monomolecular decay rate for vapour-deposited $CH_3NH_3PbI_{3-x}Cl_x$ determined through PL spectroscopy is very low for a polycrystalline material, and only slightly (by about a factor of two) higher than that for meso-superstructured, solution processed $CH_3NH_3PbI_{3-x}Cl_x$. This result suggests that $CH_3NH_3PbI_{3-x}Cl_x$ has a generally low propensity to trap free charge carriers, regardless of the general processing route taken.

A comparison of the determined bi-molecular recombination rate to the prediction of Langevin theory [142, 143] ($k_{2,\mathrm{L}} = \mu e(\epsilon_0\epsilon)^{-1}$) yields a discrepancy of about five orders of magnitude (i.e. tremendously slower recombination then predicted) in agreement with the results on meso-superstructured, solution-processed $CH_3NH_3PbI_{3-x}Cl_x$. This organo-lead halide perovskite therefore fundamentally appears to exhibit particular mechanisms inhibiting electron-hole recombination, independent of the deposition route. In Chapter 5 it was proposed that polarization of free-charge pairs across the metal-halide bond may be a cause of stabilization for a spatially charge-separated state. Such effects have been intensively examined for a range of ionic solids such as alkali halides [155], for which the valence band has strong halide character (i.e. localizing the hole in the halide vicinity), and they are also apparent in recent density-functional calculations for $CsPbI_3$ perovskites [78].

Alternatively, more extended electron-hole spatial separations may be induced through built-in electric fields. Many materials in perovskite structures with lack of inversion symmetry display ferroelectric effects [167, 168], allowing such fields to be present even in the bulk material. The extent to which $CH_3NH_3PbI_{3-x}Cl_x$ and related compounds exhibit ferroelectricity is still unknown, however, if such effects were to be present, they could aid photovoltaic performance by facilitating initial charge separation and by inhibiting subsequent recombination [168]. An understanding of

the mechanisms for the observed strongly non-Langevin electron-hole recombination dynamics would allow design rules to be established for a wider class of materials for photovoltaics.

6.2.2 Charge-Carrier Diffusion Length

With knowledge of charge-carrier mobility and lifetimes in $CH_3NH_3PbI_{3-x}Cl_x$ the charge diffusion length may be calculated, which is central to the performance of absorber layers in solar cells. Especially in planar heterojunction device architectures, charge-carrier diffusion lengths are required that sufficiently exceed the thickness of the active layer (currently ∼330 nm in planar heterojunction $CH_3NH_3PbI_{3-x}Cl_x$ based cells [15]) to achieve satisfactory current densities under working conditions where no electric field is present.

L_D is evaluated as a function of n as described in 5.2.4, using the determined recombination rate constants and charge mobility listed in Table 6.2. The resulting plots are shown in Figure 6.3 for which a photon-to-free-charge conversion ratio $\phi = 1$ was assumed for simplicity. For charge-carrier concentrations covering realistic solar cell operating conditions, it can be seen that the diffusion length in $CH_3NH_3PbI_{3-x}Cl_x$ is on the order of microns (2.7 μm at $n = 10^{15}\,\mathrm{cm}^{-3}$) and is only limited by mono-molecular decay processes. At higher concentrations ($n \geq 10^{18}\,\mathrm{cm}^{-3}$) bi-molecular and finally Auger recombination reduce the diffusion length to the sub-micron range. Note that these diffusion lengths are probed at THz frequencies causing only short-range carrier displacement and thus the long-range DC values may be somewhat shorter, if the mobility is strongly inhibited by grain boundaries. On the other hand, if ϕ was to be lower than unity, the calculated diffusion lengths would be even larger.

In addition, Figure 6.3 also shows the diffusion lengths expected for the two hypothetical cases of (i) solely kinetically limited bi-molecular recombination rates (Langevin recombination, $k_2 = \mu e(\epsilon_0\epsilon)^1$), and for (ii) complete absence of mono-molecular decay

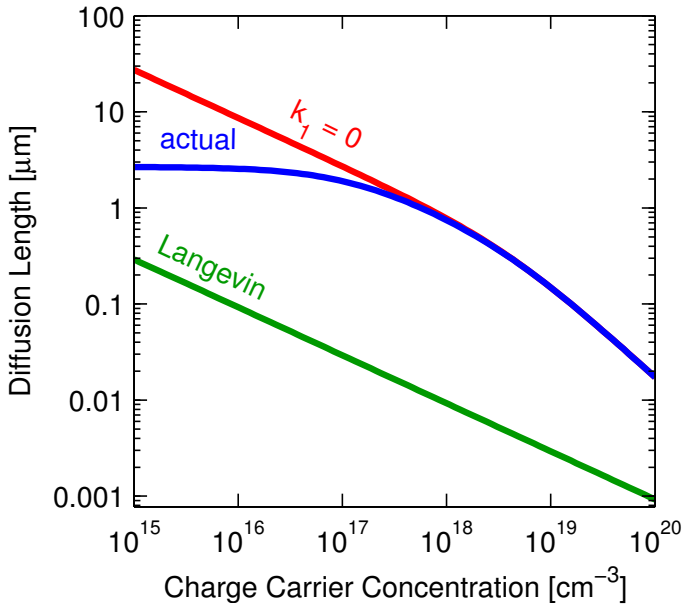

Figure 6.3: Charge-carrier diffusion lengths as a function of charge-carrier density, calculated from the decay rate constants in Table 6.2, assuming a photon-to-free-charge conversion efficiency $\phi = 1$. The blue line shows the actual diffusion length to be expected from the measured first-, second- and third-order rates. The red and green lines show hypothetical values for the two cases of (i, green): bi-molecular recombination rates instead being governed by Langevin recombination, i.e. $k_2 = \mu e(\epsilon_0\epsilon)^1$, taking the low-frequency limit of $\epsilon = \epsilon_s = 60$ [165], and for (ii, red): complete absence of mono-molecular decay channels ($k_1 = 0$). A recent estimation suggests that realistic carrier concentrations in working $CH_3NH_3PbI_{3-x}Cl_x$-based solar cells are on the order of $10^{15}\,cm^{-3}$ or less [91].

channels ($k_1 = 0$). The plot shows that the situation would change dramatically if the material were to exhibit Langevin-recombination (case (i)). Here, bi-molecular recombination would dominate through the entire density range shown in the plot limiting the diffusion length to a few tens of nanometres at a carrier concentration of $10^{15}\,\mathrm{cm}^{-3}$. Without the observed non-Langevin decay mechanisms, these materials would therefore only find application as thin sensitizer layers on nano- or meso-structured electron- and hole-extracting layers, such as those employed in dye-sensitized solar cells. For case (ii) on the other hand, the elimination of trap-mediated decay channels would enhance the diffusion length significantly ($29\,\mu$m at $n = 10^{15}\,\mathrm{cm}^{-3}$) and make it dependent on absorbed photon flux over the typical solar cell operating range.

Note that previously reported values of k_1 for solution processed films ([87] and Chapter 5) are lower than the mono-molecular rate measured here for vapour-deposited films. This comparison suggests that the mono-molecular charge recombination rate is governed at least to some extent by defects or impurities in the bulk and at grain boundaries, which can be targeted by careful engineering of the processing route. In this respect, improvements of the vapour deposition protocol could very well hold the potential for solar cells showing even higher photocurrents and power conversion efficiencies.

6.3 Conclusion

In this chapter, two key properties for photovoltaic operation, charge-carrier mobility and lifetime, were investigated for vapour-deposited films of the organo-lead halide perovskite $CH_3NH_3PbI_{3-x}Cl_x$. The high-quality films obtained through dual-source evaporation show excellent charge-carrier mobility of at least $33\,\mathrm{cm}^2/(\mathrm{Vs})$, and low bi-molecular recombination rates that defy the prediction of the Langevin model by about five orders of magnitude. As a result, the diffusion lengths are only limited

by mono-molecular decay processes under realistic solar cell operating conditions. It is found that the extracted long diffusion lengths approaching 3 microns result from the combination of both non-Langevin bi-molecular electron-hole recombination, and exceptionally low trap-induced mono-molecular charge recombination pathways.

In comparison to the results from Chapter 5 on meso-superstructured, solution-processed films of $CH_3NH_3PbI_{3-x}Cl_x$, vapour-deposited films exhibit higher charge-carrier mobilities and mono-molecular recombination rates, but similar bi-molecular recombination. This change in the former two parameters coincidentally cancels when the diffusion lengths are evaluated, leading to similar calculated values of L_D for the two processing methods. Comparison of parameters obtained for the two deposition routes suggests that while the non-Langevin bi-molecular decay rates are an inherent property of this material, charge-carrier mobilities and trap densities may vary with processing conditions. Finding ways to identify and eliminate traps, and to enlarge crystallite size further, would therefore allow further increases in photovoltaic device efficiencies.

In addition, there is a clear need for finding an explanation for the underlying mechanism causing the observed non-Langevin charge recombination. This mechanism could also be to some extent responsible for the large fraction of initially generated free-charge carriers that appear to be present following light absorption. Such an understanding would greatly aid the development of new material classes that not only exhibit excellent photovoltaic performance, but also have additional benefits such as higher long-term stability or lead-free composition.

7

Spectral Broadening of Photoluminescence Emission from $CH_3NH_3PbI_{3-x}Cl_x$

In the previous chapters, some of the very favourable optoelectronic properties of $CH_3NH_3PbI_3$ and $CH_3NH_3PbI_{3-x}Cl_x$ for photovoltaic applications were highlighted. The most important ones are strong optical absorption in the visible and ultraviolet spectrum [14], long free charge-carrier lifetimes and high carrier mobilities (see also [87, 88, 169]). These properties are also highly desirable for many other optoelectronic applications, where organic-inorganic perovskites could once more lead to a step change in feasibility or performance. However, little in-depth knowledge exists to date on what governs the behaviour of the emissive species in these materials.

In this chapter the intense, broad band-edge luminescence from $CH_3NH_3PbI_{3-x}Cl_x$ is investigated with the intention of unravelling the nature of the emission line broadening and the underlying radiative recombination processes. This study focusses on thin films fabricated from thermal vapour deposition, which allows for smooth film-formation and high crystalline order making them very suitable for general device applications [15]. Using photoluminescence spectroscopy with continuously tunable excitation energy, the broadening mechanism in the mixed halide $CH_3NH_3PbI_{3-x}Cl_x$ is scrutinized, which features an emission peak around its band gap energy (1.62 eV)

with a full width at half maximum (FWHM) of 103 meV. By scanning the excitation energy across the width of this peak while observing the spectral shape of the PL emission, it is established that the spectral broadening is homogeneous. Furthermore, time-resolved emission spectra are acquired, which show an invariant shape over the captured interval between 200 ps and 200 ns after excitation, suggesting an absence of significant disorder-related effects in the emissive species. Based on the observations in this chapter, strong phonon coupling of charge carriers arising from their polaronic properties is proposed as a likely source of the homogeneous broadening. Owing to the uncertainty relation between pulse duration and frequency bandwidth manifested in the natural spectral line width, a broad emission spectrum is one of the primary prerequisites for gain materials in ultrashort (femtosecond) pulsed lasers [170]. Here, perovskites could also offer a perspective for electrically pumped designs creating a significant advantage over many well-established fs-laser gain materials which require optical pumping. With the observed spectral width of 103 meV, the homogeneous gain medium could sustain amplification of light pulses as short as 6.4 fs.

7.1 Experimental Details

7.1.1 Sample Preparation

Samples were prepared in the same way as described in 6.1.1.

7.1.2 Photoluminescence Spectroscopy

Excitation-energy-dependent PL

PL with continuously tunable excitation is performed using the experimental setup described in 3.2.3 based on a tunable Ti:Sapphire laser operated in continuous wave mode. The intensity incident on the sample is stabilized at about 5 W cm^{-2} across the full photon energy range. Samples are mounted in a vacuum cell maintaining a pres-

sure below 10^{-5} mbar. In this environment the materials is observed to be stable over days involving exposure to the excitation light for many hours, with no degradation in PL or visual change in film appearance observed for the duration of the measurements. Entry slit width and grating constant of the monochromator are chosen to achieve a spectral resolution $\Delta\Lambda$ better than 0.5 nm. The spectrally resolved PL is detected by a nitrogen cooled Si-CCD detector and corrected for spectral response of the apparatus by using a tungsten filament lamp of known emissivity spectrum. Unless otherwise stated, measurements were taken at room temperature (297 K).

Time-resolved PL

Time-resolved PL experiments are performed by means of time-correlated single photon counting using the setup described in 3.2.4. A pulsed diode laser operating at a photon energy of 1.96 eV (634 nm) excites the sample, which is contained in a vacuum chamber at pressures below 10^5 mbar, with a repetition rate of 2 MHz. The grating monochromator is configured to provide spectral filtering with a resolution $\Delta\Lambda$ of about 2 nm. The variable attenuator in the emission path is used to ensure counting rates are kept below 1 % of the repetition rate to avoid multi-photon events. All measurements were taken at room temperature (297 K).

7.1.3 Optical Transmittance and Reflectance Spectroscopy

Optical transmittance and reflectance spectra were acquired in a Perkin-Elmer Lambda 1050 UV/VIS/NIR spectrophotometer operated at a spectral resolution of 2 nm.

7.2 Results and Discussion

7.2.1 Optical Properties

Figure 7.1a displays the optical transmission and reflection spectra of a vapour-deposited $CH_3NH_3PbI_{3-x}Cl_x$ film in the NIR/vis range. The onset of inter-band absorption can be identified as an edge centred at 1.64 eV, in agreement with previously published data on thin films of solution-processed mixed halide $CH_3NH_3PbI_{3-x}Cl_x$ [14, 82, 87] and trihalide $CH_3NH_3PbI_3$ [171] materials. At photon energies below the steep absorption onset at 1.64 eV, the transmittance and reflectance spectra exhibit clear thin-film-interference (Fabry-Perot) effects, which indicates that the film thickness is very uniform and the surface optically flat, preventing any substantial light scattering. From the data in Figure 7.1a, and the film thickness $d = 330$ nm (determined from SEM cross sectional imaging) the absorption coefficient shown in Figure 7.1b is obtained together with the PL emission spectrum. Since information on excitonic effects is still emerging and the exact nature of the electronic structure near the band edge is still being explored, extraction of the precise band gap energy is difficult due to the lack of an unambiguous physical description of the absorption onset. A direct semiconductor in accordance with the results of band-structure calculations [75, 76, 77, 78] ought to exhibit a broad regime for which $\alpha \propto (E - E_g)^{1/2}$ near the absorption onset [103]. Such a square-root behaviour would at best partly fit the initial steep rise around 1.64 eV leaving the following sharp transition to a flatter regime difficult to account for. On the other hand, absorption enhancements at the band edge caused by resonant exciton creation would provide a plausible explanation for an initially steeper rise of the absorption coefficient [172]. Exciton binding energies have been reported for the pure halide $CH_3NH_3PbI_3$ to range from 20 meV [89] to 37 meV [90], which is sufficiently high for enhancement effects to be observed at room temperature, given that for $T = 297$ K the characteristic thermal energy is $k_BT = 25.6$ meV. Note that reliable clarification of the nature of the absorption onset

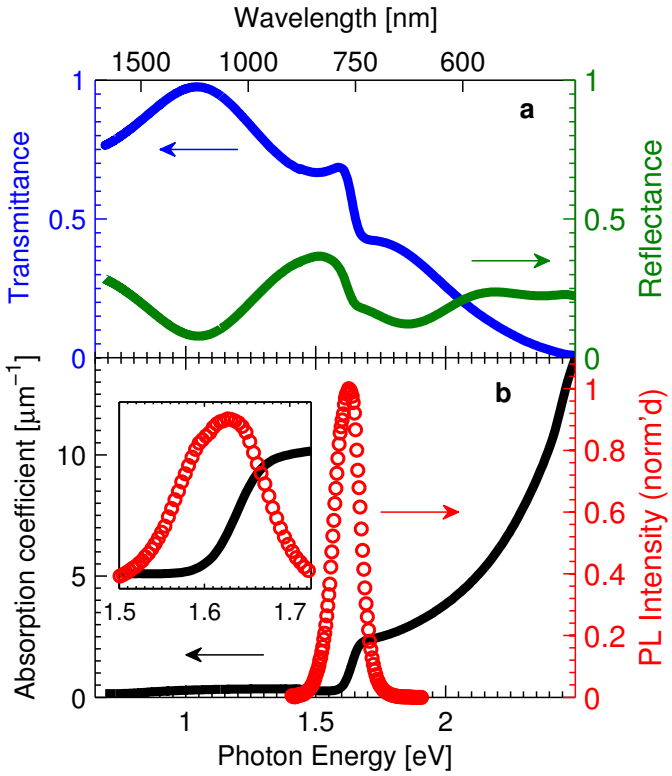

Figure 7.1: **(a)** Optical transmittance ($T_{\text{ext}} = I_{\text{transmitted}}/I_{\text{incident}}$, blue) and reflectance spectra ($R = I_{\text{reflected}}/I_{\text{incident}}$, green) of evaporated films of $CH_3NH_3PbI_{3-x}Cl_x$. T_{ext} was determined in specular transmission geometry and R in specular reflection geometry at close to normal (6°) incidence. **(b)** Black curve: absorption coefficient $\alpha = -1/d \ln(T_{\text{ext}}/(1-R))$, calculated from the data in (a) and the film's thickness $d = 330\,\text{nm}$ (black). Red circles: Photoluminescence emission spectrum at 1.96 eV excitation energy ($\lambda = 634\,\text{nm}$), 6 μJ/cm^2 fluence and 2 MHz repetition rate. Inset: magnification of the plot in the energy range around the absorption edge and PL emission.

may require in-depth theoretical modelling e.g. in conjunction with low-temperature absorption data to allow isolation of individual contributions.

7.2.2 Photoluminescence

The photoluminescence emission spectrum of vapour-deposited $CH_3NH_3PbI_{3-x}Cl_x$ is shown along with the absorption data in Figure 7.1b. The full-width-at-half-maximum (FWHM) of this spectrum is 103 meV. With its centre of mass (1.617 eV) near the low-energy tail of the absorption edge, the PL emission appears to show a slight down-shift in energy with respect to the band gap. The magnitude of any potential shift is however subject to some uncertainty due to the aforementioned ambiguities in the precise location of the band gap energy. Such Stokes shifts are commonly observed in different materials for a variety of reasons including migration of excitations to low-energy sites [173] and lattice relaxation (polaronic effects) [109, 143]. More remarkable is the apparent presence of additional broadening mechanisms resulting in the emission line width being almost twice as broad as the spectral width of the absorption onset (56 meV, determined as the FWHM of the derivative of the absorption edge).

To probe the mechanisms that underlie the broadening of the PL emission spectrum, photoluminescence spectra are recorded while scanning the excitation energy through the absorption edge and across the full range of the emission spectrum. For this experiment the Ti:Sapphire pump laser was operated in continuous wave mode to allow spectrally narrow excitation of the sample. A representative subset of the acquired spectra is shown in Figure 7.2a. Since it is experimentally impossible to fully separate scattered excitation light from the photoluminescence, the spectra also exhibit additional sharp peaks at the corresponding excitation energy. Below, in panel (b) the spectrally integrated PL emission intensity is plotted as a function of excitation energy. For this purpose, the PL intensity was normalized for excitation photon flux

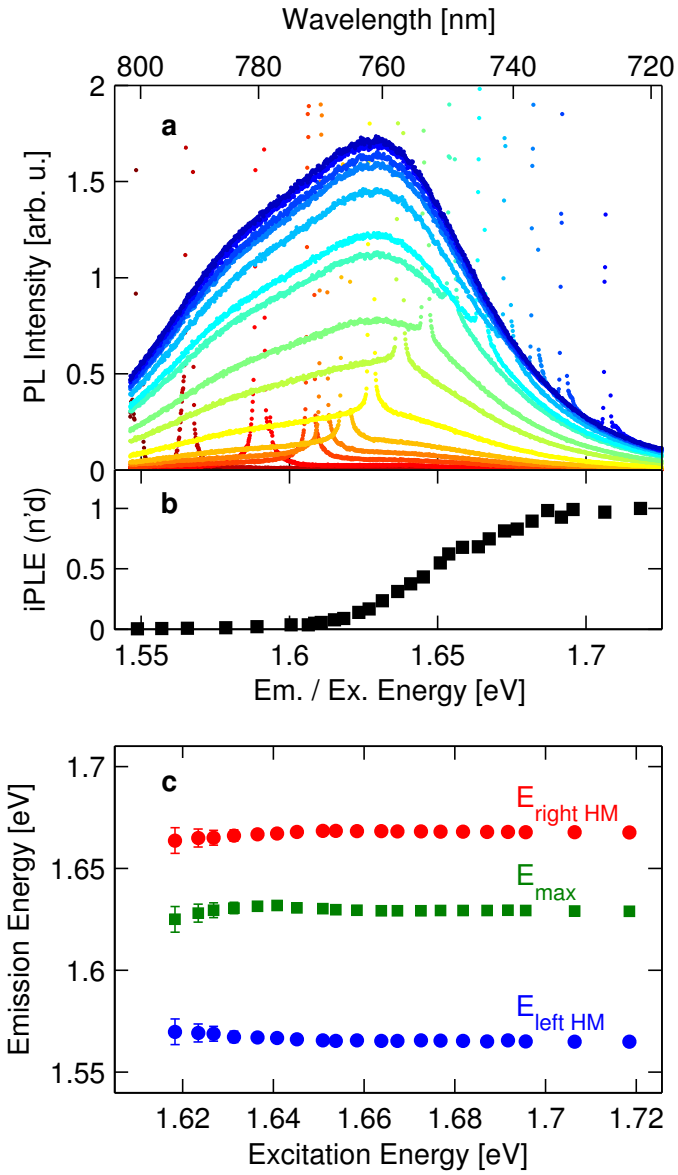

Figure 7.2: **(a)** PL emission spectra of evaporated $CH_3NH_3PbI_{3-x}Cl_x$ films on glass (PL intensity vs. emission energy), taken at excitation energies close to the absorption edge ranging from 1.55 eV (dark red) to 1.73 eV (dark blue). The excitation intensity was held constant at 5 W cm^{-2}. The narrow peaks originate from scattered excitation light and can be used as a visual indicator of the excitation energy. **(b)** Spectrally integrated PL intensity as a function of excitation energy for evaporated films $CH_3NH_3PbI_{3-x}Cl_x$ as extracted from the data shown in (a). **(c)** Energy of the PL emission maximum extracted from the data shown in (a) plotted against excitation energy (green squares). The energies at which the emission reaches half its maximum intensity are shown as red and blue circles.

and the scattered excitation light peaks removed through data interpolation.

From the excitation energy dependent PL data the striking observation can be made that the shape of the emission spectrum is identical across the entire excitation range. While this result is visually apparent from the spectra shown in Figure 7.2a, further analysis is provided by extracting the energy of maximum emission and the positions of the left and right half-maxima as a function of excitation energy in Figure 7.2b. While the uncertainty increases in the regime of weaker PL emission (as indicated by the error bars), Figure 7.2b confirms that the emission spectrum of $CH_3NH_3PbI_{3-x}Cl_x$ is independent of excitation energy across the inter-band absorption onset. It is therefore concluded that the broadening mechanism must be homogeneous, i.e. the emission at every single site is itself equally and fully broadened. If this were not the case, selective excitation within a distribution of inhomogeneous sites would generate charge-pairs only at those sites that are tuned to the particular excitation energy used. As a result, the excitation energy would be site-selective, and the emission spectra shift to reflect the local nature of the sites selected. Such site-selective emission shifts can for example be observed for thin films of disordered polymeric semiconductors exhibiting significant inhomogeneous spectral broadening [173]. In contrast, the observation of shape-persistent emission spectra for resonant excitation throughout the emission spectrum of vapour-deposited $CH_3NH_3PbI_{3-x}Cl_x$ highlights the low degree of disorder present in these thin films.

To gain further insights into the dynamics of radiative decay channels in $CH_3NH_3PbI_{3-x}Cl_x$ and the factors determining the spectral shape of the emission, time-resolved photoluminescence spectra were recorded by means of time-correlated single photon counting (TCSPC). PL decay traces were taken for a range of regularly spaced emission energies and the spectra at the desired time-delays reconstructed from the data. Figure 7.3a shows the resulting three-dimensional plot of the emission spectra at various times after pulsed excitation at 1.96 eV. Visual inspection of these data

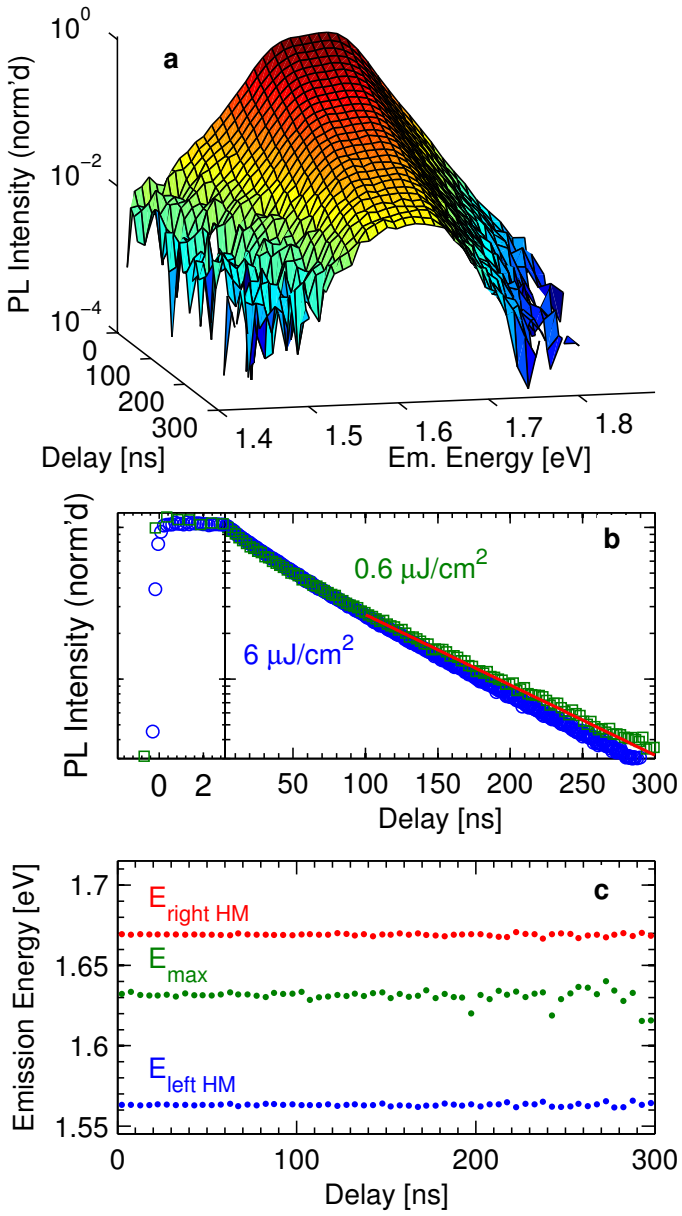

Figure 7.3: **(a)** 3D representation of the time-resolved PL emission spectrum of evaporated $CH_3NH_3PbI_{3-x}Cl_x$ acquired by means of time-correlated single photon counting at various emission energies (Excitation energy: 1.96 eV, fluence: 6 μJ/cm^2, repetition rate: 2 MHz.) **(b)** Time-resolved PL emission decay at the spectral maximum for excitation fluences of 6 μJ/cm^2 and 0.6 μJ/cm^2 acquired in the same way as the data in (a). Red line: fit of a mono-exponential decay function to the low-fluence data for the time-delay interval from 100 ns to 300 ns. The resulting decay time constant is (94.2 ± 0.9) ns with $\chi^2_r ed = 1.04$. **(c)** Photon energy at the emission maximum (green), and the energies at which the emission reaches half its maximum intensity (red and blue) as extracted from the data shown in (a), plotted against the time delay between excitation and emission.

reveals an essentially time-independent spectral shape of the PL emission. Again the energetic positions of the emission maximum and half-intensity points of each spectrum are extracted, to allow for better inspection of potential changes in the spectrum over time (see Figure 7.3c). This plot clearly confirms that the PL emission spectrum of $CH_3NH_3PbI_{3-x}Cl_x$ is time-independent for time delays between 200 ps and 200 ns. Again these results suggest an absence of significant inhomogeneous broadening arising from energetic disorder. For materials incorporating a broad distribution of energetic sites, as for example semiconducting polymer films [174, 175] porous silicon [176], or heavily doped crystalline GaAs [177], pulsed excitation of the material is usually followed by gradual emission shifts towards lower energy with time, resulting from migration to lower-energy sites in the inhomogeneous distribution. The absence of such emission energy shifts with time after excitation in $CH_3NH_3PbI_{3-x}Cl_x$ films is therefore fully compatible with the prior observation of a predominantly homogeneously broadened emission line width.

Figure 7.3b shows that the PL emission intensity from vapour-deposited $CH_3NH_3PbI_{3-x}Cl_x$ decays relatively slowly over a few 100 nanoseconds after excitation, in similarity to previous reports [87, 88] for solution-processed films of $CH_3NH_3PbI_{3-x}Cl_x$. The observed PL transients are almost fully mono-exponential and only exhibit very slightly increasing decay rates for increased excitation fluences. As previously seen in Chapter 5 for solution-processed $CH_3NH_3PbI_{3-x}Cl_x$ films, such effects arise mainly from the onset of bi-molecular charge recombination, which becomes more and more dominant as the charge-carrier density is increased. From the PL decay at low excitation fluence ($0.6\,\mu J/cm^2$) and at longer delays (> 100 ns) after excitation, a mono-molecular decay lifetime of 94 ns can be extracted by fitting a single exponential decay function to the data. It shall also be noted that while there is some fluence-dependence of the PL decay rate, the shape of the emission spectra was found to be independent of excitation fluence for values up to at least $20\,\mu J/cm^2$ (not shown). This observation again suggests an absence of disorder-related effects such as potential saturation of

low-energy states in the tail of an inhomogeneously broadened density of states that would induce spectral shifts with increasing excitation fluence.

7.2.3 Mechanisms of Spectral Broadening

For the discussion of the above findings several processes are considered that can potentially cause substantial homogeneous PL emission broadening and the observed asymmetry with the spectral broadening of the absorption edge. The simplest origin of homogeneous broadening is given by the natural line width of $\Delta E = \hbar/\tau$ caused by the finite lifetime τ of the excited state [170]. The observed asymmetry between absorption and emission broadening would in this case require at least one additional intermediate state in the recombination process with an extremely short lifetime $\leq 6.4\,\mathrm{fs}$ (corresponding to $\Delta E = 103\,\mathrm{meV}$), which is seven orders of magnitude shorter than the overall decay dynamics actually observed in time-resolved PL (Figure 7.3c). In addition, lifetime broadening would have to result in a Lorentzian emission line shape [170]; however, the observed spectra (Figure 7.2), and in particular the shape of the tails which resemble those of a Gaussian, are not consistent with a Lorentzian distribution function. It is therefore concluded that lifetime broadening is not responsible for the dominant contribution to the observed broad emission line width.

Another possible source of homogeneous broadening lies in the participation of phonons in the radiative recombination process. Figure 7.2 clearly shows that the PL emission spectra feature a superposition of at least two peaks. It appears that a possible underlying composition could consist of a band-edge emission peak and a number of side bands responsible for the shoulder at about 1.58 eV and the broad tails. PL side-bands are commonly found to arise from phonon creation or annihilation and have been observed in a whole variety of materials, ranging from inorganic semiconductors such as silicon [178] to metal halides [155, 179, 180] and organic

(molecular) semiconductors [173]. In Chapter 5 is was shown that the low-frequency photoconductivity spectra of solution-processed $CH_3NH_3PbI_{3-x}Cl_x$ and $CH_3NH_3PbI_3$ films contain the signature of metal halide lattice vibrations. It therefore seems likely that the emission from such photogenerated charge pairs is also subject to interaction with phonons. Given the large size of the crystallites for these vapour-deposited films of $CH_3NH_3PbI_{3-x}Cl_x$ (extending up to hundreds of nanometres [15]) and the absence of time-dependent spectral emission features, the phonon coupling mechanism will most likely arise directly from the intrinsic nature of the bulk material, rather then derive from surface mediated effects.

In the picture of electronic band structure, processes involving phonon creation or annihilation simultaneous to the emission of the photon are of particular importance in indirect gap semiconductors where a third particle is needed during electron-hole recombination to accept the momentum difference between conduction band minimum (CBM) and valence band maximum (VBM). Luminescence from indirect semiconductors hence often exhibits a broadened spectrum as e.g. observed in crystalline silicon [178]. Band structure calculations have so far postulated a direct band gap for the methylammonium lead halides $CH_3NH_3PbI_3$ [75, 76, 77, 78], $CH_3NH_3PbCl_3$ [77] and $CH_3NH_3PbI_{3-x}Cl_x$ [77]. Similar recombination dynamics to those in indirect semiconductors could however also arise from the existence of a second conduction band valley that is only separated from the main (Γ-) valley by a low energy barrier allowing rapid equilibration of their populations. The low bi-molecular decay rates and the observation of Auger processes in $CH_3NH_3PbI_{3-x}Cl_x$ (see Chapter 6) suggest that recombination via the direct transition is in some way inhibited, which leaves the possibility for an additional indirect transition to become a dominant recombination pathway. It must be noted that the likelihood of this scenario to apply in the present case is reduced by the fact that calculations of the electronic band structure of $CH_3NH_3PbI_{3-x}Cl_x$ have so far not indicated the presence of a second valley [77].

As an alternative concept, the observed broadening may be attributed to polaronic effects, similar to those observed in molecular semiconductors [181, 182] or metal halides [155]. Here, the photo-generated electron-hole pair strongly couples to the underlying lattice, which leads to a geometric lattice relaxation around the created charge. As a result, the emission is found to be Stokes-shifted from the absorption edge and likely contains phonon features. For materials with strongly ionic bonding and hence strong exciton-phonon interaction, Coulomb-correlated electron-hole pairs have therefore also been referred to as *self-trapped excitons* [155]. Such phenomena have been evoked in alkali halides [183], transition metal halides [180] and also certain perovskites [184, 185]. They are therefore likely to also play a role in the related compounds here. Note that for metal halides, the barrier to self-trapping was found to be generally low and the process appeared to occur on ultrashort (sub-picosecond) timescales related to the involved lattice vibration periods [155]. A signature of self-trapping dynamics would therefore not necessarily be expected to appear in the time-resolved PL spectra shown in Figure 7.3a, as these were taken with much lower time-resolution. Earlier work on alkali halides often revealed significant Stokes shifts between absorption and emission [155]. For the $CH_3NH_3PbI_{3-x}Cl_x$ films under investigation here, the lack of an unambiguous physical decomposition of the broad absorption and emission features prevent the extraction of an exact Stokes shift. However, by visual inspection of Figure 7.1b it is clear that possible values could at most be of the order of 30 meV. This suggests that any polaronic effects in this system are comparatively low, in agreement with the high charge-carrier mobilities found in Chapter 6 and long diffusion lengths recently reported for solution-processed methylammonium lead halide perovskite films [87, 88]. Hence while polaronic effects may be present in these materials, they appear to be sufficiently low to still allow excellent charge extraction and high open-circuit voltages in planar-heterojunction photovoltaic device architectures [15].

The observation of a strongly homogeneously broadened emission line shape has two

implications for device applications. First, the absence of spectral shifts resulting e.g. from site-selective excitation or excitation migration in these materials suggests that disorder and trapping is scarce, at least for the dominant bulk-like emissive species. This finding again highlights the suitability of these materials for photovoltaic applications, for which material disorder in systems such as organic semiconductors, mesoporous metal oxides and amorphous silicon, has been shown to correlate with a reduction in photovoltage [186]. The presence of disorder or traps near the surfaces of the perovskite cannot be ruled out, as these contribute little to the overall emission in terms of volume fraction. However, surface states are also highly accessible to passivation treatments [53, 187] that can be more easily applied here than throughout the bulk structure. Second, materials with broad homogeneous emission line shapes fulfil a central requirement for gain media in femtosecond lasers due to the high natural bandwidth of ultrashort pulses (103 meV at 6.4 fs). Organolead halide perovskites already show many of the required properties for lasing operation, such as strong emission and a sufficiently long-lived upper state. The potential for electrical injection due to the good charge conductivity of the material may create a crucial advantage over existing gain media enabling more compact and efficient laser systems than those relying on optical pumping.

7.3 Conclusion

The origin of spectral broadening in the emission of vapour-deposited $CH_3NH_3PbI_{3-x}Cl_x$ was investigated. By recording PL spectra while continuously tuning the excitation energy across the spectral range of the emission peak it is revealed that no observable selective excitation occurs of sub-sites in resonance with the respective energy. It is hence established that the broadening mechanism is homogeneous with an associated width of 103 meV. It is furthermore shown that the PL emission spectrum does not exhibit a dependence on time after excitation or excitation fluence,

suggesting a high degree of order present in the film. The slightly Stokes-shifted and homogeneously broadened PL spectra exhibit features consistent with phonon coupling as the dominant spectral broadening mechanism of the emission from $CH_3NH_3PbI_{3-x}Cl_x$. The findings in this chapter underline the potential of organometal halide perovskites for a wider range of optoelectronic applications beyond photovoltaic energy conversion. In particular, the observed broad homogeneous line width ought to allow amplification of Fourier-transform limited pulses with sub-100 fs duration, making these materials interesting for pulsed laser operation.

8

Charge-Carrier Recombination Channels in the Low-Temperature Phase of $CH_3NH_3PbI_{3-x}Cl_x$ Thin Films

During the past two years, remarkable progress has been made in revealing what enables organo-lead halide perovskites to deliver their impressive power conversion efficiencies in solar cells. In order to substantiate the understanding of the underlying photophysics, studies with a scope beyond the conditions defined by a particular application can provide essential further contributions and help verify theoretical predictions from structural and band-structural calculations, which have recently been undertaken by several groups [77, 78, 85, 188, 189, 190, 191]. Valuable insights can often be gained by isolating the influence of thermal excitation and broadening mechanisms in the system through temperature-dependent studies. Given that reported exciton binding energies in $CH_3NH_3PbI_3$ and $CH_3NH_3PbI_{3-x}Cl_x$ are close to the characteristic thermal energy at room temperature ($k_BT \approx 25\,\mathrm{meV}$) [89, 90, 91], low-temperature measurements may shed more light on the role of excitonic states in carrier recombination processes. Furthermore, it was shown in the previous chapters that phonon-interactions have a significant impact on the luminescence and charge transport properties of these perovskites.

To date the results of several temperature-dependent studies on bulk $CH_3NH_3PbI_3$ have been published, which provide important information on structural phase transitions in the material. At temperatures above ∼330 K the compound adopts the simple cubic perovskite structure (space group $Pm\overline{3}m$) [192], although a very small ferroelectric-type displacement of the lead-cation has been observed [82], which - strictly speaking - creates a tetragonal unit cell (space group P4mm). The transition to the room-temperature phase involves a collective rotation of the PbI_6-octahedra around the c-axis [193, 194], which is well-known from many inorganic perovskites and which leads to closer packing within the *ab*-plane. The resulting unit cell is tetragonal with space group I4cm and has doubled in volume with respect to the cubic unit cell [193, 194].

A further transition to an orthorhombic phase is observed at 160 K [193, 195]. This transition is accompanied by a tilting of the PbI_6-octahedra out of the *ab*-plane and a corresponding further doubling of the unit cell volume (space group Pnma) [195]. An analysis of the symmetries of the tetragonal and the orthorhombic shows that a continuous transition between the two space groups is not possible. Therefore, a transient intermediate phase has been postulated, but not yet been resolved [195]. The behaviour of the A-cation $CH_3NH_3^+$, which, other than in purely inorganic perovskites, possesses several rotational degrees of freedom in the high-temperature phase, has been investigated by means of NMR- spectroscopy [196] as well as IR-vibrational spectroscopy [197], calorimetry [197] and dielectric measurements [165, 193]. It was found that the cubic symmetry of the high-temperature phase is effectively preserved through rapid random reorientations of the $CH_3NH_3^+$-cation. From its 24 possible orientations, 8 remain in the tetragonal phase. Eventually, in the orthorhombic phase, all degrees of freedom are frozen [196, 197].

Information on optical and electronic properties of $CH_3NH_3PbI_3$ at low temperature is very scarce. Apart from the aforementioned dielectric studies reflecting the behaviour

of the $CH_3NH_3^+$-cation, some data is available on resistivity showing a decrease with increasing temperature as is typical for undoped semiconductors [82]. Very recently, *DInnocenzo et al.* conducted a study of the excitonic properties of the mixed halide perovskite $CH_3NH_3PbI_{3-x}Cl_x$ for which temperature-dependent optical absorption data has been acquired [91]. The focus of the report however mainly lies on the behaviour of the material within the tetragonal (room-temperature) phase. PL and diffuse reflectance spectra at low-temperature were also recently acquired by *Yamada et al.* on the pure triiodide $CH_3NH_3PbI_3$ as infiltrated into mesoporous TiO_2 [198]. In this chapter, a study of the optical absorption and luminescence properties of $CH_3NH_3PbI_{3-x}Cl_x$ is presented, scrutinizing the temperature-dependent evolution of recombination pathways in this system.

8.1 Experimental Details

Compact films of about 330 nm thickness were prepared by dual-source evaporation on glass as described in detail in 6.1.1. Photoluminescence measurements were performed on the experimental setup based on a tunable Ti:Sapphire laser described in 3.2.3. Samples were mounted in a liquid-helium cryostat (Oxford Instruments Microstat), where they remain under vacuum ($p < 10^{-5}$ mbar). Optical absorption spectra were acquired in the same experimental setup through the same collection optics as the PL spectra. A 100 W incandescent lamp was used as a light source.

8.2 Results and Discussion

8.2.1 Optical Absorption

First the optical absorption spectra acquired across the temperature range from 4.2 K to 297 K are discussed. It has been shown previously that a shift of the absorption edge in energy at about 140 K can be identified in films of $CH_3NH_3PbI_{3-x}Cl_x$ (and at about

170 K in $CH_3NH_3PbI_3$) [91]. This shift very likely reflects the same orthorhombic-to-tetragonal phase transition as occurs in the pure halide perovskite $CH_3NH_3PbI_3$, for which an increase in bandgap energy has also been predicted computationally [189, 195]. In Figure 8.1, the electronic band structure diagrams obtained by *Baikie et al.* using density functional theory (DFT) [195] are reproduced showing the direct bandgap of the material at the Γ-point in both phases with a slight down-shift of the valence band maximum as the symmetry of the Brillouin zone is lowered during the phase transition.

The optical absorption data recorded in this study are displayed in Figure 8.2a. It shows the expected leap of the onset from ∼1.7 eV to ∼1.6 eV between 120 K and 140 K, superimposed on a continuous shift towards higher energy with increasing temperature. The latter represents an unusual behaviour of the perovskite when compared to most direct semiconductors, which was recently reproduced in band-structure calculations [189]. At low temperature the absorption edge is relatively steep and exhibits an overshoot-feature which is most probably to be attributed to resonant formation of excitons [172]. This feature becomes less pronounced towards high temperature along with a continuous broadening of the absorption onset.

In order to locate the orthorhombic-to-tetragonal phase transition more precisely,

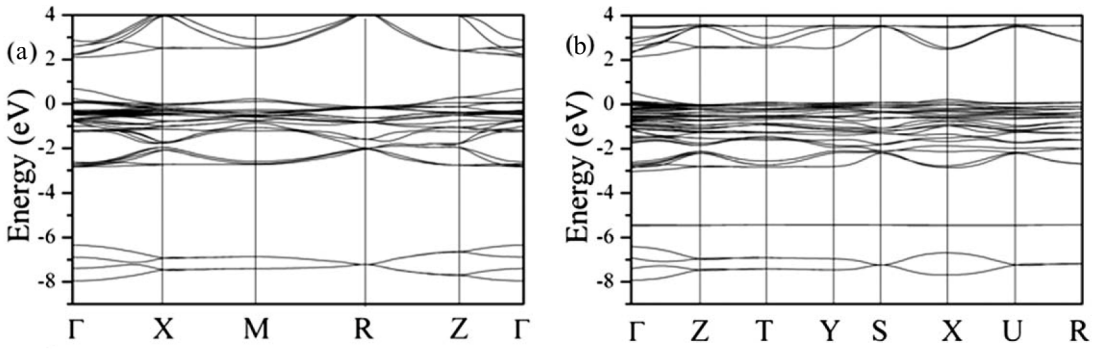

Figure 8.1: Calculated band structures (based on density functional theory) of the (a) tetragonal and (b) orthorhombic phase of $CH_3NH_3PbI_3$. Reprinted with permission from [195]. Copyright (2013) The Royal Society of Chemistry.

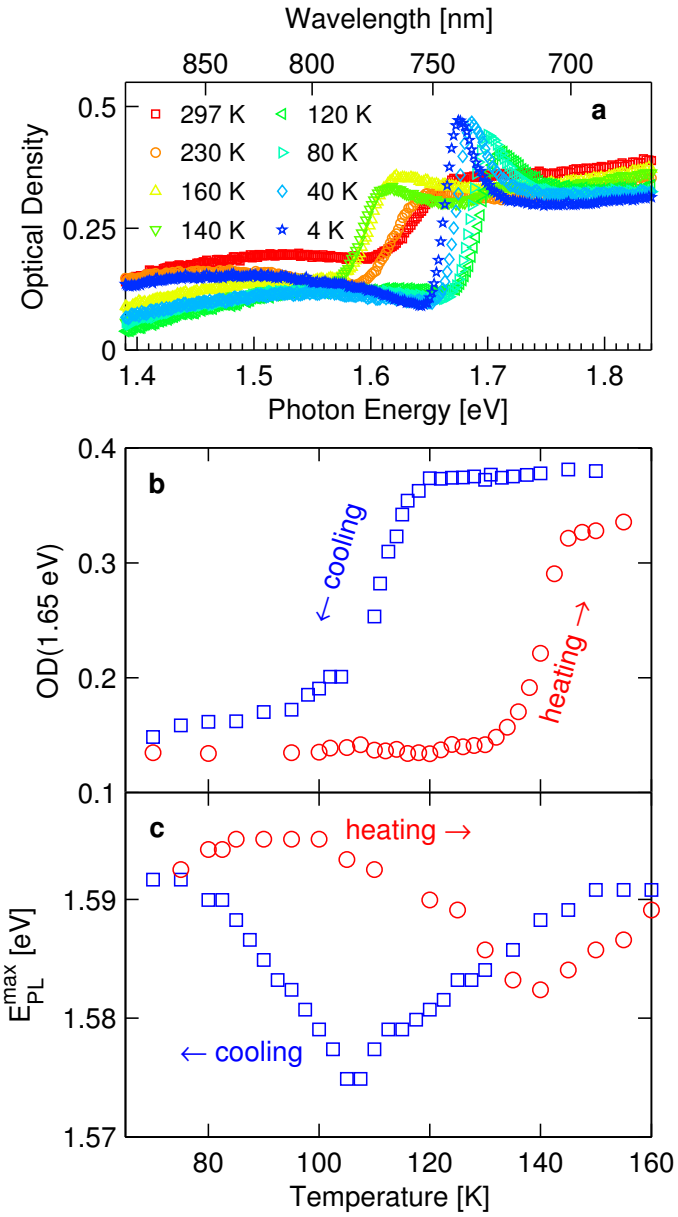

Figure 8.2: **(a)** Optical absorbance spectra of $CH_3NH_3PbI_{3-x}Cl_x$ recorded at temperatures between 4 K and 297 K. **(b)** Optical density at 1.65 eV photon energy recorded while cooling the sample from 160 K to 40 K (blue squares) at -6 K min^{-1} and while subsequently heating the sample from 40 K to 160 K at 6 K min^{-1} (red circles). **(c)** Photon energy of maximum PL emission vs temperature (ignoring the higher-energy peak emerging in the low-temperature phase) at excitation fluence 50 nJ/cm^2 during an identical cooling and heating cycle as in (b).

the temperature range around 140 K is scanned with higher resolution. As shown in Figure 8.2b, where the optical density at 1.65 eV is plotted against temperature as an indicator of the completeness of the phase transition, strong hysteretic behaviour is found with an about 40 K lower transition when cooling as compared to when heating the sample. Note that even stronger hysteresis is observed when performing an even slower cooling- and heating-cycle (not shown). Previous studies have not come to unique results on this point. While dielectric measurements of $CH_3NH_3PbI_3$ crystals only reveal a hysteresis of a few kelvin [165], resistivity measurements also on crystals exhibit a span of about 30 K between the corresponding features in the heating and the cooling cycle [82].

8.2.2 Photoluminescence Spectra

Photoluminescence (PL) emission was recorded in identical cooling- and heating cycles as performed for optical absorption measurements. Figure 8.3 shows a series of temperature-dependent PL spectra at two different excitation fluences. The features of room-temperature emission were discussed in Chapter 7. There, the relatively large spectral width and the structure of the peak was attributed to a homogeneous broadening mechanism arising from phonon coupling effects. Within the tetragonal phase the shape of the peak remains essentially unchanged between 140 K and 297 K, however the overall spectral width decreases with temperature consistent with a smaller available phonon population. The shape of the PL emission is also found to be independent of excitation fluence in this phase ruling out contributions of defect broadening. Such contributions would be expected to show either saturation effects or decrease in their relative strength when entering the regime of bi-molecular recombination processes at stronger excitation.

Interestingly, at temperatures below the phase transition and under high-fluence excitation, emission centred around the same energy as in the high-temperature phase

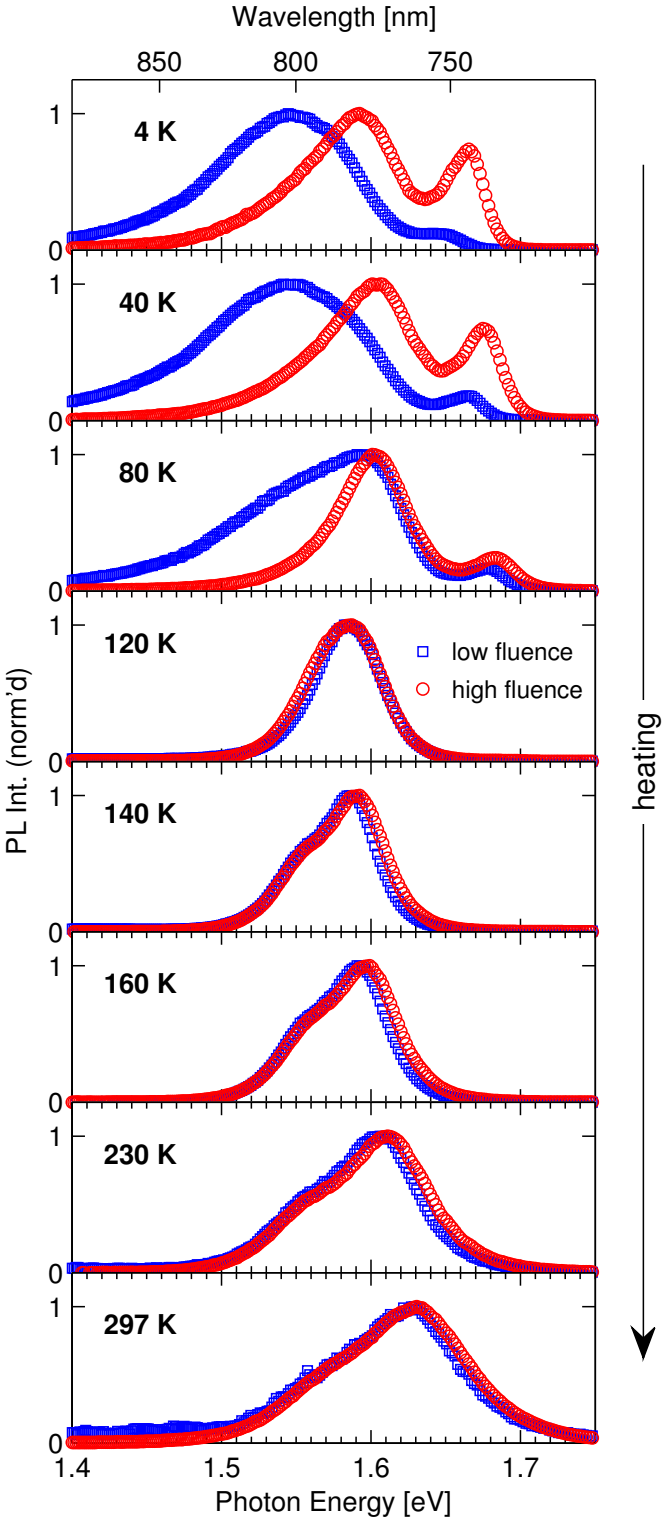

Figure 8.3: Photoluminescence spectra of $CH_3NH_3PbI_{3-x}Cl_x$ at temperatures between 4 K and 297 K taken at excitation fluences 5 µJ/cm^2 and 50 nJ/cm^2. Spectra were taken in a single temperature sweep from 4 K to 297 K.

is continued to be observed. This is surprising given the increase in bandgap energy by 0.1 eV seen in the optical absorption data. In Figure 8.2c, the transition regime is inspected more closely by plotting the position of the emission maximum against temperature. A feature consisting in a sharp reversal of the continuous drift of the PL peak is identified. For both, the heating and the cooling cycle, this feature coincides with the spontaneous shift of the absorption edge (Figure 8.2b). The fact that no spontaneous shift of the PL peak is observed, suggest that emission still originates from the same intraband transition on both sides of the structural phase transition. Towards lower temperatures, a second, small, higher-energy emission peak appears gradually, which is located close to the corresponding absorption onset. Note that the spectral width of this peak does not decrease with temperature and substantial broadening is still effective even at 4 K. This observation is consistent with the polaronic mechanism suggested for the homogeneous spectral broadening at room temperature, which has been shown to characteristically lead to a remaining finite line width, even at very low temperatures [155, 180]. Overall, the PL emission spectrum becomes strongly dependent on excitation fluence below the phase transition. While at low excitation fluence the higher-energy peak almost disappears, the lower-energy peak significantly broadens and drops to even lower energy.

As an explanation for the observed emission behaviour in the low-temperature phase the possibility of small inclusions of crystallites adopting the high-temperature tetragonal phase is considered. Coexisting crystallographic phases have been observed in several inorganic perovskite materials of mixed [199, 200, 201] and pure [202, 203, 204] composition. For the latter case it has been shown that the secondary phase can be stabilized through the effect of strain imposed on a thin film by the substrate [202, 203] or through external pressure [204]. Despite the fact that $CH_3NH_3PbI_{3-x}Cl_x$-films studied here were grown on an amorphous glass substrate, and hence any lattice-mismatch of the as-grown sample is ruled out, unequal thermal expansion and, more importantly, the spontaneous change of the in-plane lattice constants during the

phase-transition [195] may well cause a significant amount of strain to the film.

Tetragonal inclusions in the orthorhombic phase of $CH_3NH_3PbI_{3-x}Cl_x$ can potentially trap photoexcited carriers due a possibly lower-lying conduction band in this phase (as suggested by the 0.1 eV lower gap). Thus, a large density of carriers would agglomerate and eventually recombine within these inclusions. This scenario straightforwardly rationalizes the fluence-dependent emission spectra. Under strong excitation, the carrier density in tetragonal crystallites saturates, such that a significant number of carriers remains in the orthorhombic phase, hence causing substantial emission at the correspondingly higher energy. In contrast, under weak excitation, the low number of initially free carriers can just partially fill the sub-gap distribution of states in the tetragonal crystallites. A high density of sub-gap states located at the phase boundaries is plausible, if individual crystallites are assumed to be very small. As a consequence a broadened and down-shifted emission is observed from these carriers.

In order to verify the proposed physical mechanism for the emission characteristics in the low-temperature phase of the $CH_3NH_3PbI_{3-x}Cl_x$ film, excitation-energy dependent PL spectra were recorded. In Figure 8.4a the spectrally integrated emission is plotted against excitation energy at 40 K. From comparison of emission and excitation spectrum it becomes clear that, although the strongest emission is observed at about 1.6 eV, i.e. corresponding to the bandgap of the tetragonal phase, measurable excitation through this transition does not appear to be possible. In fact photoexcitation seems to occur exclusively through the higher-energy transition at 1.7 eV corresponding to the bandgap of the orthorhombic phase. This suggests that the relative volume fraction of low-energy sites is very small, while at the same time these sites provide the dominant radiative recombination route.

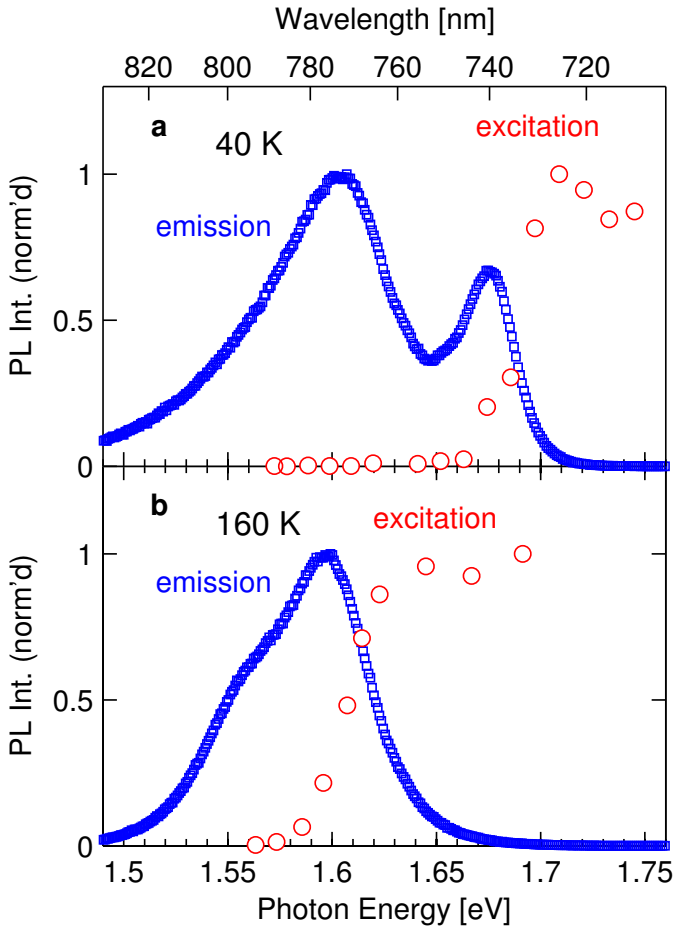

Figure 8.4: Normalized photoluminescence excitation spectra (red circles), i.e. spectrally integrated PL emission as a function of excitation energy, at **(a)** 40 K and **(b)** 160 K, recorded under continuous wave excitation at an intensity of 5 W cm^2. To provide sensible reference points, normalized PL emission spectra as displayed in Figure 8.2 (fluence 5 µJ/cm^2) are added to the plot (blue circles).

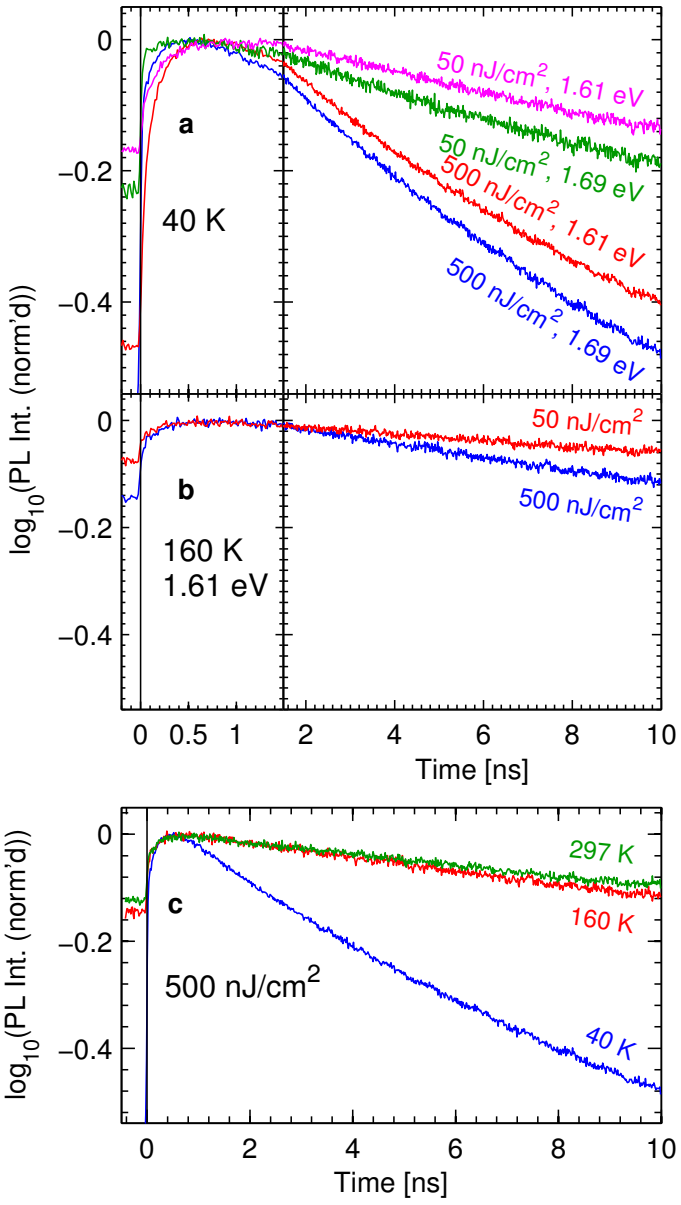

Figure 8.5: Time-resolve photoluminescence emission recorded by means of time-correlated single photon counting at various temperatures, excitation fluences and emission energies: **(a)** T = 40 K. Traces were recorded at both spectral emission maxima. Labels on curves show excitation fluence and detected energy. **(b)** T = 160 K. Traces were recorded at the spectral emission maximum. Labels on curves show the excitation fluence. **(c)** Comparison of time-resolved PL at 4 K, 160 K and 297 K at excitation fluence 500 nJ/cm^2. Traces were recorded at the (higher energy) spectral emission maximum. Excitation energy in all panels: 2.43 eV.

8.2.3 Time-Resolved Photoluminescence

Further insight into the recombination pathways in the orthorhombic and tetragonal phases of $CH_3NH_3PbI_{3-x}Cl_x$ films can be gained from studying their dynamics through time-resolved PL measurements. PL decay traces were recorded by means of time-correlated single photon counting below and above the phase transition. Figure 8.5a shows time-dependent PL at 40 K under two different excitation fluences at the maxima of both emission peaks. First, it can be observed that decay lifetimes as compared between the two emission energies (1.61 eV and 1.69 eV) at the same excitation fluence are very similar. Focussing on the signal rise it can furthermore be seen that the low-energy emission builds up with about one nanosecond delay with respect to the emission at higher-energy. These observations support the proposed scenario of excited carriers largely transferring to low-energy sites (i.e. small tetragonal crystallites) before recombining there. As a consequence of the charge-carrier migration being much faster than their recombination, the decay of both populations, in the orthorhombic host-phase and the tetragonal inclusions, is predominantly governed by the (faster) recombination process within the inclusions.

It is found that the decay lifetime of photoexcited carriers in the $CH_3NH_3PbI_{3-x}Cl_x$-film depends significantly on excitation fluence, with the decay becoming faster for higher carrier density. This is a signature of a bi-molecular recombination component. In contrast only a negligible excitation fluence dependence of the PL decay is observed above the phase transition (see Figure 8.5b). The latter agrees well with room temperature studies, which show that within the range of excitation densities used ($\sim 5 \times 10^{15}\,\mathrm{cm}^{-3}$ for $50\,\mathrm{nJ/cm}^2$), carrier decay is dominantly governed by monomolecular processes, since, as revealed in Chapter 6 the bi-molecular rate constant is very small in the material. This does however not imply that the tetragonal-to-orthorhombic phase transition involves a dramatic increase of the bi-molecular rate constant, since it can already be accounted for by the assumed carrier migration to

small tetragonal phase inclusions. Because the effective carrier density within these would be much higher than in a homogeneous distribution upon photoexcitation, a substantial rise of bi-molecular contributions is expected even if the intrinsic rate constant does not change. This observation also explains the overall faster carrier decay in the low-temperature phase indicated by Figure 8.5c, which directly compares PL transients at 40, 160 and 297 K.

8.3 Conclusion

In summary, the temperature dependent optical absorption and photoluminescence emission was investigated from thin $CH_3NH_3PbI_{3-x}Cl_x$-films grown by thermal dual-source evaporation. A broad phase transition exhibiting strong temperature hysteresis has been located in the range between 100 K and 140 K. During this transition, which can very probably be identified with the well-established tetragonal-to-orthorhombic phase-transition in the pure triiodide $CH_3NH_3PbI_3$, the absorption edge shifts upwards in photon energy from about 1.6 eV to 1.7 eV. In the room-temperature (tetragonal) phase the PL emission spectrum consists of a single broad peak in the vicinity of the absorption edge. This peak continues to exist below the phase transition while a second, smaller peak gradually emerges close to the absorption edge of the low-temperature (orthorhombic) phase. The spectral width of this peak remains constant under further cooling, consistent with polaronic broadening mechanisms as previously proposed to account for the large homogeneous emission line width at room temperature. The observation that, even below the phase transition, PL is dominantly emitted near the bandgap energy of the room-temperature phase may be explained by the presence of small inclusions of the tetragonal crystal structure, in which a large fraction of photoexcited carriers agglomerate. Excitation-energy-dependent PL data shows that any possible absorption from such inclusions does at most contribute a negligible amount to carrier generation and therefore indicates that

their total volume-fraction in the film is very small. Time-resolved PL measurements were performed and a clear signature of carrier migration to lower-energy sites was observed. Very similar lifetimes were found for higher- and lower-energy emission indicating that the decay of the photoexcited carrier population is predominantly governed by recombination within the tetragonal crystallites. These lifetimes are, in comparison to those measured above the phase transition, considerably shorter and notably fluence-dependent. This can be explained by the strongly increased carrier density within the inclusions giving rise to significant bi-molecular recombination and hence does not imply intrinsically higher decay rate constants in the orthorhombic phase. These findings further the understanding of how structural phase transitions in thin films of organometal halide perovskites influence their film morphology and in turn their optoelectronic properties.

Outlook

To conclude this thesis, a brief perspective on the significance of the main results and desirable further developments in the concerned fields shall be given.

TiO_2 Nanotubes

The discovery of fast shallow trapping in TiO_2 nanotubes described in Chapter 4 constitutes an important step in understanding the limiting factors for electron-transport in this nanomaterial. Although it may have to be expected that the dye-sensitized solar cell will loose much of the research focus it has enjoyed during the last two decades to perovskite-based devices, the range of possible applications for TiO_2-nanotubes will not collapse to zero. First, it is noted that one of the major designs of perovskite solar cells equally relies on a nanostructured TiO_2 anode (see [13, 16] and Section 2.2). Although the author is not aware of any reports of perovskite devices employing TiO_2 nanotubes so far, the material holds some benefits which may make it worth being considered as an alternative to nanoparticle matrices in the function of the nanostructured semiconducting scaffold. First, with the anodization-method a very simple and well-established route exists for large-scale fabrication [59, 63]. Second, the reproducibility and production yield may be enhanced as a result of the predictable, ordered morphology of the tubes.

At the same time, owing to the semiconducting properties of the employed hybrid perovskites, the restriction to monolayer coverage of the nanotubes by the sensitizer

is lifted. Hence the original drawback of a reduced specific surface area and a consequently higher required active layer thickness in TiO_2-nanotube-DSSCs compared to those based on nanoparticles does not persist.

Outside the field of photovoltaic energy conversion, it is noted that TiO_2 nanotubes also play an important role for photocatalysis- [205, 206] as well as sensing-applications [207, 208].

Although first steps in understanding the cause of inhibited electron-transport have been made, a clear route to alleviating the trapping-phenomenon is still to be found. In Chapter 4 evidence was obtained that impurities introduced from the electrolyte during the anodization process (e.g. fluorine) may be the origin of the observed shallow trap states. With optical-pump-THz-probe spectroscopy as a straightforward tool to probe the prevalence of charge-carrier trapping, a follow-up study on sets of TiO_2-nanotube films prepared in different electrolytes may reveal a strategy to reduce the density of impurities in the material or to replace potential contaminants with those not inducing transport-limiting trap-states.

Organic-Inorganic Perovskites

The work on organic-inorganic perovskites presented in this thesis was conducted in a somewhat different context to the work on TiO_2 nanotubes despite targeting very similar questions concerning a very similar application. While TiO_2 can certainly be referred to as a well-studied functional material with a large amount of literature available on its electronic properties [122, 209], the field of hybrid perovskites is still in its infancy. Research efforts have only recently started to concentrate on a few, most application-relevant compounds within this very diverse material class. These are primarily the pure and mixed methylammonium lead halides $CH_3NH_3PbI_3$ and $CH_3NH_3PbI_{3-x}Cl_x$ [8, 9, 10, 210] but ongoing investigations should be mentioned into the possibilities of replacing the toxic element lead by tin [211, 212] or the organic

cation with one of different size creating a material with an even more favourable bandgap for solar cell applications [83, 213]. Due to the early state of knowledge in the field, the spectroscopy studies here were aimed at establishing the very basic charge transport and recombination behaviour of the materials. Approaches to interpreting observed phenomena did not rarely raise several new questions for every one question answered.

In Chapters 5 and 6 results on central optoelectronic properties which govern photovoltaic device operation and have direct impact on device performance were presented. These include charge-carrier mobilities, decay dynamics, and diffusion lengths. It was found that due to surprisingly low bi-molecular recombination rates in the materials, the decay of the free carrier population under solar cell operating conditions is only substantially driven by (presumably trap-mediated) mono-molecular processes, which also turn out to be slow. In combination with the comparatively high carrier mobilities within the realm of solution-processable materials, charge-carrier diffusion lengths of up to several micrometers were shown to be achieved. Such long diffusion lengths mark a milestone in the development of low-cost thin-film solar cells. Device architectures based on simple planar heterojunction suddenly become feasible eliminating the need to employ nanostructured materials.

The determined values for the decay rate constants now bring up extremely interesting and important questions about the underlying physics responsible for the slow recombination dynamics. It has been discussed in Chapters 5 and 6 that a huge gap of more than four orders of magnitude exists between the theoretical prediction by the Langevin model and the actually observed bi-molecular rate constants. It was suggested that a mechanism separating electron- and holes either in position- or momentum-space must be in force to explain this discrepancy. In recent publications, possible scenarios have been investigated in which a ferroelectric polarization consistent with the observed weak inversion-symmetry breaking in the perovskite CH_3NH_3-

PbI_3 [82] may have the suspected, favourable effect on charge separation [189, 214]. Another heavily debated issue revolves around the function and stoichiometry of chlorine in the mixed halide perovskite $CH_3NH_3PbI_{3-x}Cl_x$. Studies published to date have found that the actual chlorine content in this compound seems to be very low ($x \ll 1$) [77, 85] supported by the observation of a very similar bandgap energy to that of $CH_3NH_3PbI_3$. In this work and also in [87] it was however clearly shown that charge-carrier lifetimes are strongly enhanced in the mixed halide as compared to the pure triiodide. By means of electron-beam-induced current measurements, *Edri et al.* have obtained evidence that differences in charge-collection efficiency primarily originate at crystallite boundaries which were found to be a much greater barrier to charge transport in the pure than in the mixed halide perovskite [215].

These and other aspects of hybrid perovskites relating to the physical origin of their superb performance in low-cost solar cells can be expected to be subject to a great amount of studies in the near future. Given the various degrees of freedom in tuning the properties of organic-inorganic metal halides, an overarching physical picture of the photophysical processes would hold great promise for a continuation of the currently ongoing continuous efficiency improvements of perovskite solar cells [3].

Chapters 7 and 8 primarily revealed insights into phenomena with less direct impact on solar-cell operation, but certainly of general material-scientific interest and possible relevance to other applications. Carrier-phonon-coupling with notable influence on photoconductivity and luminescence properties has been observed. A homogeneous broadening of PL emission was established in $CH_3NH_3PbI_{3-x}Cl_x$ and ascribed to these coupling effects. Temperature dependent measurements have brought early results for the structural phase-transition behaviour of the material and a possibly strain-induced coexistence of two phases at low temperature.

The consideration of potential applications of hybrid perovskites beyond photovoltaics is particularly important as the universally favourable properties of the materials may

well prove to be useful in a broader variety of optoelectronic devices, such as e.g. pulsed lasers [216, 217]. It is moreover desirable for the development of the field that the next years also see a significant, further broadening of fundamental research activity on organic-inorganic metal halides expanding beyond the scope of any device applications.

Bibliography

[1] Ohl, R. S.: Light-sensitive electric device. US Patent 2,402,622 (27th May 1941).

[2] Ohl, R. S.: Light-sensitive device including silicon. US Patent 2,443,542 (27th May 1941).

[3] National Renewable Energy Laboratory: Best research cell efficiencies (2014). http://www.nrel.gov/ncpv/images/efficiency_chart.jpg.

[4] European Photovoltaic Industry Association: Market report 2013. (March 2014). http://www.epia.org/news/publications/.

[5] MacKay, D. J.: Sustainable Energy - Without the Hot Air (UIT Cambridge, 2009).

[6] Green, M. A.: Third generation photovoltaics: Solar cells for 2020 and beyond. *Physica E* **14**, 65 – 70 (2002).

[7] Hagfeldt, A., Boschloo, G., Sun, L., Kloo, L. & Pettersson, H.: Dye-sensitized solar cells. *Chem. Rev.* **110**, 6595–6663 (2010).

[8] Park, N.-G.: Organometal perovskite light absorbers toward a 20% efficiency low-cost solid-state mesoscopic solar cell. *J. Phys. Chem. Lett.* **4**, 2423–2429 (2013).

[9] Snaith, H. J.: Perovskites: The emergence of a new era for low-cost, high-efficiency solar cells. *J. Phys. Chem. Lett.* **4**, 3623–3630 (2013).

[10] Kim, H. S., Im, S. H. & Park, N.-G.: Organolead halide perovskite: New horizons in solar cell research. *J. Phys. Chem. C* **118**, 5615–5625 (2014).

[11] O'Regan, B. & Grätzel, M.: A low-cost, high-efficiency solar-cell based on dye-sensitized colloidal TiO_2 films. *Nature* **353**, 737 (1991).

[12] Kojima, A., Teshima, K., Miyasaka, T. & Shirai, Y.: Novel photoelectrochemical cell with mesoscopic electrodes sensitized by lead-halide compounds (2). In *ECS Meeting Abstracts: 210th ECS Meeting*, MA2006-02, 397 (Cancun, Mexico, 2006).

[13] Kim, H.-S., Lee, C.-R., Im, J.-H., Lee, K.-B., Moehl, T., Marchioro, A., Moon, S.-J., Humphry-Baker, R., Yum, J.-H., Moser, J. E., Grätzel, M. & Park, N.-G.: Lead iodide perovskite sensitized all-solid-state submicron thin film mesoscopic solar cell with efficiency exceeding 9%. *Sci. Rep.* **2**, 591 (2012).

[14] Lee, M. M., Teuscher, J., Miyasaka, T., Murakami, T. N. & Snaith, H. J.: Efficient hybrid solar cells based on meso-superstructured organometal halide perovskites. *Science* **338**, 643–647 (2012).

[15] Liu, M., Johnston, M. B. & Snaith, H. J.: Efficient planar heterojunction perovskite solar cells by vapour deposition. *Nature* **501**, 395–398 (2013).

[16] Burschka, J., Pellet, N., Moon, S.-J., Humphry-Baker, R., Gao, P., Nazeeruddin, M. K. & Grätzel, M.: Sequential deposition as a route to high-performance perovskite-sensitized solar cells. *Nature* **499**, 316–319 (2013).

[17] Green, M. A., Emery, K., Hishikawa, Y., Warta, W. & Dunlop, E. D.: Solar cell efficiency tables (version 43). *Prog. Photovolt.: Res. Appl.* **22**, 1–9 (2014).

[18] Shockley, W. & Queisser, H. J.: Detailed balance limit of efficiency of p-n junction solar cells. *J. Appl. Phys.* **32**, 510–519 (1961).

[19] Drr, M., Bamedi, A., Yasuda, A. & Nelles, G.: Tandem dye-sensitized solar cell for improved power conversion efficiencies. *Appl. Phys. Lett.* **84**, 3397–3399 (2004).

[20] Grätzel, M.: The advent of mesoscopic injection solar cells. *Prog. Photovolt.: Res. Appl.* **14**, 429–442 (2006).

[21] Riede, M., Uhrich, C., Widmer, J., Timmreck, R., Wynands, D., Schwartz, G., Gnehr, W.-M., Hildebrandt, D., Weiss, A., Hwang, J., Sundarraj, S., Erk, P., Pfeiffer, M. & Leo, K.: Efficient organic tandem solar cells based on small molecules. *Adv. Funct. Mater.* **21**, 3019–3028 (2011).

[22] Schmidt-Mende, L., Zakeeruddin, S. M. & Grätzel, M.: Efficiency improvement in solid-state-dye-sensitized photovoltaics with an amphiphilic ruthenium-dye. *Appl. Phys. Lett.* **86**, 013504 (2005).

[23] Schlichthörl, G., Huang, S. Y., Sprague, J. & Frank, A. J.: Band edge movement and recombination kinetics in dye-sensitized nanocrystalline TiO_2 solar cells: a study by intensity modulated photovoltage spectroscopy. *J. Phys. Chem. B* **101**, 8141–8155 (1997).

[24] Haque, S. A., Tachibana, Y., Willis, R. L., Moser, J. E., Grätzel, M., Klug, D. R. & Durrant, J. R.: Parameters influencing charge recombination kinetics in dye-sensitized nanocrystalline titanium dioxide films. *J. Phys. Chem. B* **104**, 538–547 (2000).

[25] Nelson, J., Haque, S. A., Klug, D. R. & Durrant, J. R.: Trap-limited recombination in dye-sensitized nanocrystalline metal oxide electrodes. *Phys. Rev. B* **6320**, 205321 (2001).

[26] Lenzmann, F. O. & Kroon, J. M.: Recent advances in dye-sensitized solar cells. *Adv. OptoElectron.* **2007**, 65073 (2007).

[27] Durrant, J. R., Haque, S. A. & Palomares, E.: Towards optimisation of electron transfer processes in dye sensitised solar cells. *Coord. Chem. Rev.* **248**, 1247 (2004).

[28] Snaith, H. J., Petrozza, A., Ito, S., Miura, H. & Grätzel, M.: Charge generation and photovoltaic operation of solid-state dye-sensitized solar cells incorporating a high extinction coefficient indolene-based sensitizer. *Adv. Funct. Mater.* **19**, 1810–1818 (2009).

[29] Howard, I. A., Meister, M., Baumeier, B., Wonneberger, H., Pschirer, N., Sens, R., Bruder, I., Li, C., Mllen, K., Andrienko, D. & Laquai, F.: Two channels of charge generation in perylene monoimide solid-state dye-sensitized solar cells. *Adv. Energ. Mater.* **4**, 1300640 (2014).

[30] Zaban, A., Meier, A. & Gregg, B.: Electric potential distribution and short-range screening in nanoporous TiO_2 electrodes. *J. Phys. Chem. B* **101**, 7985–7990 (1997).

[31] Könenkamp, R., Henninger, R. & Hoyer, P.: Photocarrier transport in colloidal TiO_2 films. *J. Phys. Chem.* **97**, 7328–7330 (1993).

[32] Schwarzburg, K. & Willig, F.: Influence of trap filling on photocurrent transients in polycrystalline TiO_2. *Appl. Phys. Lett.* **58**, 2520–2522 (1991).

[33] de Jongh, P. & Vanmaekelbergh, D.: Trap-limited electronic transport in assemblies of nanometer-size TiO_2 particles. *Phys. Rev. Lett.* **77**, 3427–3430 (1996).

[34] Kopidakis, N., Benkstein, K. D., van de Lagemaat, J. & Frank, A. J.: Transport-limited recombination of photocarriers in dye-sensitized nanocrystalline TiO_2 solar cells. *J. Phys. Chem. B* **107**, 11307–11315 (2003).

[35] Dunn, H. K. & Peter, L. M.: How efficient is electron collection in dye-sensitized solar cells? Comparison of different dynamic methods for the determination of the electron diffusion length. *J. Phys. Chem. C* **113**, 4726–4731 (2009).

[36] Frank, A., Kopidakis, N. & van de Lagemaat, J.: Electrons in nanostructured TiO_2 solar cells: transport, recombination and photovoltaic properties. *Coord. Chem. Rev.* **248**, 1165–1179 (2004).

[37] Kopidakis, N., Neale, N. R., Zhu, K. & Frank, A. J.: Spatial location of transport-limiting traps in TiO_2 nanoparticle films in dye-sensitized solar cells. *Appl. Phys. Lett.* **87**, 202106 (2005).

[38] Bach, U., Lupo, D., Comte, P., Moser, J.-E., Weissortel, F., Salbeck, J., Spreitzer, H. & Grätzel, M.: Solid-state dye-sensitized mesoporous TiO_2 solar cells with high photon-to-electron conversion efficiencies. *Nature* **395**, 583 (1998).

[39] Cai, N., Moon, S.-J., Cevey-Ha, L., Moehl, T., Humphry-Baker, R., Wang, P., Zakeeruddin, S. M. & Grätzel, M.: An organic d--a dye for record efficiency solid-state sensitized heterojunction solar cells. *Nano Lett.* **11**, 1452–1456 (2011).

[40] Mathew, S., Yella, A., Gao, P., Humphry-Baker, R., Curchod, B. F. E., Ashari-Astani, N., Tavernelli, I., Rothlisberger, U., Nazeeruddin, M. K. & Grätzel, M.: Dye-sensitized solar cells with 13% efficiency achieved through the molecular engineering of porphyrin sensitizers. *Nat. Chem.* **6**, 242–247 (2014).

[41] Tang, H., Berger, H., Schmid, P., Levy, F. & Burri, G.: Photoluminescence in TiO_2 anatase single-crystals. *Solid State Commun.* **87**, 847–850 (1993).

[42] Forro, L., Chauvet, O., Emin, D., Zuppiroli, L., Berger, H. & Levy, F.: High mobility n-type charge carriers in large single crystals of anatase TiO_2. *J. Appl. Phys.* **75**, 633–635 (1994).

[43] Levinshtein, M., Rumyantsev, S. & Shur, M.: Handbook series on semiconductor parameters. 1. Si, Ge, C (diamond), GaAs, GaP, GaSb, InAs, InP, InSb (World Scientific Publishing Company, Incorporated, 1996).

[44] Moser, S., Moreschini, L., Jaćimović, J., Barišić, O. S., Berger, H., Magrez, A., Chang, Y. J., Kim, K. S., Bostwick, A., Rotenberg, E., Forró, L. & Grioni, M.: Tunable polaronic conduction in anatase TiO_2. *Phys. Rev. Lett.* **110**, 196403 (2013).

[45] Dittrich, T., Lebedev, E. & Weidmann, J.: Electron drift mobility in porous TiO_2 (anatase). *Phys. Status Solidi A* **165**, R5–R6 (1998).

[46] Solbrand, A., Lindstrom, H., Rensmo, H., Hagfeldt, A., Lindquist, S. E. & Sodergren, S.: Electron transport in the nanostructured TiO_2-electrolyte system studied with time-resolved photocurrents. *J. Phys. Chem. B* **101**, 2514 (1997).

[47] Cao, F., Oskam, G., Meyer, G. & Searson, P.: Electron transport in porous nanocrystalline TiO_2 photoelectrochemical cells. *J. Phys. Chem.* **100**, 17021–17027 (1996).

[48] van de Lagemaat, J. & Frank, A. J.: Nonthermalized electron transport in dye-sensitized nanocrystalline TiO_2 films: transient photocurrent and random-walk modeling studies. *J. Phys. Chem. B* **105**, 11194–11205 (2001).

[49] Bisquert, J.: Chemical diffusion coefficient of electrons in nanostructured semiconductor electrodes and dye-sensitized solar cells. *J. Phys. Chem. B* **108**, 2323–2332 (2004).

[50] Bisquert, J. & Vikhrenko, V.: Interpretation of the time constants measured by kinetic techniques in nanostructured semiconductor electrodes and dye-sensitized solar cells. *J. Phys. Chem. B* **108**, 2313–2322 (2004).

[51] Petrozza, A., Groves, C. & Snaith, H. J.: Electron transport and recombination in dye-sensitized mesoporous TiO_2 probed by photoinduced charge-conductivity modulation spectroscopy with monte carlo modeling. *J. Am. Chem. Soc.* **130**, 12912–12920 (2008).

[52] Hendry, E., Koeberg, M., O'Regan, B. & Bonn, M.: Local field effects on electron transport in nanostructured TiO_2 revealed by terahertz spectroscopy. *Nano Lett.* **6**, 755 (2006).

[53] Tiwana, P., Parkinson, P., Johnston, M. B., Snaith, H. J. & Herz, L. M.: Ultrafast terahertz conductivity dynamics in mesoporous TiO_2: Influence of dye sensitization and surface treatment in solid-state dye-sensitized solar cells. *J. Phys. Chem. C* **114**, 1365–1371 (2010).

[54] Krüger, J., Plass, R., Grätzel, M., Cameron, P. J. & Peter, L. M.: Charge transport and back reaction in solid-state dye-sensitized solar cells: A study using intensity-modulated photovoltage and photocurrent spectroscopy. *J. Phys. Chem. B* **107**, 7536–7539 (2003).

[55] Jennings, J. R. & Peter, L. M.: A reappraisal of the electron diffusion length in solid-state dye-sensitized solar cells. *J. Phys. Chem. C* **111**, 16100–16104 (2007).

[56] Snaith, H. J. & Schmidt-Mende, L.: Advances in liquid-electrolyte and solid-state dye-sensitized solar cells. *Adv. Mater.* **19**, 3187–3200 (2007).

[57] Jose, R., Thavasi, V. & Ramakrishna, S.: Metal oxides for dye-sensitized solar cells. *J. Am. Ceram. Soc.* **92**, 289–301 (2009).

[58] Tiwana, P., Docampo, P., Johnston, M. B., Snaith, H. J. & Herz, L. M.: Electron mobility and injection dynamics in mesoporous ZnO, SnO_2, and TiO_2 films used in dye-sensitized solar cells. *ACS Nano* **5**, 5158 (2011).

[59] Gong, D., Grimes, C., Varghese, O., Hu, W., Singh, R., Chen, Z. & Dickey, E.: Titanium oxide nanotube arrays prepared by anodic oxidation. *J. Mater. Res.* **16**, 3331–3334 (2001).

[60] Berger, S., Hahn, R., Roy, P. & Schmuki, P.: Self-organized TiO_2 nanotubes: Factors affecting their morphology and properties. *Phys. Status Solidi B* **247**, 2424–2435 (2010).

[61] Weickert, J., Palumbiny, C., Nedelcu, M., Bein, T. & Schmidt-Mende, L.: Controlled growth of TiO_2 nanotubes on conducting glass. *Chem. Mater.* **23**, 155–162 (2011).

[62] Tighineanu, A., Ruff, T., Albu, S., Hahn, R. & Schmuki, P.: Conductivity of TiO_2 nanotubes: Influence of annealing time and temperature. *Chem. Phys. Lett.* **494**, 260–263 (2010).

[63] Mor, G. K., Varghese, O. K., Paulose, M., Shankar, K. & Grimes, C. A.: A review on highly ordered, vertically oriented TiO_2 nanotube arrays: Fabrication, material properties, and solar energy applications. *Sol. Energy Mater. Sol. Cells* **90**, 2011–2075 (2006).

[64] Zhu, K., Neale, N. R., Miedaner, A. & Frank, A. J.: Enhanced charge-collection efficiencies and light scattering in dye-sensitized solar cells using oriented TiO_2 nanotubes arrays. *Nano Lett.* **7**, 69–74 (2007).

[65] Paulose, M., Shankar, K., Varghese, O., Mor, G. & Grimes, C.: Application of highly-ordered TiO_2 nanotube-arrays in heterojunction dye-sensitized solar cells. *J. Phys. D.* **39**, 2498–2503 (2006).

[66] Jennings, J. R., Ghicov, A., Peter, L. M., Schmuki, P. & Walker, A. B.: Dye-sensitized solar cells based on oriented TiO_2 nanotube arrays: Transport, trapping, and transfer of electrons. *J. Am. Chem. Soc.* **130**, 13364–13372 (2008).

[67] Wang, J. & Lin, Z.: Dye-sensitized TiO_2 nanotube solar cells with markedly enhanced performance via rational surface engineering. *Chem. Mater.* **22**, 579–584 (2010).

[68] Mitzi, D. B.: Synthesis, Structure, and Properties of Organic-Inorganic Perovskites and Related Materials, vol. 48 of *Progress in Inorganic Chemistry*, chap. 1, 1–121 (John Wiley & Sons, Inc., Hoboken, NJ, US, 1999).

[69] Mitzi, D. B., Chondroudis, K. & Kagan, C. R.: Organic-inorganic electronics. *IBM J. Res. Dev.* **45**, 29–45 (2001).

[70] Kojima, A., Teshima, K., Shirai, Y. & Miyasaka, T.: Organometal halide perovskites as visible-light sensitizers for photovoltaic cells. *J. Am. Chem. Soc.* **131**, 6050–6051 (2009).

[71] Im, J.-H., Lee, C.-R., Lee, J.-W., Park, S.-W. & Park, N.-G.: 6.5% efficient perovskite quantum-dot-sensitized solar cell. *Nanoscale* **3**, 4088–4093 (2011).

[72] Ball, J. M., Lee, M. M., Hey, A. & Snaith, H. J.: Low-temperature processed meso-superstructured to thin-film perovskite solar cells. *Energy Environ. Sci.* **6**, 1739–1743 (2013).

[73] Heo, J. H., Im, S. H., Noh, J. H., Mandal, T. N., Lim, C.-S., Chang, J. A., Lee, Y. H., Kim, H.-j., Sarkar, A., K., N., Grätzel, M. & Seok, S. I.: Efficient inorganic-organic hybrid heterojunction solar cells containing perovskite compound and polymeric hole conductors. *Nat. Photon.* **7**, 486–491 (2013).

[74] Eperon, G. E., Burlakov, V. M., Docampo, P., Goriely, A. & Snaith, H. J.: Morphological control for high performance, solution-processed planar heterojunction perovskite solar cells. *Adv. Funct. Mater.* **24**, 151–157 (2014).

[75] Koutselas, I. B., Ducasse, L. & Papavassiliou, G. C.: Electronic properties of three- and low-dimensional semiconducting materials with Pb halide and Sn halide units. *J. Phys.: Condens. Matter* **8**, 1217 (1996).

[76] Umebayashi, T., Asai, K., Kondo, T. & Nakao, A.: Electronic structures of lead iodide based low-dimensional crystals. *Phys. Rev. B* **67**, 155405 (2003).

[77] Mosconi, E., Amat, A., Nazeeruddin, M. K., Grätzel, M. & De Angelis, F.: First principles modeling of mixed halide organometal perovskites for photovoltaic applications. *J. Phys. Chem. C* **117**, 1390213913 (2013).

[78] Even, J., Pedesseau, L., Jancu, J.-M. & Katan, C.: Importance of spin-orbit coupling in hybrid organic/inorganic perovskites for photovoltaic applications. *J. Phys. Chem. Lett.* **4**, 2999–3005 (2013).

[79] Ishihara, T.: Optical properties of PbI-based perovskite structures. *J. Lumin.* **60**, 269–274 (1994).

[80] Papavassiliou, G. C. & Koutselas, I. B.: Structural, optical and related properties of some natural 3-dimensional and lower-dimensional semiconductor systems. *Synth. Met.* **71**, 1713–1714 (1995).

[81] Papavassiliou, G., Mousids, G., Koutselas, I. & Papaionannou, G.: Excitonic bands in the photoconductivity spectra of some organic-inorganic hybrid compounds based on metal halide units. *Int. J. Mod. Phys. B* **15**, 3727–3731 (2001).

[82] Stoumpos, C. C., Malliakas, C. D. & Kanatzidis, M. G.: Semiconducting tin and lead iodide perovskites with organic cations: Phase transitions, high mobilities, and near-infrared photoluminescent properties. *Inorg. Chem.* **52**, 9019–9038 (2013).

[83] Eperon, G. E., Stranks, S. D., Menelaou, C., Johnston, M. B., Herz, L. M. & Snaith, H. J.: Formamidinium lead trihalide: a broadly tunable perovskite for efficient planar heterojunction solar cells. *Energy Environ. Sci.* **7**, 982–988 (2014).

[84] Noh, J. H., Im, S. H., Heo, J. H., Mandal, T. N. & Seok, S. I.: Chemical management for colorful, efficient, and stable inorganicorganic hybrid nanostructured solar cells. *Nano Lett.* **13**, 1764–1769 (2013).

[85] Colella, S., Mosconi, E., Fedeli, P., Listorti, A., Gazza, F., Orlandi, F., Ferro, P., Besagni, T., Rizzo, A., Calestani, G., Gigli, G., De Angelis, F. & Mosca, R.: $MAPbI_{3-x}Cl_x$ mixed halide perovskite for hybrid solar cells: the role of chloride as dopant on the transport and structural properties. *Chem. Mater.* **25**, 4613–4618 (2013).

[86] Kitazawa, N., Watanabe, Y. & Nakamura, Y.: Optical properties of $CH_3NH_3PbX_3$ (X = halogen) and their mixed-halide crystals. *J. Mater. Sci.* **37**, 3585–3587 (2002).

[87] Stranks, S. D., Eperon, G. E., Grancini, G., Menelaou, C., Alcocer, M. J. P., Leijtens, T., Herz, L. M., Petrozza, A. & Snaith, H. J.: Electron-hole diffusion lengths exceeding 1 micrometer in an organometal trihalide perovskite absorber. *Science* **342**, 341–344 (2013).

[88] Xing, G., Mathews, N., Sun, S., Lim, S. S., Lam, Y. M., Grätzel, M., Mhaisalkar, S. & Sum, T. C.: Long-range balanced electron- and hole-transport lengths in organic-inorganic $CH_3NH_3PbI_3$. *Science* **342**, 344–347 (2013).

[89] Sun, S., Salim, T., Mathews, N., Duchamp, M., Boothroyd, C., Xing, G., Sum, T. C. & Lam, Y. M.: The origin of high efficiency in low-temperature solution-processable bilayer organometal halide hybrid solar cells. *Energy Environ. Sci.* **7**, 339–407 (2014).

[90] Hirasawa, M., Ishihara, T., Goto, T., Uchida, K. & Miura, N.: Magnetoabsorption of the lowest exciton in perovskite-type compound $(CH_3NH_3)PbI_3$. *Physica B* **201**, 427 – 430 (1994).

[91] D'Innocenzo, V., Grancini, G., Alcocer, M. J. P., Kandada, A. R. S., Stranks, S. D., Lee, M. M., Lanzani, G., Snaith, H. J. & Petrozza, A.: Excitons versus free charges in organo-lead tri-halide perovskites. *Nat. Commun.* **5**, 3586 (2014).

[92] Docampo, P., Ball, J. M., Darwich, M., Eperon, G. E. & Snaith, H. J.: Efficient organometal trihalide perovskite planar-heterojunction solar cells on flexible polymer substrates. *Nat. Commun.* **4**, 2761 (2013).

[93] Menzel, R.: Photonics (Springer Berlin Heidelberg, 2007).

[94] Kuzmany, H.: Solid-State Spectroscopy (Springer Berlin Heidelberg, 2009).

[95] Beard, M. C., Turner, G. M. & Schmuttenmaer, C. A.: Terahertz spectroscopy. *J. Phys. Chem. B* **106**, 7146 (2002).

[96] Schmuttenmaer, C. A.: Exploring dynamics in the far-infrared with terahertz spectroscopy. *Chem. Rev.* **104**, 1759–1779 (2004).

[97] Hangyo, M., Tani, M. & Nagashima, T.: Terahertz time-domain spectroscopy of solids: A review. *Int. J. Infrared Millimeter Waves* **26**, 1661–1690 (2005).

[98] Nvemec, H., Kužel, P. & Sundström, V.: Charge transport in nanostructured materials for solar energy conversion studied by time-resolved terahertz spectroscopy. *J. Photochem. Photobiol. A-Chem.* **215**, 123–139 (2010).

[99] Ulbricht, R., Hendry, E., Shan, J., Heinz, T. F. & Bonn, M.: Carrier dynamics in semiconductors studied with time-resolved terahertz spectroscopy. *Rev. Mod. Phys.* **83**, 543–586 (2011).

[100] Lloyd-Hughes, J. & Jeon, T.-I.: A review of the terahertz conductivity of bulk and nano-materials. *J. Infrared Millim. Terahertz Waves* **33**, 871–925 (2012).

[101] Kroeze, J. E., Savenije, T. J. & Warman, J. M.: Electrodeless determination of the trap density, decay kinetics, and charge separation efficiency of dye-sensitized nanocrystalline TiO_2. *J. Am. Chem. Soc.* **126**, 7608–7618 (2004).

[102] Nienhuys, H.-K. & Sundström, V.: Intrinsic complications in the analysis of optical-pump, terahertz probe experiments. *Phys. Rev. B* **71**, 235110 (2005).

[103] Fox, M.: Optical Properties of Solids (Oxford University Press, 2010), 2 edn.

[104] Tani, M., Matsuura, S., Sakai, K. & Nakashima, S.: Emission characteristics of photoconductive antennas based on low-temperature-grown GaAs and semi-insulating GaAs. *Appl. Optics* **36**, 7853 (1997).

[105] Cook, D. J. & Hochstrasser, R. M.: Intense terahertz pulses by four-wave rectification in air. *Opt. Lett.* **25**, 1210–1212 (2000).

[106] Nahata, A., Weling, A. S. & Heinz, T. F.: A wideband coherent terahertz spectroscopy system using optical rectification and electro-optic sampling. *Appl. Phys. Lett.* **69**, 2321 (1996).

[107] Tani, M., Sakai, K. & Mimura, H.: Ultrafast photoconductive detectors based on semi-insulating GaAs and InP. *Jpn. J. Appl. Phys. Part 2 - Lett.* **36**, L1175–L1178 (1997).

[108] Dai, J., Xie, X. & Zhang, X.-C.: Detection of broadband terahertz waves with a laser-induced plasma in gases. *Phys. Rev. Lett.* **97**, 103903 (2006).

[109] Pelant, I. & Valenta, J.: Luminescence Spectroscopy of Semiconductors (Oxford University Press, 2012).

[110] Reddy, K. M., Manorama, S. V. & Reddy, A. R.: Bandgap studies on anatase titanium dioxide nanoparticles. *Mater. Chem. Phys.* **78**, 239 – 245 (2003).

[111] Liu, H., Yao, J. & Puri, A.: Second and third harmonic generation in BBO by femtosecond Ti:sapphire laser pulses. *Opt. Commun.* **109**, 139 – 144 (1994).

[112] Beranek, R., Hildebrand, H. & Schmuki, P.: Self-organized porous titanium oxide prepared in H_2SO_4/HF electrolytes. *Electrochem. Solid-State Lett.* **6**, B12–B14 (2003).

[113] Hendry, E., Wang, F., Shan, J., Heinz, T. F. & Bonn, M.: Electron transport in TiO_2 probed by thz time-domain spectroscopy. *Phys. Rev. B* **69**, 081101 (2004).

[114] Kroeze, J. E., Savenije, T. J. & Warman, J. M.: Contactless determination of the efficiency of photo-induced charge separation in a porphyrin-TiO_2 bilayer. *J. Photochem. Photobiol. A* **148**, 49 – 55 (2002).

[115] Jepsen, P. U., Schairer, W., Libon, I. H., Lemmer, U., Hecker, N. E., Birkholz, M., Lips, K. & Schall, M.: Ultrafast carrier trapping in microcrystalline silicon observed in optical pump–terahertz probe measurements. *Appl. Phys. Lett.* **79**, 1291–1293 (2001).

[116] Bauer, C., Boschloo, G., Mukhtar, E. & Hagfeldt, A.: Ultrafast relaxation dynamics of charge carriers relaxation in zno nanocrystalline thin films. *Chem. Phys. Lett.* **387**, 176–181 (2004).

[117] Cooke, D. G., Hegmann, F. A., Mazur, Y. I., Wang, Z. M., Black, W., Wen, H., Salamo, G. J., Mishima, T. D., Lian, G. D. & Johnson, M. B.: Ultrafast carrier capture dynamics in InGaAs/GaAs quantum wires. *J. Appl. Phys.* **103**, 023710 (2008).

[118] Fekete, L., Kužel, P., Němec, H., Kadlec, F., Dejneka, A., Stuchlík, J. & Fejfar, A.: Ultrafast carrier dynamics in microcrystalline silicon probed by time-resolved terahertz spectroscopy. *Phys. Rev. B* **79**, 115306 (2009).

[119] Wang, X., Feng, Z., Shi, J., Jia, G., Shen, S., Zhou, J. & Li, C.: Trap states and carrier dynamics of TiO_2 studied by photoluminescence spectroscopy under weak excitation condition. *Phys. Chem. Chem. Phys.* **12**, 7083–7090 (2010).

[120] Zhao, H., Zhang, Q. & Weng, Y.-X.: Deep surface trap filling by photoinduced carriers and interparticle electron transport observed in TiO_2 nanocrystalline film with time-resolved visible and mid-IR transient spectroscopies. *J. Phys. Chem. C* **111**, 3762–3769 (2007).

[121] Munnix, S. & Schmeits, M.: Origin of defect states on the surface of TiO_2. *Phys. Rev. B* **31**, 3369–3371 (1985).

[122] Diebold, U.: The surface science of titanium dioxide. *Surf. Sci. Rep.* **48**, 53–229 (2003).

[123] Wu, P.-G., Ma, C.-H. & Shang, J.: Effects of nitrogen doping on optical properties of TiO_2 thin films. *Appl. Phys. A* **81**, 1411–1417 (2005).

[124] Ruan, C., Paulose, M., Varghese, O. K. & Grimes, C. A.: Enhanced photoelectrochemical-response in highly ordered tio2 nanotube-arrays anodized in boric acid containing electrolyte. *Solar Energy Materials and Solar Cells* **90**, 1283 – 1295 (2006).

[125] Marino, C. E., Nascente, P. A., Biaggio, S. R., Rocha-Filho, R. C. & Bocchi, N.: {XPS} characterization of anodic titanium oxide films grown in phosphate buffer solutions. *Thin Solid Films* **468**, 109 – 112 (2004).

[126] Dittrich, T., Weidmann, J., Koch, F., Uhlendorf, I. & Lauermann, I.: Temperature- and oxygen partial pressure-dependent electrical conductivity in nanoporous rutile and anatase. *Appl. Phys. Lett.* **75**, 3980–3982 (1999).

[127] Varghese, O., Gong, D., Paulose, M., Ong, K., Dickey, E. & Grimes, C.: Extreme changes in the electrical resistance of titania nanotubes with hydrogen exposure. *Adv. Mater.* **15**, 624–627 (2003).

[128] Fujishima, A., Zhang, X. & Tryk, D. A.: TiO_2 photocatalysis and related surface phenomena. *Surf. Sci. Rep.* **63**, 515 – 582 (2008).

[129] Thompson, T. & Yates, J.: Tio_2-based photocatalysis: Surface defects, oxygen and charge transfer. *Top. Catal.* **35**, 197–210 (2005).

[130] Westermark, K., Henningsson, A., Rensmo, H., Sdergren, S., Siegbahn, H. & Hagfeldt, A.: Determination of the electronic density of states at a nanostructured TiO_2/Ru-dye/electrolyte interface by means of photoelectron spectroscopy. *Chem. Phys.* **285**, 157 – 165 (2002).

[131] Sekiya, T., Yagisawa, T., Kamiya, N., Das Mulmi, D., Kurita, S., Murakami, Y. & Kodaira, T.: Defects in anatase TiO_2 single crystal controlled by heat treatments. *J. Phys. Soc. Jpn.* **73**, 703–710 (2004).

[132] Desilvestro, J., Grätzel, M., Kavan, L., Moser, J. & Augustynski, J.: Highly efficient sensitization of titanium-dioxide. *J. Am. Chem. Soc.* **107**, 2988–2990 (1985).

[133] Richter, C. & Schmuttenmaer, C. A.: Exciton-like trap states limit electron mobility in TiO_2 nanotubes. *Nat. Nanotech.* **5**, 769–772 (2010).

[134] Roberts, S.: Dielectric constants and polarizabilities of ions in simple crystals and barium titanate. *Phys. Rev.* **76**, 1215–1220 (1949).

[135] Gonzalez, R. J., Zallen, R. & Berger, H.: Infrared reflectivity and lattice fundamentals in anatase TiO_2. *Phys. Rev. B* **55**, 7014–7017 (1997).

[136] Smith, N. V.: Classical generalization of the Drude formula for the optical conductivity. *Phys. Rev. B* **64**, 155106 (2001).

[137] Němec, H., Kužel, P. & Sundström, V.: Far-infrared response of free charge carriers localized in semiconductor nanoparticles. *Phys. Rev. B* **79**, 115309 (2009).

[138] Mitzi, D., Feild, C., Schlesinger, Z. & Laibowitz, R.: Transport, optical, and magnetic properties of the conducting halide perovskite $CH_3NH_3SnI_3$. *J. Solid State Chem.* **114**, 159 – 163 (1995).

[139] Takahashi, Y., Obara, R., Nakagawa, K., Nakano, M., Tokita, J.-y. & Inabe, T.: Tunable charge transport in soluble organicinorganic hybrid semiconductors. *Chem. Mater.* **19**, 6312–6316 (2007).

[140] Hirasawa, M., Ishihara, T. & Goto, T.: Exciton features in 0-, 2-, and 3-dimensional networks of $[PbI_6]^{4-}$ octahedra. *J. Phys. Soc. Jpn.* **63**, 3870–3879 (1994).

[141] Tanaka, K., Takahashi, T., Ban, T., Kondo, T., Uchida, K. & Miura, N.: Comparative study on the excitons in lead-halide-based perovskite-type crystals $CH_3NH_3PbBr_3$ $CH_3NH_3PbI_3$. *Solid State Commun.* **127**, 619 – 623 (2003).

[142] Langevin, P.: The recombination and mobilities of ions in gases. *Ann. Chim. Phys.* **28**, 433–530 (1903).

[143] Pope, M. & Swenberg, C. E.: Electronic Processes in Organic Crystals and Polymers. Monographs on the Physics and Chemistry of Materials (Oxford Science, New York, 1999).

[144] Abate, A., Leijtens, T., Pathak, S., Teuscher, J., Avolio, R., Errico, M. E., Kirkpatrik, J., Ball, J. M., Docampo, P., McPherson, I. & Snaith, H. J.: Lithium salts as redox active p-type dopants for organic semiconductors and their impact in solid-state dye-sensitized solar cells. *Phys. Chem. Chem. Phys.* **15**, 2572 (2013).

[145] Beattie, A. R. & Landsberg, P. T.: Auger effect in semiconductors. *P. Roy. Soc. Lond. A Mat.* **249**, 16–29 (1959).

[146] Haug, A.: Band-to-band auger recombination in semiconductors. *J. Phys. Chem. Solids* **49**, 599 – 605 (1988).

[147] Lloyd-Hughes, J., Merchant, S. K. E., Fu, L., Tan, H. H., Jagadish, C., Castro-Camus, E. & Johnston, M. B.: Influence of surface passivation on ultrafast carrier dynamics and terahertz radiation generation in GaAs. *Appl. Phys. Lett.* **89**, 232102 (2006).

[148] Parkinson, P., Lloyd-Hughes, J., Johnston, M. B. & Herz, L. M.: Efficient generation of charges via below-gap photoexcitation of polymer-fullerene blend films investigated by terahertz spectroscopy. *Phys. Rev. B* **78**, 115321 (2008).

[149] de Haas, M. P., Warman, J. M. & Anthopoulos, T. D.: The mobility and decay kinetics of charge carriers in pulse-ionized microcrystalline PCBM powder. *Adv. Funct. Mater.* **16**, 2274 (2006).

[150] Defranzo, A. C. & Pazol, B. G.: Index of refraction measurement on sapphire at low-temperatures and visible wavelengths. *Appl. Optics* **32**, 2224–2234 (1993).

[151] Pivrikas, A., Juška, G., Mozer, A. J., Scharber, M., Arlauskas, K., Sariciftci, N. S., Stubb, H. & Österbacka, R.: Bimolecular recombination coefficient as a sensitive testing parameter for low-mobility solar-cell materials. *Phys. Rev. Lett.* **94**, 176806 (2005).

[152] Adriaenssens, G. J. & Arkhipov, V. I.: Non-langevin recombination in disordered materials with random potential distributions. *Solid State Commun.* **103**, 541–543 (1997).

[153] Makino, T., Watanabe, M., Hayashi, T. & Ashida, M.: Time-resolved luminescence of exciton polaritons in PbI_2. *Phys. Rev. B* **57**, 3714–3717 (1998).

[154] Iwanaga, M., Watanabe, M. & Hayashi, T.: Relaxation of excitons into charge-separated pairs in $PbBr_2$ and $PbCl_2$ crystals. *Int. J. Mod. Phys. B* **15**, 3677–3680 (2001).

[155] Williams, R. & Song, K.: The self-trapped exciton. *J. Phys. Chem. Solids* **51**, 679 – 716 (1990).

[156] Lee, K., Heeger, A. J. & Cao, Y.: Reflectance of polyaniline protonated with camphor sulfonic acid: Disordered metal on the metal-insulator boundary. *Phys. Rev. B* **48**, 14884–14891 (1993).

[157] D'Andrade, B. & Forrest, S.: White organic light-emitting devices for solid-state lighting. *Adv. Mater.* **16**, 1585–1595 (2004).

[158] Forrest, S.: The path to ubiquitous and low-cost organic electronic appliances on plastic. *Nature* **428**, 911–918 (2004).

[159] Bae, S., Kim, H., Lee, Y., Xu, X., Park, J.-S., Zheng, Y., Balakrishnan, J., Lei, T., Ri Kim, H., Song, Y. I., Kim, Y.-J., Kim, K. S., Ozyilmaz, B., Ahn, J.-H., Hong, B. H. & Iijima, S.: Roll-to-roll production of 30-inch graphene films for transparent electrodes. *Nat. Nano.* **5**, 574–578 (2010).

[160] Dualeh, A., Ttreault, N., Moehl, T., Gao, P., Nazeeruddin, M. K. & Grätzel, M.: Effect of annealing temperature on film morphology of organicinorganic hybrid pervoskite solid-state solar cells. *Adv. Funct. Mater.* **in press**, DOI: 10.1002/adfm.201304022 (2014).

[161] Conings, B., Baeten, L., De Dobbelaere, C., D'Haen, J., Manca, J. & Boyen, H.-G.: Perovskite-based hybrid solar cells exceeding 10% efficiency with high reproducibility using a thin film sandwich approach. *Adv. Mater.* **26**, 2041–2046 (2013).

[162] Huber, R., Schmid, B. A., Kaindl, R. A. & Chemla, D. S.: Femtosecond thz studies of intra-excitonic transitions. *Phys. Status Solidi B* **245**, 1041–1048 (2008).

[163] Maalej, A., Abid, Y., Kallel, A., Daoud, A., Lauti, A. & Romain, F.: Phase transitions and crystal dynamics in the cubic perovskite $CH_3NH_3PbCl_3$. *Solid State Commun.* **103**, 279 – 284 (1997).

[164] Quarti, C., Grancini, G., Mosconi, E., Bruno, P., Ball, J. M., Lee, M. M., Snaith, H. J., Petrozza, A. & Angelis, F. D.: The raman spectrum of the $CH_3NH_3PbI_3$ hybrid perovskite: Interplay of theory and experiment. *J. Phys. Chem. Lett* **5**, 279–284 (2014).

[165] Onoda-Yamamuro, N., Matsuo, T. & Suga, H.: Dielectric study of $CH_3NH_3PbX_3$ (X = Cl, Br, I). *J. Phys. Chem. Solids* **53**, 935–939 (1992).

[166] Marchioro, A., Teuscher, J., Friedrich, D., Kunst, M., van de Krol, R., Moehl, T., Grätzel, M. & Moser, J.-E.: Unravelling the mechanism of photoinduced charge transfer processes in lead iodide perovskite solar cells. *Nat. Photon.* **8**, 250–255 (2014).

[167] Choi, T., Lee, S., Choi, Y. J., Kiryukhin, V. & Cheong, S.-W.: Switchable ferroelectric diode and photovoltaic effect in bifeo3. *Science* **324**, 63–66 (2009).

[168] Grinberg, I., West, D. V., Torres, M., Gou, G., Stein, D. M., Wu, L., Chen, G., Gallo, E. M., Akbashev, A. R., Davies, P. K., Spanier, J. E. & Rappe, A. M.: Perovskite oxides for visible-light-absorbing ferroelectric and photovoltaic materials. *Nature* **503**, 509–512 (2013).

[169] Gonzalez-Pedro, V., Jurez-Prez, E. J., Arsyad, W. S., Barea, E. M., Fabregat-Santiago, F., Mora-Sero, I. & Bisquert, J.: General working principles of $CH_3NH_3PbX_3$ perovskite solar cells. *Nano Lett.* **14**, 888–893 (2014).

[170] Svelto, O.: Principles of Lasers (Springer, New York, NY, USA, 2010).

[171] Cai, B., Xing, Y., Yang, Z., Zhang, W.-H. & Qiu, J.: High performance hybrid solar cells sensitized by organolead halide perovskites. *Energy Environ. Sci.* **6**, 1480–1485 (2013).

[172] Sturge, M. D.: Optical absorption of gallium arsenide between 0.6 and 2.75 ev. *Phys. Rev.* **127**, 768–773 (1962).

[173] Bässler, H. & Schweitzer, B.: Site-selective fluorescence spectroscopy of conjugated polymers and oligomers. *Acc. Chem. Res.* **32**, 173–182 (1999).

[174] Meskers, S. C. J., Hbner, J., Oestreich, M. & Bässler, H.: Dispersive relaxation dynamics of photoexcitations in a polyfluorene film involving energy transfer: experiment and monte carlo simulations. *J. Phys. Chem. B* **105**, 9139–9149 (2001).

[175] Herz, L. M., Silva, C., Grimsdale, A. C., Müllen, K. & Phillips, R. T.: Time-dependent energy transfer rates in a conjugated polymer guest-host system. *Phys. Rev. B* **70**, 165207 (2004).

[176] Song, L., El-Sayed, M. A. & Chen, P. C.: Spectral diffusion within the porous silicon emission wavelength range on the nanosecond to millisecond time scale. *J. Appl. Phys.* **82**, 836–839 (1997).

[177] Göbel, E. O. & Graudszus, W.: Optical detection of multiple-trapping relaxation in disordered crystalline semiconductors. *Phys. Rev. Lett.* **48**, 1277–1280 (1982).

[178] Haynes, J., Lax, M. & Flood, W.: Analysis of intrinsic recombination radiation from silicon and germanium. *J. Phys. Chem. Solids* **8**, 392 – 396 (1959).

[179] Ikehara, T. & Itoh, T.: Dynamical behavior of the exciton polariton in cucl: Coherent propagation and momentum relaxation. *Phys. Rev. B* **44**, 9283–9294 (1991).

[180] von der Osten, W. & Stolz, H.: Localized exciton states in silver halides. *J. Phys. Chem. Solids* **51**, 765 – 791 (1990).

[181] Heeger, A. J., Kivelson, S., Schrieffer, J. R. & Su, W. P.: Solitons in conducting polymers. *Rev. Mod. Phys.* **60**, 781–850 (1988).

[182] Furukawa, M., Mizuno, K.-i., Matsui, A., D. D. V. Rughooputh, S. & C. Walker, W.: Time-resolved excitonic luminescence processes in poly(phenylenevinylene). *J. Phys. Soc. Jpn.* **58**, 2976–2987 (1989).

[183] Känzig, W.: Electron spin resonance of v1-centers. *Phys. Rev.* **99**, 1890–1891 (1955).

[184] Lewis, J. T., Kolopus, J. L., Sonder, E. & Abraham, M. M.: Reorientation and motion of the self-trapped hole in $KMgF_3$. *Phys. Rev. B* **7**, 810–818 (1973).

[185] Tale, I., Springis, M., Rogulis, U., Ogorodnik, V., Kulis, P., Tale, V., Veispals, A. & Fitting, H.-J.: Self-trapped holes and recombination luminescence in $LiBaF_3$ crystals. *Radiat. Meas.* **33**, 751 – 754 (2001).

[186] Nayak, P. K., Garcia-Belmonte, G., Kahn, A., Bisquert, J. & Cahen, D.: Photovoltaic efficiency limits and material disorder. *Energy Environ. Sci.* **5**, 6022–6039 (2012).

[187] Tiwana, P., Docampo, P., Johnston, M. B., Herz, L. M. & Snaith, H. J.: The origin of an efficiency improving "light soaking" effect in SnO_2 based solid-state dye-sensitized solar cells. *Energy Environ. Sci.* **5**, 9566–9573 (2012).

[188] Even, J., Pedesseau, L., Jancu, J.-M. & Katan, C.: Dft and k p modelling of the phase transitions of lead and tin halide perovskites for photovoltaic cells. *Phys. Status Solidi A* **8**, 31–35 (2014).

[189] Frost, J. M., Butler, K. T., Brivio, F., Hendon, C. H., van Schilfgaarde, M. & Walsh, A.: Atomistic origins of high-performance in hybrid halide perovskite solar cells. *Nano Lett.* **14**, 25842590 (2014).

[190] Umari, P., Mosconi, E. & De Angelis, F.: Relativistic gw calculations on $CH_3NH_3PbI_3$ and $CH_3NH_3SnI_3$ perovskites for solar cell applications. *Sci. Rep.* **4**, 4467 (2014).

[191] Wang, Y., Gould, T., Dobson, J. F., Zhang, H., Yang, H., Yao, X. & Zhao, H.: Density functional theory analysis of structural and electronic properties of orthorhombic perovskite $CH_3NH_3PbI_3$. *Phys. Chem. Chem. Phys.* **16**, 1424–1429 (2014).

[192] Weber, D.: $CH_3NH_3PbX_3$, ein Pb(II)-system mit kubischer perowskitstruktur. *Z. Naturforsch. B* **33**, 1443–1445 (1978).

[193] Poglitsch, A. & Weber, D.: Dynamic disorder in methylammoniumtrihalogenoplumbates (ii) observed by millimeter-wave spectroscopy. *J. Chem. Phys.* **87**, 6373–6378 (1987).

[194] Kawamura, Y., Mashiyama, H. & Hasebe, K.: Structural study on cubic–tetragonal transition of $CH_3NH_3PbI_3$. *J. Phys. Soc. Jpn.* **71**, 1694–1697 (2002).

[195] Baikie, T., Fang, Y., Kadro, J. M., Schreyer, M., Wei, F., Mhaisalkar, S. G., Grätzel, M. & White, T. J.: Synthesis and crystal chemistry of the hybrid perovskite $(CH_3NH_3)PbI_3$ for solid-state sensitised solar cell applications. *J. Mater. Chem. A* **1**, 5628–5641 (2013).

[196] Wasylishen, R., Knop, O. & Macdonald, J.: Cation rotation in methylammonium lead halides. *Solid State Commun.* **56**, 581 – 582 (1985).

[197] Onoda-Yamamuro, N., Matsuo, T. & Suga, H.: Calorimetric and {IR} spectroscopic studies of phase transitions in methylammonium trihalogenoplumbates (ii). *J. Phys. Chem. Solids* **51**, 1383–1395 (1990).

[198] Yamada, Y., Nakamura, T., Endo, M., Wakamiya, A. & Kanemitsu, Y.: Near-band-edge optical responses of solution-processed organicinorganic hybrid perovskite $CH_3NH_3PbI_3$ on mesoporous TiO_2 electrodes. *Appl. Phys. Expr.* **7**, 032302 (2014).

[199] Saito, K., Kurosawa, T., Akai, T., Yokoyama, S., Morioka, H., Oikawa, T. & Funakubo, H.: Characterization of epitaxial $Pb(Zr_x,Ti_{1-x})O_3$ thin films with composition near the morphotropic phase boundary. In *Symposium U Ferroelectric Thin Films XI*, vol. 748 of *MRS Online Proceedings Library* (2002).

[200] Yokoyama, S., Honda, Y., Morioka, H., Oikawa, T., Funakubo, H., Iijima, T., Matsuda, H. & Saito, K.: Large piezoelectric response in (111)-oriented epitaxial Pb(Zr,Ti)O_3 films consisting of mixed phases with rhombohedral and tetragonal symmetry. *Appl. Phys. Lett.* **83**, 2408–2410 (2003).

[201] Kelman, M. B., McIntyre, P. C., Hendrix, B. C., Bilodeau, S. M., Roeder, J. F. & Brennan, S.: Structural analysis of coexisting tetragonal and rhombohedral phases in polycrystalline $Pb(Zr_{0.35}Ti_{0.65})O_3$ thin films. *J. Mater. Res.* **18**, 173–179 (2003).

[202] Zeches, R. J., Rossell, M. D., Zhang, J. X., Hatt, A. J., He, Q., Yang, C.-H., Kumar, A., Wang, C. H., Melville, A., Adamo, C., Sheng, G., Chu, Y.-H., Ihlefeld, J. F., Erni, R., Ederer, C., Gopalan, V., Chen, L. Q., Schlom, D. G., Spaldin, N. A., Martin, L. W. & Ramesh, R.: A strain-driven morphotropic phase boundary in $BiFeO_3$. *Science* **326**, 977–980 (2009).

[203] Chen, Z., You, L., Huang, C., Qi, Y., Wang, J., Sritharan, T. & Chen, L.: Nanoscale domains in strained epitaxial $BiFeO_3$ thin films on $LaSrAlO_4$ substrate. *Appl. Phys. Lett.* **96**, 252903 (2010).

[204] Ehm, L., Borkowski, L. A., Parise, J. B., Ghose, S. & Chen, Z.: Evidence of tetragonal nanodomains in the high-pressure polymorph of batio3. *Appl. Phys. Lett.* **98**, 021901 (2011).

[205] Macak, J., Zlamal, M., Krysa, J. & Schmuki, P.: Self-organized tio2 nanotube layers as highly efficient photocatalysts. *Small* **3**, 300–304 (2007).

[206] Adachi, M., Murata, Y., Harada, M. & Yoshikawa, S.: Formation of titania nanotubes with high photo-catalytic activity. *Chem. Lett.* **29**, 942–943 (2000).

[207] Varghese, O., Gong, D., Paulose, M., Ong, K., Dickey, E. & Grimes, C.: Extreme changes in the electrical resistance of titania nanotubes with hydrogen exposure. *Adv. Mater.* **15**, 624–627 (2003).

[208] Mor, G. K., Carvalho, M. A., Varghese, O. K., Pishko, M. V. & Grimes, C. A.: A room-temperature tio2-nanotube hydrogen sensor able to self-clean photoac-

tively from environmental contamination. *Journal of Materials Research* **19**, 628–634 (2004).

[209] Chen, X. & Mao, S. S.: Titanium dioxide nanomaterials: Synthesis, properties, modifications, and applications. *Chem. Rev.* **107**, 2891–2959 (2007). PMID: 17590053.

[210] Nazeeruddin, M. K., Gao, P. & Grätzel, M.: Organohalide lead perovskites for photovoltaic applications. *Energy Environ. Sci.* **in press**, DOI: 10.1039/C4EE00942H (2014).

[211] Noel, N. K., Stranks, S. D., Abate, A., Wehrenfennig, C., Guarnera, S., Haghighirad, A., Sadhanala, A., Eperon, G. E., Pathak, S. K., Johnston, M. B., petrozza, a., Herz, L. & Snaith, H.: Lead-free organic-inorganic tin halide perovskites for photovoltaic applications. *Energy Environ. Sci.* **in press**, DOI: 10.1039/C4EE01076K (2014).

[212] Hao, F., Stoumpos, C. C., Cao, D. H., Chang, R. P. H. & Kanatzidis, M. G.: Lead-free solid-state organic-inorganic halide perovskite solar cells. *Nat. Photon.* **in press**, DOI: 10.1038/nphoton.2014.82 (2014).

[213] Pellet, N., Gao, P., Gregori, G., Yang, T.-Y., Nazeeruddin, M. K., Maier, J. & Grätzel, M.: Mixed-organic-cation perovskite photovoltaics for enhanced solar-light harvesting. *Angew. Chem. Int. Edit.* **53**, 31513157 (2014).

[214] Brivio, F., Walker, A. B. & Walsh, A.: Structural and electronic properties of hybrid perovskites for high-efficiency thin-film photovoltaics from first-principles. *APL Mat.* **1**, 042111 (2013).

[215] Edri, E., Kirmayer, S., Henning, A., Mukhopadhyay, S., Gartsman, K., Rosenwaks, Y., Hodes, G. & Cahen, D.: Why lead methylammonium tri-iodide perovskite-based solar cells require a mesoporous electron transporting scaffold (but not necessarily a hole conductor). *Nano Lett.* **14**, 1000–1004 (2014).

[216] Deschler, F., Price, M., Pathak, S., Klintberg, L., Jarausch, D. D., Higler, R., Huettner, S., Leijtens, T., Stranks, S. D., Snaith, H. J., Atature, M., Phillips, R. T. & Friend, R. H.: High photoluminescence efficiency and optically-pumped lasing in solution-processed mixed halide perovskite semiconductors. *J. Phys. Chem. Lett.* **5**, 1421–1426 (2014).

[217] Xing, G., Mathews, N., Lim, S. S., Yantara, N., Liu, X., Sabba, D., Grätzel, M., Mhaisalkar, S. & Sum, T. C.: Low-temperature solution-processed wavelength-tunable perovskites for lasing. *Nat. Mater.* **13**, 476–480 (2014).

List of Acronyms

AM	Air-Mass
BBO	Beta-Barium Borate
CB	Conduction Band
CCD	Charge-Coupled Device
DSSC	Dye-Sensitized Solar Cell
EBIC	Electron-Beam-Induced Current
ETM	Electron Transport Material
FA	Formamidinium
FF	Fill-Factor
FIR	Far Infrared
FTO	Fluorine-Doped Tin Oxide
FWHM	Full Width at Half Maximum
HOMO	Highest Occupied Molecular Orbital
HTM	Hole Transport Material
IR	Infrared
LUMO	Lowest Unoccupied Molecular Orbital
MA	Methylammonium
MAI	Methylammonium Iodide
MSSC	Meso-Superstructured Solar Cell
NIR	Near Infrared
NP	Nanoparticle
NREL	National Renewable Energy Laboratory
NT	Nanotube
OPA	Optical-Parametric Amplifier
OPO	Optical-Parametric Oscillator
OPTP	Optical-Pump-THz-Probe
PCE	Power Conversion Efficiency
PL	Photoluminescence
PV	Photovoltaic(s)

sDSSC	solid state Dye-Sensitized Solar Cell
SEM	Scanning Electron Microscopy
TCSPC	Time-Correlated Single Photon Counting
TDS	Time-Domain Spectroscopy
UV	Ultraviolet
VB	Valence Band
XRD	X-Ray Diffraction